Effects of Lubricant Starvation on Performance of Elasto-Hydrodynamically Lubricated Contacts

G. Popovici

Effects of Lubricant Starvation on Performance of Elasto-Hydrodynamically Lubricated Contacts
G. Popovici

Cover Image: G. Popovici

EFFECTS OF LUBRICANT STARVATION ON PERFORMANCE OF ELASTO-HYDRODYNAMICALLY LUBRICATED CONTACTS

PROEFSCHRIFT

ter verkrijging van
de graad van doctor aan de Universiteit Twente,
op gezag van de rector magnificus,
prof. dr. W.H.M. Zijm,
volgens besluit van het College voor Promoties
in het openbaar te verdedigen
op donderdag 3 november 2005 om 15:00 uur

door

Gheorghiţă Popovici

geboren op 16 april 1976
te Iaşi, Roemenië

Dit proefschrift is goedgekeurd door de promotor:
prof. dr. ir. H.W.M. Hoeijmakers
en de assistent promotor:
dr. ir. C.H. Venner

În memoria bunicilor

TABLE OF CONTENTS

SUMMARY

The understanding and the accurate prediction of Elasto-Hydrodynamic Lubrication behaviour is crucial for controlled and reliable operation of machine parts in situations ranging from technical applications like rolling bearings, gears, cam-follower mechanisms, to medical applications such as artificial joints.

Already since the early 1960's the basic aspects of Elasto-Hydrodynamic Lubrication are quite well understood. The film thickness prediction formulas for oil lubricated contacts under steady state conditions derived in these early years are still widely used. However, at present only predicting the nominal film thickness level in the contact is no longer sufficient. As a results of trends in engineering design (see downsizing) the conditions under which the contacts have to operate reliably have become increasingly severe. Higher loads and temperatures lead to significantly reduced film thickness levels. Under these conditions accurate prediction also of the local variations in time of the film thickness due to time varying load or surface roughness moving through the contact is paramount to accurate prediction of performance and service life. In the past decades these topics have been the subject of many experimental and theoretical investigations. In the theoretical research numerical simulations play an important role. A crucial step has been the development of efficient and stable numerical simulation algorithms based on Multigrid techniques.

On the experimental side the optical interferometry technique applied to the model contact of a ball running against a coated glass or sapphire disc has been developed to a very high level. As a result of these developments a detailed validation of the theoretical models is possible. Such validation is one of the points of attention in this thesis.

Most existing models assume oil lubricated contacts under fully flooded conditions, i.e. when ample oil is available in the inlet of the contact. However, in reality most Elasto-Hydrodynamically Lubricated contacts function with grease. Unfortunately the predictive capabilities for grease lubricated contacts are much more limited due to the lack of models for the complex rheological behaviour of the grease and the many complex aspects of lubricant supply that occur in grease lubricated contacts. Most research has therefore been experimental, e.g. using optical inter-

ferometry. However, excluding the early overrollings after relubrication in which the grease is pushed to the side of the track, several aspects of grease lubricated contacts can be modelled quite well with models based on oil lubrication assuming starved lubrication conditions. In recent years this has been done mainly for steady state contacts. In this thesis attention is directed to time varying conditions. Using numerical simulations various aspects of limited lubricant supply on the operation of Elasto-Hydrodynamically Lubricated contacts are studied under steady state and time varying conditions. For example the effect of starvation on the startup of the contact is studied. In addition, based on the results of many simulations simple engineering formulas are presented to predict effect of limited lubricant supply on the deformation of surface roughness inside the contact. In the same way a predictive formula has been derived for the film thickness oscillations induced by variations in the lubricant supply across the contact as well as in time. It is shown that these effects are all governed by a mechanism that can be characterized by a single dimensionless parameter related to the inlet length of the contact.

Input to the starved lubrication model is the shape and thickness of the layer of oil that is supplied to the contact. This is determined by the flow around the contact, and by replenishment that occurs on the track in between overrollings. In many cases it is also influenced by other factors such as cage effects and raceway shape in roller bearings. To validate the predictions of the starved lubrication models requires a method to determine the thickness of this layer in a real contact situation. In this thesis a first step in this direction has been made. It is shown that for sufficiently thin layers the thickness and shape can be measured using optical interferometry. As an application of the thin oil film measurement method the effect of repeated overrolling on the film thickness and the replenishment rate of the contact is investigated experimentally.

Finally, in most studies of Elasto-Hydrodynamically Lubricated contacts the geometry of the undeformed surfaces is approximated by paraboloids. By means of some examples taken from existing rolling element bearing geometries it is shown in this thesis that the existing EHL models can be extended to many other contact shapes.

SAMENVATTING

Het nauwkeurig voorspellen van het gedrag van elasto-hydrodynamisch gesmeerde contacten is cruciaal voor het gecontroleerd en betrouwbaar functioneren van bewegende onderdelen in allerlei situaties, zoals in technische apparaten in lagers, versnellingsbakken, en nok-stoter mechanismes en in medische toepassingen in kunstmatige gewrichten. Daarnaast varieert de schaal van de toepassingen waarin deze contacten voorkomen van microapparaten tot grootschalige aëronautische ontwerpen en zelfs waterkeringen.

Sinds het begin van de jaren zestig van de 20e eeuw is er een goed inzicht in de basisprincipes van elasto-hydrodynamische smering. Empirische formules voor de voorspelling van de smeerfilmdikte in oliegesmeerde contacten in stationaire toestand, die reeds in deze beginjaren zijn opgesteld, worden nog uitgebreid gebruikt. Deze formules voorspellen enkel een nominale smeerfilm dikte, dwz. de waarde in het centrale gedeelte van het contact waar de filmdikte ruwweg constant is, onder stationaire condities, en voor perfect gladde loopvlakken. Tegenwoordig is het niet meer voldoende om alleen deze nominale smeerfilmdikte te kunnen voorspellen. Als gevolg van de huidige ontwikkelingen om apparaten steeds kleiner te maken worden de operationele condities voor de contacten steeds extremer en daarmee worden steeds hogere eisen gesteld aan de betrouwbaarheid. Hogere belastingen en hogere temperaturen leiden tot aanzienlijke reducties van de nominale filmdikte tot slechts enkele tientallen nanometers. Onder deze omstandigheden is het voor een goede voorspelling van de prestatie en levensduur van groot belang dat ook de locale variaties in het contact goed voorspeld kunnen worden, met name in verband met het risico van het optreden van metallisch contact.

In het afgelopen decennium zijn de locale effecten als gevolg van tijdsafhankelijke variatie van de belastingscondities en als gevolg van oppervlakteruwheid uitgebreid theoretisch en experimenteel onderzocht. In het theoretische onderzoek spelen numerieke simulaties een belangrijke rol. Een cruciale stap was de ontwikkeling van snelle, efficiënte, en stabiele numerieke algoritmes gebaseerd op Multigrid-technieken. Op experimenteel gebied is de techniek van optische interferometrie, toegepast op het modelcontact van een kogel op een glazen of saffieren schijf thans

zo geavanceerd dat ook hiermee het gedrag van een contact tot zeer kleine nominale filmdiktes in detail kan worden bestudeerd. Als gevolg van deze ontwikkelingen is het nu mogelijk om de theoretische modellen te valideren. Een dergelijke validatie is een van de aandachtspunten in dit proefschrift.

In de meeste van deze studies wordt uitgegaan van olie als smeermiddel en van een ruim voldoende aanvoer van smeermiddel in de inlaat van het contact. In werkelijkeid werken de meeste elasto-hydrodynamicsche gesmeerde contacten echter niet met olie, maar met vet. De mogelijkheden voor de modellering van vetgesmeerde contacten zijn nog zeer beperkt. Enerzijds is dit het gevolg van het ontbreken van kennis van het gecompliceerde reologisch gedrag van vet. Anderzijds zijn er nog veel onbeantwoorde vragen ten aanzien van de distributie en migratie van het vet in en rondom het contact en is er daardoor nog veel onduidelijkheid over de hoeveelheid en de eigenschappen van het smeermiddel dat beschikbaar is in de inlaat van het contact voor de smeerfilmvorming. Het meeste onderzoek op het gebied van vetsmering is daarom dan ook experimenteel van aard. Met name door middel van de voornoemde techniek van optische interferometrie zijn diverse regimes van het gedrag van vetgesmeerde contacten geïdentificeerd en onderzocht. Zo is gebleken dat in de eerste omwentelingen het vet naar de zijkant van het contactspoor wordt geduwd en daar vervolgens functioneert als een afdichting tegen vuil van buitenaf en als reservoir waaruit basisolie op het spoor kan vloeien welke dan zorgt voor de smering van het contact. Deze situatie kan gemodelleerd worden als een schraal gesmeerd contact met de basisolie van het vet als smeermiddel.

Tot op heden beperken de studies op het gebied van schraalgesmeerde contacten zich meestal tot de stationaire situatie. In dit proefschrift wordt aandacht besteed aan de effecten van tijdsafhankelijke omstandigheden. Met behulp van numerieke simulaties zijn de effecten van schrale smering op het functioneren van elasto-hydrodynamisch gesmeerde contacten bestudeerd. Zo is bijvoorbeeld het effect van schrale smering op de filmopbouw gedurende het opstarten van het contact onderzocht. Tevens zijn de effecten van schrale smering op de vervorming van oppervlakteruwheid in het contact, en van locale en tijdsafhankelijke variaties van de smeermiddel toevoer in de inlaat van het contact, op de grootte van de locale filmdikte oscillaties in het contact bestudeerd. Met behulp van numerieke simulaties voor een groot aantal verschillende condities is aangetoond dat de deformatie van ruwheid en de locale filmdikte oscillaties geinduceerd door variaties in de smeermiddeltoevoer, bepaald worden door een enkele dimensieloze parameter die gekarakteriseerd kan worden als een dimensieloze inlaatlengte van het contact. Empirische formules zijn afgeleid voor praktisch gebruik bij oppervlakteoptimalisatie in ontwerp.

Een beperking bij het gebruik van de resultaten van schrale smeringsmodellen in de praktijk is dat in het model de dikte en vorm van de olielaag die aan het contact wordt toegevoerd gegeven wordt verondersteld. Deze is echter in het algemeen niet

bekend en wordt bepaald door de locatie van het vet, de stroming rond het contact, en door het terugvloeien van smeermiddel op het contactspoor tussen verschillende passages. Daarnaast spelen in een kogellager ook andere factoren een belangrijke rol, zoals de kooi en de geometrie. Om de voorspellingen van schraalgesmeerde contactmodellen te kunnen valideren is een methode nodig om in een modelcontact de dikte van deze laag in een echte contactsituatie te bepalen, en de relatie tussen de dikte van de laag en de filmdikte in het contact. In principe is optische interferometrie hiervoor uitermate geschikt. In dit proefschrift wordt een eerste stap gezet in de richting van zulke olielaag metingen. Er wordt aangetoond dat bij voldoende dunne lagen de dikte ervan gemeten kan worden.

Tot slot wordt in de meeste studies op het gebied van Elasto-hydrodynamisch gesmeerde contacten de geometrie van de onvervormde oppervlakken benaderd door paraboloïdes. Door middel van enkele voorbeelden van bestaande wentellagergeometrieën wordt in dit proefschrift aangetoond dat de EHL modellen en numerieke oplosalgoritmes gemakkelijk kunnen worden uitgebreid naar andere geometrieën.

ACKNOWLEDGMENTS

NOMENCLATURE

a Hertzian contact ellipse axis parallel to flow direction, [m]

A_c dimensionless amplitude of the central film thickness, [-]

A_{cc} dimensionless acceleration, [-], $A_{cc} = \frac{a_{cc} \cdot a}{u_m^2}$

A_{d+c} combined dimensionless amplitude of the central film thickness, [m]

A_d dimensionless deformed amplitude, [-]

A_i dimensionless initial amplitude, [-]

b Hertzian contact ellipse axis perpendicular to flow direction, [m]

c Hertzian mutual approach, [m]

C constant, [-], $C = 2^{-3/2} 3^{-5/4} \pi^2 \kappa^{-1/2}$, see Damiens [18]

C_D dimensionless parameter, [-], $C_D = \frac{r\kappa}{W_Y}\sqrt{\frac{L}{M}}$, see Damiens [18]

C_O dimensionless parameter, [-], $C_O = (I\!R)_{max} \frac{\mathcal{W}_X^{3/2}}{S_{ff} \cdot I\!R^2}$

d elastic deformation, [m]

D spatial domain, [-]

E' reduced elastic modulus, [Pa], $\frac{2}{E'} = \frac{1-\nu_1^2}{E_1} + \frac{1-\nu_2^2}{E_2}$

f_a variation factor, [-]

F external load, [N]

F_N nominal load, [N]

h gap height, [m]

h_c central film thickness, [m]

h_{cff} central film thickness in fully flooded conditions, [m]

h_{min} minimum film thickness, [m]

h_{oil} thickness of the oil layer supplied at the inlet, [m]

h_l thickness of the oil layer, [m], $h_l = \theta \, h$

h_s film thickness in starved conditions, [m]

$h_{X,Y}$ dimensionless mesh size in X, Y direction, [-]

h_T dimensionless time step, [-]

H dimensionless gap height, [-]

H_l dimensionless thickness layer, [-], $H_l = \theta \cdot H$

$\overline{H}_{oil}$ mean dimensionless thickness of the lubricant layer, [-]

H_{cff} dimensionless central film thickness in fully flooded conditions, [-]

H_{cM} Moes dimensionless film thickness, $H_{cM} = \frac{h}{R_x}\left(\frac{\eta_0 2 u_m}{E' R_x}\right)^{-1/2}$, [-]

H_s dimensionless central film thickness in starved conditions, [-]

H_{oil} dimensionless thickness of the oil layer supplied at the inlet, [-]

I_O moment of inertia of lever around O, [$kg\ m^2$], $I_O = m_r(L_A + L_B)^2/12$

K elastic kernel, [-]

$\overline{K}$ dimensionless stiffness, [-], $\overline{K} = k\ c/F$

L lubricant dimensionless (Moes) parameter, [-]

$L_{A,B}$ length of the lever OA, OB in the loading system configuration

m_1 mass of the ball, [kg]

m_2 mass of the loading mass, [kg]

m_r mass of the loading lever in the loading system, [kg]

$\overline{m}$ equivalent mass of the system, [kg], $\overline{m} = m_1 + m_2 + I_O/L_A^2$

M load dimensionless (Moes) parameter, [-]

p pressure, [Pa]

p_r reference pressure, [Pa], $p_r = 1.96 \times 10^8$

p_H Hertzian maximum dry contact pressure, [Pa]

P dimensionless pressure, [-]

r dimensionless relative lubricant layer thickness, [-], $r = H_{oil}/H_{cff}$

$\overline{r}$ mean dimensionless relative lubricant layer thickness, [-], $\overline{r} = \overline{H}_{oil}/H_{cff}$

r_w surface waviness, [m]

R reduced radius of curvature, [m], $1/R = 1/R_x + 1/R_y$

$R_{x,y}$ reduced radius of curvature in x, y direction, [m]

$R_{1x,2x}$ radius of curvature in x direction of body $1, 2$, [m]

$R_{1y,2y}$ radius of curvature in y direction of body $1, 2$, [m]

$\mathbb{R}$ degree of starvation, [-], $\mathbb{R} = H_{cs}/H_{cff}$

$\mathbb{R}_{max}$ maximum amplitude reduction factor for lubricant layer oscillations, [-]

$\mathcal{R}$ dimensionless surface waviness, [-]

S inlet length of the starved circular contact, [m]

S_{ff} inlet length of the fully flooded circular contact, [m]

$\overline{S}_{ff}$ inlet length in fully flooded conditions, [-], $\overline{S}_{ff} = C\sqrt{\frac{\mathbb{E}}{\kappa(1+\mathbb{D})}}\sqrt{\frac{L}{M}}$

t time, [s]

T dimensionless time, [-], $T = t\ u_m/a$

T_0 dimensionless initial time, [-]

$u_{1,2}$ velocity of surface $1, 2$, [m/s]

u_m mean velocity, [m/s], $u_m = (u_1 + u_2)/2$

u_s sum velocity, [m/s], $u_s = u_1 + u_2$

$\overline{u}(t)$ momentary entrainment velocity, [m/s]

x coordinate in direction of flow, [m]

X dimensionless coordinate in direction of flow, [-]

x' coordinate, [m]

X' dimensionless coordinate, [-]

X_0 dimensionless position of waviness,[-], $X_0 = X_a + T$,

y coordinate perpendicular to direction of flow, [m]

y' coordinate, [m]

Y dimensionless coordinate perpendicular to direction of flow, [-]

Y' dimensionless coordinate, [-]

z coordinate in vertical direction, [m]

z pressure-viscosity index in Roelands equation, [-], $z = \alpha p_r / (ln(\eta_0) + 9.67)$

$z_{1,2}$ undeformed geometry of surface $1, 2$, [m]

α pressure-viscosity index, $[Pa^{-1}]$

$\overline{\alpha}$ dimensionless parameter, [-], $\overline{\alpha} = \alpha p_H$

γ dimensionless parameter, [-]

δ mutual approach, [m]

δ_∞ mutual approach at equilibrium, [m]

Δ dimensionless mutual approach, [-]

Δ_∞ dimensionless mutual approach at equilibrium, [-]

κ ellipticity ratio, [-], $\kappa = a/b$ (wide elliptic) $|| \, \kappa = b/a$ (narrow elliptic)

η viscosity, $[Pa\,s]$

η_0 viscosity at ambient pressure, $[Pa\,s]$

$\overline{\eta}$ dimensionless viscosity, [-], $\overline{\eta} = \eta/\eta_0$

ρ density, $[kg/m^3]$

ρ_0 density at ambient pressure, $[kg/m^3]$

$\overline{\rho}$ dimensionless density, [-], $\overline{\rho} = \rho/\rho_0$

$\overline{\lambda}$ dimensionless parameter, [-], $\overline{\lambda} = 6u_s \eta_0 a / c^2 p_H$

$\overline{\nabla}$ dimensionless parameter, [-], $\overline{\nabla} = \mathcal{W}_{X,Y} / (\sqrt{L/M} \cdot I\!R^{3/2})$

Ω dimensionless natural frequency, [-], $\Omega = \sqrt{FR_x / \overline{m} u_m^2}$

$I\!K$ first kind elliptic integral, [-], $I\!K(m) = \int_0^{\frac{\pi}{2}} 1/\sqrt{1 - m^2 sin^2(\psi)} d\psi$

$I\!E$ second king elliptic integral, [-], $I\!E(m) = \int_0^{\frac{\pi}{2}} \sqrt{1 - m^2 sin^2(\psi)} d\psi$

$I\!D$ gap curvature ratio, [-], $I\!D = R_x / R_y$

$\mathcal{W}_{X,Y}$ waviness wavelength in X, Y direction, [-]

INTRODUCTION

Control of friction, lubrication and wear is a subject of interest in our modern society as it has been for thousands of years. Dragging animal carcasses in different weather conditions were, probably, the first tribological experiments. The early civilizations used animal fat, olive oil or tree trunks underneath sleds to reduce friction. As the need of motion developed into transportation needs, even more control over friction was needed, brakes were required, and first attempts of using bearings and gears were materialized. With introduction of steam engines and further industrial developments, the role of friction, lubrication and wear became increasingly important. Our modern society would collapse without strong knowledge of tribology. Just imagine that there are no lubricants, engines, bearings or gear boxes! In addition to automotive and industrial applications, tribology knowledge is used for many other purposes, including bio-medical applications (e.g. artificial joints), personal hygiene, conditioners, contraceptives, etc.

The science of lubrication, friction and wear is highly interdisciplinary and involves physics, fluid dynamics, chemistry, mechanics, mathematics, etc. Input from these fields is continuously needed when new questions and challenges are addressed. In the early years of the last century scientists with a wide view of the principle of physics, chemistry and mathematics introduced the first tribological models and concepts that are still used today. Nowadays, owing to these bright minds, engineers have strong knowledge of tribology, helping them to develop efficient, safe and reliable products.

Part of the research in tribology concerns the lubrication of the heavily loaded contacts referred to as Elasto-Hydrodynamic Lubrication or in short EHL. This is also the topic of the present thesis. Figure 1.1 shows a few typical examples of EHL contacts encountered in everyday life. The results presented in this thesis are focused on bearing applications, but they can be easily adapted to gears and automotive industry, bio-mechanical applications, etc.
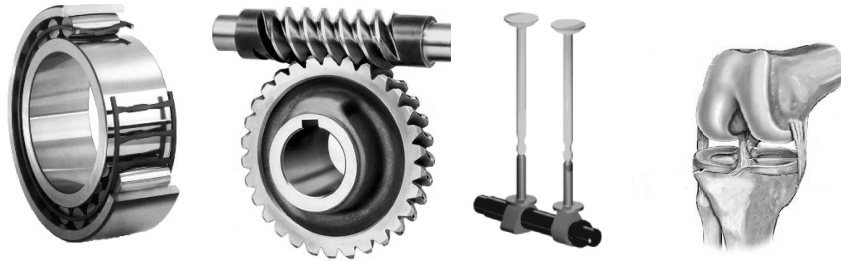
FIGURE 1.1: *Examples of EHL contacts, from left to right: roller bearing, worm gear, cam-follower mechanism, knee joint.*

1.1 Rolling bearings

Rolling bearings are used in many applications, from heavy-duty use in vehicle axles and machine shafts, to precision clock parts. The simplest example of a linear bearing is an arrangement of pencils laid on your desk under a heavy book. With this very "technology", The Seven Wonders of the Ancient World were possible. A wreck of a "thrust bearing" discovered on a Roman ship is shown in Figure 1.2 (left). The bearing was, probably, part of a rotating platform used to load and unload the ship, allowing the top platform to turn easily. Leonardo da Vinci also tried to find ingenious techniques of reducing friction. In Figure 1.2 (right) a working bearing model, build after his sketches, is shown. Major contributions to the bearing as we know it today were brought by Galilei, John Harrison, Philip Vaughan of Carmarthen and Friedrich Fischer.

The modern design of the self-aligning ball bearing is attributed to Sven Wingquist of the ball-bearing manufacturer SKF in 1907. Standards for roller bearing design were initiated by the work of Lundberg and Palmgren [50], [51]. They found that the life of roller bearings is affected by fatigue cracks initiated below the surface of the rolling contact due to orthogonal shear stress and defects in the material. In the following decades the development of the EHL theories and the new standards for life expectation and dynamic load rating have improved the quality of rolling bearings to a high degree. Nowadays it is known that a bearing can have an infinite lifetime if it is clean, lubricated, run within the rated load, and if the materials are sufficiently free of microscopic defects. Ideal operating conditions are relatively easy to achieve, but difficult to maintain. Most of the bearings have seals or shields that keep the lubricant inside the bearing and the contaminants out. However, the seals are not always a guarantee of ideal lubrication conditions. In these cases the effects of lubricant loss or contamination on the performance of the bearing need to be precisely determined.
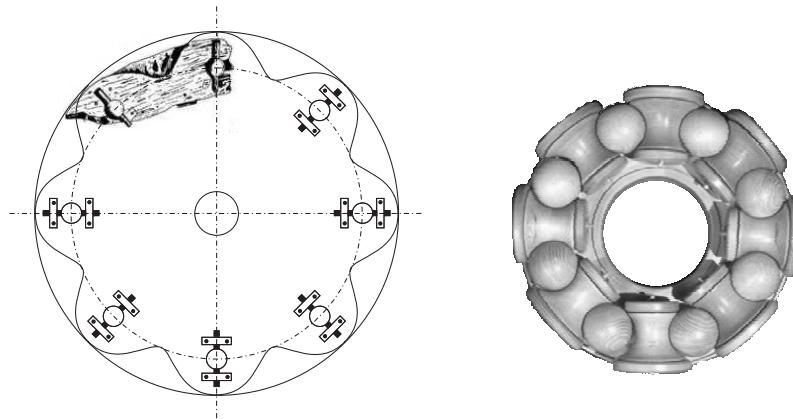
FIGURE 1.2: *Fragment of a rotating platform recovered from a Roman ship (left); Wooden model of Leonardo da Vinci's pressure resistant ball bearing (right), [Courtesy Museum of the History and Science - Florence]*

1.2 EHL background

The discovery of hydrodynamic lubrication laid the foundation of lubrication theory. Revolutionary evidence of hydrodynamic lubrication was published by Beauchamp Tower (1883), [68]. Contradicting Coulomb's law of friction Tower confirmed that when the lubrication is adequate the friction coefficient varies with velocity and is independent of the load. It was concluded that in a well-lubricated bearing the brass floats on a film of oil. Moreover, he found that pressures within certain parts of the oil film exceeded the mean pressure due to the applied load and published in 1885 [69] the measured pressure distribution in railway journal bearings.

Two years later Osborne Reynolds [63] presented the theory of fluid film lubrication in terms of a differential equation, describing the pressure build up in the oil film, see Figure 1.3. As a practical application, Reynolds deduced that the radius of the brass must be slightly greater than the radius of the journal. This deduction was used by engineers many years in the design of journal bearings.

However, there were still many applications that could not be explained by the hydrodynamic theory only. Miraculously, heavily loaded gears and roller bearings were lasting much longer than expected in spite of the very small film thickness predicted by hydrodynamic theory, see Martin [52]. The explanation of Grubin [28] was that under heavy loads the assumption of rigid solids, incompressible and isoviscous lubricant were wrong. Grubin's model predicted film thicknesses which were orders of magnitude larger than Martin's [52]. Moreover, Grubin qualitatively described the distribution of lubricant in the contact area and predicted a pressure spike close to the outlet of the contact. These findings were confirmed by Petrusevich in 1951, [60]. Based on laborious numerical calculations a convenient dimensionless formula for
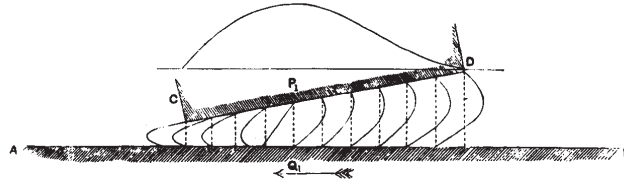
FIGURE 1.3: *Professor Osborne Reynolds' general view on the action of lubrication of inclined plane surfaces with tangential movement*

the minimum film thickness could be written in terms of load, speed, and material parameters by Dowson and Higginson [14].

In the following years progress in theory was hampered by the instability of the numerical algorithms and the excessive computational time. With the introduction of multilevel methods in lubrication by Lubrecht [48] and with the later developments by Venner [70], the efficiency and the stability of the numerical methods improved dramatically. Based on numerical calculations, function fit formulas for the prediction of film thickness were proposed by Moes, Nijenbanning and Venner [54], [57] using a minimum number of similarity parameters and validation for a wide range of operating conditions.

Cameron and coworkers, [8], [22], were the pioneers of optical interferometry in lubrication. Capacitive and resistive measurement methods were also used for measurement of the oil film thickness in bearings and piston rings. However, the optical interferometry was found more suitable for model EHL contacts. Using such an experimental setup, Wedeven [78], [79], investigated experimentally the rolling point contact under poor lubrication conditions and presented schematically the distribution of lubricant within the cavitated region of the contact. Furthermore, Chiu's [12] analysis on lubricant replenishment revealed that the degree of lubricant starvation depends strongly on the thickness of the oil layer around the rolling track. Experimental techniques could also be used for conditions for which the EHL modelling failed because of the complexity of the phenomena. Cann [6], [7] used optical interferometry, to study the grease lubricated contacts and revealed many different aspects of their behaviour.

Gradually, more complex phenomena could be approached, also numerically. Chevalier and co-workers [9], [10] studied the mechanism of starved lubrication and proposed a theoretical model which gave good qualitative agreement with experiments. The growing need for accurate prediction of the vibration levels of roller bearings motivated Wijnant et al. [82], [83], [84] and Wensing [80] to combine the numerical solution of transient EHL with a Finite Element Model model of a roller bearing. The effect of surface waviness on the EHL film was modelled by Venner et al. [73], [74]

and to predict probability of contact [53]. The effect of lubricant starvation was also included, see Venner [76], but it was restricted to constant thickness lubricant layers. Damiens [18] updated the steady state models with variable lubricant layers across the rolling direction. In the same study, [18], Damiens investigated the influence of different bearing cage designs on the lubricant supply.

1.3 Objectives

The studies mentioned above have given essential insight in the effects of lubrication on performance of isolated EHL contacts. However, information on contacts, as they appear in real applications, is still needed.

Firstly, in many cases the contact area is an ellipse oriented according to the needs of functionality of the respective machine part. Separate studies of the influence of ellipticity on EHL performance were presented by Chittenden [11], Nijenbanning [57], Wijnant [83], Damiens [18], Sharif [67]. In this study, an overview of the ellipticity effect is presented and supported by experimental results. Furthermore, the effect on the EHL performance of (specific) tailor-made surface geometries in contact is of high interest.

Secondly, in starved lubrication conditions the central film thickness can drop dramatically, increasing the probability of metal to metal contact. Obviously, it is desired that this phenomena is either avoided or predicted accurately and controlled. The effect of a steady state uniform layer on the central film thickness in a circular and elliptic EHL contact has been quantified already by Chevalier et al. [9] and Damiens et al. [18]. Now the effect of the inlet layer shape on film thickness needs to be studied in more detail for uniform and variable oil layers over the width of the contact.

Thirdly, the studies regarding the effect of starvation on the film thickness carried out so far were restricted to steady state situations, whereas in reality the thickness of the layer of oil supplied to the contact may vary in time. The study of starved elliptic contacts with time-dependent input conditions requires extension of the starvation model and of the numerical solution algorithm. The numerical solution algorithm also needs to be improved from a point of view of stability, robustness, and easiness for use in actual applications.

In addition to the theoretical study, experimental research is needed to validate the findings. At present the best way to obtain such validation is by means of optical interferometry.

Finally, the results of the studies regarding the contact performance should be implemented in existing analysis tools and simple design-rules need to be derived for practical use.

THEORY

In this chapter the equations describing Elasto-Hydrodynamic Lubrication are presented. The boundary conditions and the main assumptions are also discussed. State of the art results are given in order to introduce the reader to the latest developments in the EHL field.

2.1 The Elasto-Hydrodynamic Lubrication model

In the late 19th century it was established that the presence of viscous fluids between surfaces in relative motion generates hydrodynamic pressure and a separating fluid film [68], [69], [63]. These findings, combined with the elastic deformation of the surfaces and the piezo-viscous effects are considered as the foundation of EHL theory. According to this theory, the generation of hydrodynamic pressure in the fluid film is described in terms of a differential equation. An integral equation prescribes the elastic deformation and an exponential viscosity pressure dependence is assumed. A quantitative description of the contact behavior requires the solution of these equations simultaneously. The solution can be used to determine various performance parameters of the EHL contact. For example, the film thickness solution will indicate if a sufficiently thick fluid film is generated for surface separation, while the pressure and its variation in time provide essential input for stress and fatigue calculations. The generally used EHL model consists of:

- Reynolds' equation for the flow in the gap;

- gap height equation including the elastic deformation of the surfaces in contact;

- constitutive equation for the lubricant such as the viscosity-pressure and the density-pressure relationship;

- force balance equation.

2.1.1 Reynolds equation

To describe the flow between surfaces in relative motion, the so called *Reynolds* equation can be used. This equation follows from the Navier-Stokes equation when a very small gap is assumed between the contacting surfaces. This assumption is justified as long as the gap height is much smaller than its width. However, if the film around the surface roughness (micro-geometry) is studied, the local value of the ratio of the film thickness to the roughness wavelength may no longer be small. In such cases the Reynolds equation may not be accurate and the Stokes equation should be used to model the flow, see Odyck [58].

Another assumption made in the derivation of the Reynolds equation is that laminar flow takes place. This implies that inertia and surface forces are small compared to the viscous forces, which is indeed the case for most lubricated contacts.

If the velocities of both surfaces are in the x-direction only and fully flooded conditions apply, the Reynolds equation relating the pressure $p(x, y, t)$ to gap height $h(x, y, t)$ reads:

$$\frac{\partial}{\partial x}\left(\frac{\rho h^3}{12\eta}\frac{\partial p}{\partial x}\right) + \frac{\partial}{\partial y}\left(\frac{\rho h^3}{12\eta}\frac{\partial p}{\partial y}\right) = u_m\frac{\partial(\rho h)}{\partial x} + \rho h\frac{\partial u_m}{\partial x} + \frac{\partial(\rho h)}{\partial t} \qquad (2.1)$$

The dynamic viscosity and the density of the lubricant are denoted by η and ρ, respectively. The mean entrainment velocity of the two surfaces in the x-direction is denoted by u_m. The three terms on the right hand side represent the *wedge* effect, the *stretch* effect and the *squeeze* effect, respectively. The flow induced by the wedge term is known as *Couette flow*, whereas the left hand side of the equation represents the *Poiseuille flow* terms. For most EHL contacts the tangential deformation is very small compared to the normal deformation and the stretch term is neglected.

Because the average atmospheric pressure (10^{-4}[GPa]) is much smaller than the contact pressures (10^0[GPa]), it is justified to assume on the boundary enclosing the spatial domain the pressure zero.

$$p(x, y, t) = 0; \quad \forall (x, y, t) \in \partial D \qquad (2.2)$$

where ∂D denotes the boundary of the spatial domain.

At atmospheric pressure most of the lubricants contain dissolved gas. According to the thermodynamic laws the pressure in liquid state cannot drop below its vapor pressure. When the pressure inside the liquid reaches the vapor pressure the dissolved gas spreads into gas bubbles. The pressure at which cavitation takes place is generally smaller than the pressures encountered in EHL contacts and not much below the atmospheric pressure. Therefore, the solution for the pressure from Equation (2.1) is subjected to the cavitation condition as follows:

$$p(x, y, t) \geq 0; \quad \forall (x, y, t) \in D \tag{2.3}$$

2.1.2 Gap height equation

The separation between contacting surfaces, taking into account the elastic deformation, is given by:

$$h(x, y, t) = -\delta(t) + z(x, y) - r_w(x, y, t) + d(x, y, t) \tag{2.4}$$

with

- $\delta(t)$ is the displacement of the points unaffected by elastic deformation, often refereed to as *mutual approach* [it follows from the force balance equation (2.8)];

- $z(x, y)$ the given initial (undeformed) geometry of the surfaces;

- $r_w(x, y, t)$ surface roughness;

- $d(x, y, t)$ the deformation of the two contacting surfaces, given by (2.11) below.

For two surfaces of revolution (1 and 2) with given curvatures in x and y direction

$$\frac{1}{R_x} = \frac{1}{R_{x1}} + \frac{1}{R_{x2}} \tag{2.5}$$

and

$$\frac{1}{R_y} = \frac{1}{R_{y1}} + \frac{1}{R_{y2}} \tag{2.6}$$

the initial gap height $z(x, y)$ can be obtained expanding the equation of each surface in a Taylor series about the origin O (i.e. Maclaurin series) neglecting the high-order terms and using the fact that the surfaces are tangent at the common plane xOy as follows:

$$z(x, y) = \frac{1}{2R_x} x^2 + \frac{1}{2R_y} y^2 \tag{2.7}$$

This is the most common expression for the undeformed gap height in EHL contact models.

2.1.3   Force balance

The *mutual approach* δ from (2.4) is generally unknown. In order to obtain a well-posed problem with an unique solution for p and h equilibrium of forces acting on the system is required. In most of the theoretical studies, it is assumed that the inertia forces are small enough to be neglected. In reality, the importance of these effects depend on the dynamics of the load, the stiffness of the loading system and the speed conditions. Neglecting inertia and stiffness effects, the force balance equation reads

$$\iint_D p(x,y,t)dxdy = F(t) \tag{2.8}$$

with $F(t)$ the external load on the contact.

2.1.4   Constitutive lubricant equations

The viscosity and density of the lubricant are generally pressure and temperature dependent. Many rheological models are available, *Ree-Eyring* [44] and *Limiting shear stress* [42] being the most popular. A detailed comparison between the different rheological models can be found in Jacod [41]. In the present study pure rolling conditions are assumed (no slip), which implies that non-Newtonian effects are negligible.

Classical relationships describing the viscosity dependence on pressure are those introduced by Barus [3] and Roelands [65]. For most lubricants, the Barus relation overestimates the viscosity and the Roelands relation predicts more accurately the viscosity up to pressures of $1[GPa]$. Recently Yasutomi, Bair and Winer [2], [85] made use of the so-called *free volume* model, which can describe the pressure-viscosity relationship accurately for a wider range of pressures and is very suitable for the prediction of friction. For friction calculations under conditions of sliding the use of an accurate rheological model and viscosity-pressure relation is crucial. However, in this thesis emphasis is on film thickness calculations and prediction under pure rolling conditions. In this case the Roelands equation (2.9) is sufficiently accurate.

$$\eta(p) = \eta_0 \, exp \left\{ [ln(\eta_0) + 9.67] \left[-1 + \left(1 + \frac{p}{p_r} \right)^z \right] \right\} \tag{2.9}$$

with $p_r = 1.96 10^8$ a reference pressure, z pressure-viscosity index ranging from 0.1 to 1.5 for different lubricants and η_0 the dynamic viscosity at ambient pressure.

According to the exponential viscosity-pressure relationship (2.9), the viscosity increases many orders of magnitude, causing the lubricant to behave as a "solid" in the high pressure regions. This implies that the lubricant flow *inside the contact* is constrained by the high viscosity occurring in the contact region, for details see Jacod [40].
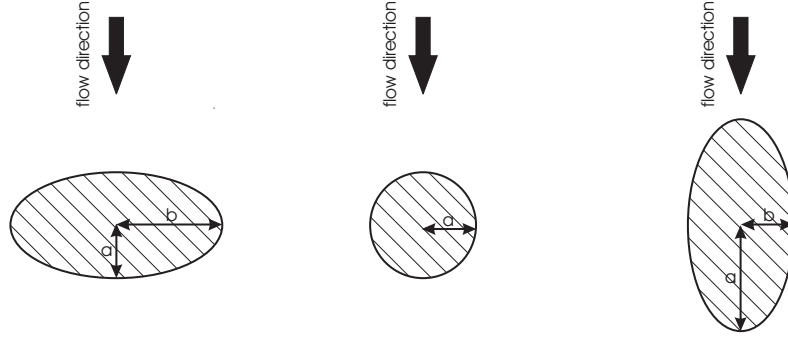
FIGURE 2.1: *Wide elliptic (left), circular (center) and narrow elliptic (right) elliptic EHL contacts*

The density of mineral oils increases with pressure. A widely used (empirical) density-pressure relationship is the Dowson-Higginson equation, [15].

$$\rho(p) = \rho_0 \frac{0.59 \cdot 10^9 + 1.34 \cdot p}{0.59 \cdot 10^9 + p} \tag{2.10}$$

2.2 Elastic deformations of surfaces in contact

In the framework of linear elasticity theory, the pressure field $p(x, y)$ and the deformation $d(x, y)$ are related by the following surface integral representation :

$$d(x, y, t) = \frac{2}{\pi E'} \iint_D K(x - x', y - y')p(x', y', t)dxdy \tag{2.11}$$

with E' reduced elasticity modulus, K the $Green$ function of the elastic isotropic halfspace, calculated in the 19th century by $Boussinesq$.

$$K(x - x', y - y') = \frac{1}{\sqrt{(x - x')^2 + (y - y')^2}}dxdy \tag{2.12}$$

An analytical solution for the concentrated contact ($h(x, y, t) = 0$) between elastic surfaces with arbitrary curvatures was presented by Hertz [33] in 1896. Hertz assumed smooth surfaces, which are perfectly elastic, isotropic, homogeneous and frictionless. This so-called *dry contact model* is still used today in contact mechanics as a reference and for scaling purpose. The contact area is generally *elliptic*, having different orientations relative to the direction of rolling (flow), see Figure 2.1. In the present thesis the ellipse axis parallel to the rolling direction is denoted as a and the axis perpendicular to the rolling direction is denoted by b. A contact ellipse with the major axis perpendicular to the rolling direction is referred to as *wide* elliptic contact and the type of contact with the major axis parallel to the rolling direction as *narrow*
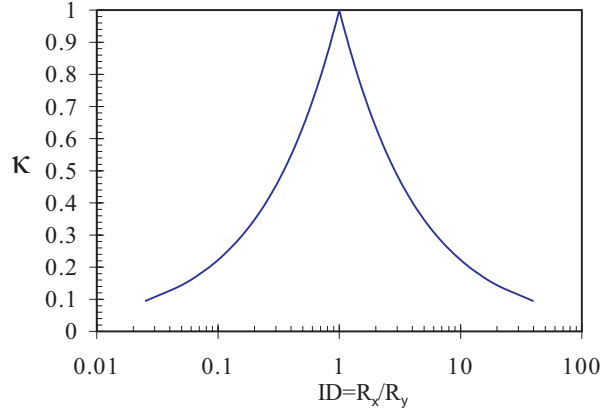
FIGURE 2.2: *Evolution of the ellipticity factor κ as function of $\mathbb{D} = R_x/R_y$*

elliptic contact. The difference between wide and narrow elliptic contacts turns out to be important when the lubricant flow is taken into account. The ellipticity factor κ is defined as the ratio between the minor and the major ellipse axis. This implies that κ never exceeds unity ($0 < \kappa \leq 1$). According to the Hertz solution the values of a, b and κ are given by:

Wide elliptic EHL contacts	Narrow elliptic EHL contacts	
$a = \left(\frac{3FR}{E'}\right)\sqrt[3]{\frac{2\kappa\mathbb{E}}{\pi}}$	$a = \frac{b}{\kappa}$	(2.13)
$b = \frac{a}{\kappa}$	$b = \left(\frac{3FR}{E'}\right)\sqrt[3]{\frac{2\kappa\mathbb{E}}{\pi}}$	

Approximate expression for *first* and *second* kind complete elliptic integrals ($\mathbb{K}$, $\mathbb{E}$) and κ are given in Appendix A. For circular contacts $\mathbb{D} = 1, \kappa = 1, m = 0, \mathbb{K} = \pi/2, \mathbb{E} = \pi/2$. Please note that the ellipticity factor κ is related to R_x/R_y ratio, which can be either smaller or larger than unity, see Figure 2.2. As a result different relationships are used for wide and narrow elliptic EHL contacts:

Wide elliptic EHL contacts	Narrow elliptic EHL contacts	
$\mathbb{D} = \kappa^2 \frac{\mathbb{K}-\mathbb{E}}{\mathbb{E}-\kappa^2\mathbb{K}}$	$\frac{1}{\mathbb{D}} = \kappa^2 \frac{\mathbb{K}-\mathbb{E}}{\mathbb{E}-\kappa^2\mathbb{K}}$	(2.14)

The pressure distribution in a dry contact is semi-ellipsoid, with its maximum given by:

$$p_H = \frac{3F}{2\pi ab} \qquad (2.15)$$

The mutual approach of two remote points in the solid where the elastic deformation can be neglected can be written as:

Wide elliptic EHL contacts	Narrow elliptic EHL contacts	
$c = \frac{a^2}{2R}\frac{\mathbb{K}}{\mathbb{E}}$	$c = \frac{b^2}{2R}\frac{\mathbb{K}}{\mathbb{E}}$	(2.16)

2.3   Starved Lubrication

The so called starved lubrication is one of the key aspects for the understanding of the phenomena occurring in grease lubricated rolling bearings. The Reynolds equation (2.1) is valid as long as the inlet gap of an EHL contact is filled with lubricant. However, in practice this is not always the case. The lack of lubricant in the neighborhood of the contact region is often referred to as *starved lubrication* and has major consequences for the performance of the EHL contact. The starved lubrication makes the boundary with the pressurized region a free boundary, see Figure 2.3. The determination of this boundary (meniscus) is part of finding the solution. If the meniscus is far enough from the pressurized region, fully flooded lubrication takes place. On the other hand if the meniscus inhibits the generation of pressure (and consequently the film thickness build up) the EHL contact is considered to operate in starved lubrication conditions.

A convenient way to account for starved lubrication was described in detail by Jakobsson and Flodeberg, [43], Elrod [19], Chevalier [9], Wijnant [83]. The main idea is to define a fractional film content (θ) defined as the ratio between the thickness of the lubricant layer (h_{oil}) and the gap height (h) as follows:

$$\theta(x, y) = \frac{h_{oil}(x, y)}{h(x, y)}. \tag{2.17}$$

Defining the boundary of the pressurized regions ($\theta = 1$) and the cavitated regions $0 \leq \theta < 1$ the variables: p, h and θ, are solved from the *modified Reynolds equation* and the equations (2.4), (2.8):

$$\frac{\partial}{\partial x}\left(\frac{\rho h^3}{12\eta}\frac{\partial p}{\partial x}\right) + \frac{\partial}{\partial y}\left(\frac{\rho h^3}{12\eta}\frac{\partial p}{\partial y}\right) = u_m\frac{\partial(\theta\rho h)}{\partial x} + \frac{\partial(\theta\rho h)}{\partial t} \tag{2.18}$$

Please remember that the *stretch* term is neglected because the tangential deformation are much smaller then the normal deformation. The equation (2.18) serves as an equation for the pressure in pressurized regions ($\theta = 1$), and as a Couette flow mass conservation equation in the cavitated regions ($\theta < 1$). For a detailed derivation of the kinematic and dynamic conditions that should hold at the interface the reader is referred to Jakobsson et al. [43], Bayada et al. [4]. This formulation was used with success by Chevalier [9], Wijnant [83] and Damiens [18] and is also adopted in the present study.

(a)

(b)
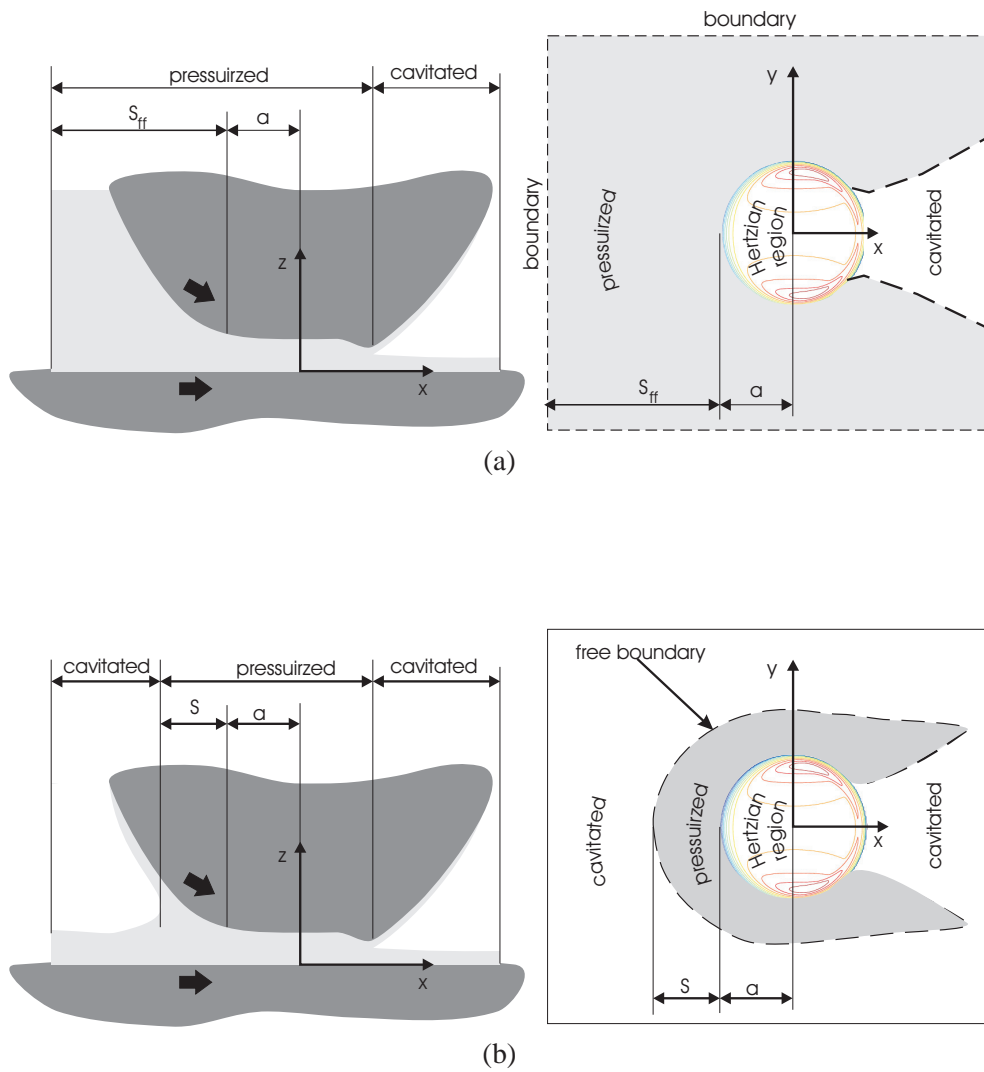
FIGURE 2.3: *Fully flooded EHL (a), starved EHL (b)*

2.4 Dimensionless equations and parameters

The equations presented above $(2.1)-(2.9)$ involve many variables, making parameter studies difficult. The parameters involved in the EHL equations (2.1) to (2.9) are not all independent and their number can be reduced, see [54]. The Hertzian dry contact parameters (2.13)- (2.16), the viscosity and the density at ambient pressure are often used to obtain dimensionless equations. In the present study the dimensionless variables are defined as:

$$
\begin{array}{ccc}
X = x/a & Y = y/b & Z = z/c \\
P = p/p_H & H = h/c & \Delta = \delta/c \\
\bar{\rho} = \rho/\rho_0 & T = t\, u_m/a & \bar{\eta} = \eta/\eta_0
\end{array}
\tag{2.19}
$$

Using these dimensionless variables the *dimensionless Reynolds equation* for *wide elliptic* contacts is obtained from (2.18) as follows:

$$
\frac{\partial}{\partial X}\left(\frac{\bar{\rho}H^3}{\bar{\eta}\bar{\lambda}}\frac{\partial P}{\partial X}\right) + \kappa^2\frac{\partial}{\partial Y}\left(\frac{\bar{\rho}H^3}{\bar{\eta}\bar{\lambda}}\frac{\partial P}{\partial Y}\right) = \Lambda(T)\frac{\partial(\theta\bar{\rho}H)}{\partial X} + \frac{\partial(\theta\bar{\rho}H)}{\partial T}
\tag{2.20}
$$

and for *narrow elliptic* contacts

$$
\frac{\partial}{\partial X}\left(\frac{\bar{\rho}H^3}{\bar{\eta}\bar{\lambda}}\frac{\partial P}{\partial X}\right) + \frac{1}{\kappa^2}\frac{\partial}{\partial Y}\left(\frac{\bar{\rho}H^3}{\bar{\eta}\bar{\lambda}}\frac{\partial P}{\partial Y}\right) = \Lambda(T)\frac{\partial(\theta\bar{\rho}H)}{\partial X} + \frac{\partial(\theta\bar{\rho}H)}{\partial T}
\tag{2.21}
$$

with

$$
\bar{\lambda} = \frac{12 u_m \eta_0 a}{c^2 p_H}
\tag{2.22}
$$

$\Lambda(T)$ is a dimensionless parameter that represents the change of the velocity in time, relative to the nominal velocity u_m. For example, in the case of a start up problem with a certain acceleration considered and $T > 0$, $\Lambda(T)$ is given by:

$$
\Lambda(T) = \frac{\bar{u}(t)}{u_m}
\tag{2.23}
$$

with $\bar{u}(t)$ the momentary entrainment speed.

The dimensionless boundary conditions reads:

$$
\theta(X_a, Y, T) = \frac{H_{oil}(X_a, Y, T)}{H(X_a, Y, T)}.
\tag{2.24}
$$

and the dimensionless cavitation condition:

$$
P(X, Y, T) \geq 0; \quad \forall (X, Y, T) \in D
\tag{2.25}
$$

For starved lubrication the complementarity condition should hold such that in pressurized regions $\theta = 1$ and in regions of zero pressure the variable θ has to be solved as follows:

$$P(X, Y, T)(1 - \theta(X, Y, T)) = 0 \tag{2.26}$$

Substitution of the dimensionless variables in the film thickness equation (2.4) leads to the dimensionless film thickness equation for *wide elliptic* contacts as follows:

$$H(X, Y, T) = -\Delta(T) + Z(X, Y) - \mathcal{R}(X, Y, T) + \tag{2.27}$$
$$+ \frac{1}{\pi I\!K} \iint_D \frac{P(X', Y', T)}{\sqrt{\kappa^2(X - X')^2 + (Y - Y')^2}} dX dY$$

and for *narrow elliptic contacts*

$$H(X, Y, T) = -\Delta(T) + Z(X, Y) - \mathcal{R}(X, Y, T) + \tag{2.28}$$
$$+ \frac{1}{\pi I\!K} \iint_D \frac{P(X', Y', T)}{\sqrt{\frac{1}{\kappa^2}(X - X')^2 + (Y - Y')^2}} dX dY$$

The dimensionless force balance condition gives:

$$\frac{3}{2\pi} \iint_D P(X, Y) dX dY = 1 \tag{2.29}$$

For the density from Equation (2.10) the following dimensionless density-pressure relationship is obtained

$$\overline{\rho} = \frac{5.9 \cdot 10^8 + 1.34 \cdot p_H \cdot P}{5.9 \cdot 10^8 + p_H \cdot P} \tag{2.30}$$

The Roelands relation in dimensionless terms is obtain from Equation (2.9) as

$$\overline{\eta}(p) = exp\left\{ [ln(\eta_0) + 9.67] \left[-1 + \left(1 + \frac{p_H}{p_r} P \right)^z \right] \right\} \tag{2.31}$$

In the literature different sets of dimensionless parameters are used to reduce the number of variables involved in the EHL equations and deliver a curve that is easy to use in the engineering practice (see Hamrock and Dowson [29, 30, 31] Chittichen [11], Greenwood [27]). Moes introduced in [54] a set of dimensionless parameters and curve fits complying with the need of a minimum number of similarity parameters. For elliptic contacts Moes's parameters are given by

$$M = \frac{F\mathbb{D}^{1/2}}{E'R_x^2}\left(\frac{\eta_0 u_s}{E'R_x}\right)^{-4/3} \tag{2.32}$$

and

$$L = \alpha E'\left(\frac{\eta_0 u_s}{E'R_x}\right)^{1/4} \tag{2.33}$$

The relation between the parameters $\overline{\lambda}$ and $\overline{\alpha}$ appearing in the dimensionless equations and Moes' dimensionless parameters M and L and the ellipticity parameters κ, $\mathbb{K}$ and $\mathbb{E}$ is given by:

$$\overline{\lambda} = \left(\frac{128\pi^3}{3M^4}\right)^{1/3}\left(\frac{16\pi(\mathbb{E} - \kappa^2\mathbb{K})^5}{\kappa^4(1-\kappa^2)^5\mathbb{K}^6}\right)^{1/3} \tag{2.34}$$

$$\overline{\alpha} = \frac{L}{\pi}\left(\frac{3M}{2}\right)^{1/3}\left(\frac{\pi^2\kappa(1-\kappa^2)^2}{16(\mathbb{E}-\kappa^2\mathbb{K})^2}\right)^{1/3} \tag{2.35}$$

As a result of scaling, for the simplest case of incompressible lubricant and using the Barus equation, the dimensionless film thickness H and pressure P are a function of $\overline{\alpha}$, $\overline{\lambda}$, κ and H_{oil}. This is a substantial improvement since in their dimensional form the characteristic parameters such as film thickness h and pressure p were dependent on: u_m, η_0, ρ_0, α, z, R_x, R_y, E', F and h_{oil}. Moreover, the equations in the dimensionless form (2.20) to (2.31) make the numerical process easier to handle and reduce the number of computations needed for the parameter study. For the case of a compressible lubricant and using the Roelands equation also α, z has to be given.

2.5 State of the art in EHL theory

The state of the art (2005) regarding the EHL theory is presented here in order to link the available models with the results obtained in the present study. This section represents the basis of the findings from the following chapters.

2.5.1 Survey diagrams

Survey diagrams, curve fits, analytical curve fits and rules of thumb ([15], [11]) are widely applied in the engineering practice. Based on asymptotic solutions and curve fits of numerical solutions ([70, 71, 72]), Moes, [54, 57] presented a survey diagram for EHL at line, point and elliptic contacts, see Appendix A. In these diagrams the asymptotic solutions are series of analytical curve fits which can be easily distinguished. The diagram gives a good and immediate estimate of the EHL contact performance.

2.5.2   State of starved lubrication theory

Valuable predictions of how EHL contacts respond to lubricant starvation are provided by Wedeven et al. [79], Chiu [12], Chevalier et al. [9], etc. An early measure of degree of starvation was given by Wedeven [79] in terms of the inlet distance S:

$$S = \left(\frac{h_{oil}/h_{cen} - 1}{1.21} \right)^{2/3} \frac{(R\, h_{cen})^{2/3}}{a^{1/3}} \tag{2.36}$$

For ratios $h_{oil}/h_{cen} \geq 9$ the EHL contact could be considered fully flooded and the inlet length (pressure buildup distance) was calculated by Wedeven [79]:

$$S_{ff} = 3.52 \frac{(R\, h_{cen})^{2/3}}{a^{1/3}} \tag{2.37}$$

A semi-empirical formula for determination of film thickness in starved conditions was provided:

$$\frac{h_{cen}}{R} = 1.73 \left[\frac{S}{S_{ff}} \left(2 - \frac{S}{S_{ff}} \right) \right]^{1/2} \left(\frac{\alpha \eta_0 u_m}{R} \right) \left(\frac{F}{E' R^2} \right) \tag{2.38}$$

The greatest practical problem in applying Equation (2.38) is the determination of the inlet distance for a particular application. Transport and distribution of lubricant, bearing dynamics and geometry were recommended as topics of future research.

Using a numerical approach, Chevalier [10], [9] related the dimensionless film thickness H_{cs} in starved conditions with the dimensionless thickness of the layer of incoming oil, H_{oil} by:

$$I\!R = \frac{r}{\sqrt[\gamma]{1 + r^\gamma}} \tag{2.39}$$

with γ a dimensionless parameter representing the resistance to side flow and $r = H_{oil}/H_{cff}$.

Chevalier concluded that EHL contacts are very efficient in terms of using the available lubricant. Very little is needed to form a full lubricant film, most of the available lubricant 'flows' through the contact when very small amounts of lubricant are supplied. For vanishing values of H_{oil}, the hydrodynamic pressure converges to the Hertzian pressure and the film thickness converges to $H_{oil}/\overline{\rho}(p_H)$. That means that the EHL film thickness is the same as the film in front of the contact (with a minor correction related to the compressibility of the lubricant). If the contact is severely starved, the location of the meniscus is closer to the Hertzian contact circle, therefore, pressure build-up is delayed, causing very steep pressure and viscosity gradients in the inlet of the contact. As the viscosity increases very fast, the left hand-side of the Reynolds equation (2.20) will be reduced very quickly compared to the right hand side, and the lubricant is only allowed to flow straight through the
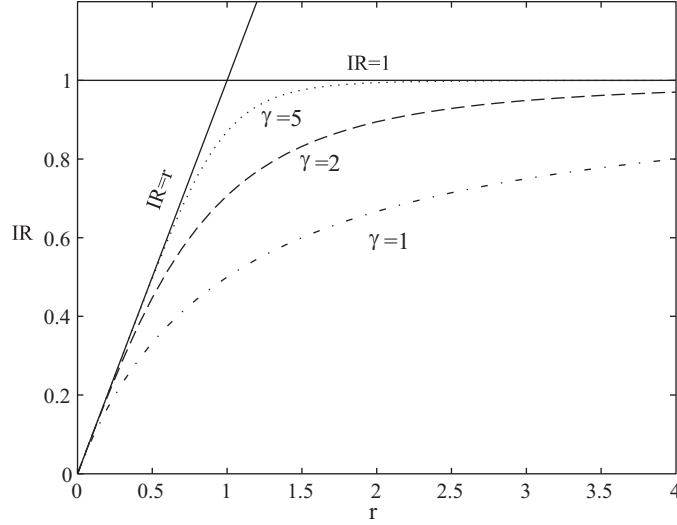
FIGURE 2.4: *Evolution of $\mathbb{R} = H_{cs}/H_{oil}$ as a function of $r = H_{cff}/H_{oil}$ for different values of γ*

contact. Figure 2.4 shows a plot of the degree of starvation $\mathbb{R} = H_{cs}/H_{cff}$ as function of relative lubricant layer thickness ($r = H_{oil}/H_{cff}$) for given operating conditions (M and L) reflected by γ. Two asymptotes $\mathbb{R} = 1$ and $\mathbb{R} = r$ can be distinguished: for increasing values of H_{oil} the solution converges to fully flooded films ($\mathbb{R} = 1$), whereas for vanishing values of H_{oil}, the solution converges to the dry contact solution ($\mathbb{R} = 0$). According to Damiens [18], the influence of the operating conditions (reflected by γ) is a function of the length of the pressure build-up zone upstream from the Hertzian area. Physically, the dimensionless parameter γ represents the resistance of the contact to the lubricant passing around it. A small inlet length (S) implies a relatively large value of γ, as the lubricant is quickly frozen and has little opportunity to escape. This corresponds with the asymptote $\mathbb{R} = r$ from Figure 2.4. On the other hand the lubricant easily escapes the contact if the inlet length is large, reaching after the asymptote $\mathbb{R} = 1$. Damiens [18] also gives a new relationship between the operating conditions and the inlet length (in a dimensionless form) for elliptic contacts:

$$\overline{S}_{ff} = C\sqrt{\frac{\mathbb{E}}{\kappa(1+\mathbb{D})}}\sqrt{\frac{L}{M}} \qquad (2.40)$$

with $C = 2^{-3/2}3^{-5/4}\pi^2\kappa^{-1/2}$

2.5.3   State of amplitude modification theory

In order to prevent metal-to-metal contact between surfaces in relative motion it is essential to predict how the micro-geometry or roughness deforms for different operating conditions. A first option for the study of the effects of the micro-geometry is to use the measured surface profile as an input. With the present multilevel solvers this is possible with reference to stability and computing time. This approach is however not recommended as it leads to several problems. Firstly the accuracy of the simulation for high frequency (small wavelength) surface features is difficult to control. Secondly to obtain general design rules valid in engineering practice a very large number of simulations are needed to test different types of micro-geometries. As a result, the enormous amount of data generated will make an extraction of general engineering rules predicting the effect of surface roughness very difficult. An alternative approach was taken by Venner et al. [73]. Instead of studying the measured surface profiles, the deformation of simple harmonic components for pure rolling conditions was studied.

Surface waviness

Based on understanding how harmonic waves deform in the high pressure region of EHL contacts for different operating conditions an amplitude reduction model is already available, Venner [73], Hooke [36], [37], [38]. Using Fourier Transforms the surface micro-geometry is decomposed in harmonic functions, followed by an estimate of the deformed harmonics with the amplitude modification model as function of the running conditions. Subsequently with inverse Fourier Transforms the deformed micro-geometry inside the contact can be found and the probability of metal to metal contact estimated, see Masen et al. [53]. Venner and Morales [74] showed that accurate amplitude reduction predictions can be obtained for two sided waviness on the basis of the results obtained for single sided waviness. Venner, Berger et al., [76], extended the model to starved lubrication with a constant thickness lubricant layer (Figure 2.5). An *amplitude reduction* curve was found, predicting how harmonic waves deform for different operating conditions and degrees of starvation. This is reflected by a dimensionless operating conditions parameter as follows:

$$\overline{\nabla} = \frac{\mathcal{W}_{X,Y}}{\sqrt{L/M} \cdot I\!R^{3/2}} \tag{2.41}$$

with $\mathcal{W}_{X,Y}$ the dimensionless wavelength of the surface waviness in X or Y direction.

The effect of surface micro-geometry in starved condition (uniform oil layer, [76]) was described by:
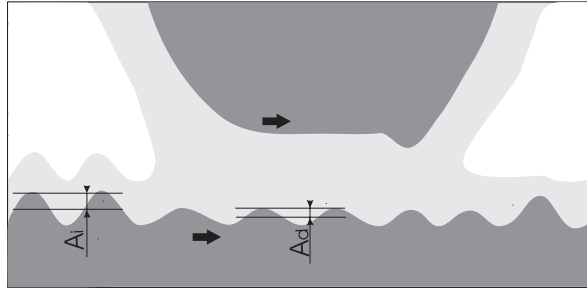
FIGURE 2.5: *Constant thickness lubricant layer following the surface features* $(H_{oil} = constant)$

$$\frac{A_d}{A_i} = \frac{1}{1 + 0.15\overline{\nabla} + 0.015\overline{\nabla}^2} \qquad (2.42)$$

with A_i and A_d the initial and the deformed amplitude of the waviness respectively.

Figure 2.6, presents Venner's findings. The model shows that for values of $\overline{\nabla}$ below 1 the surface waviness is hardly deformed while it is travelling through the contact. On the other hand, when $\overline{\nabla}$ exceeds 50 the surface features are completely flattened. In physical terms this means that for given operating conditions the amplitude of long waves harmonic components are considerably reduced. Short waves tend to minimize the deformation of the surface waviness. With an increasing degree of starvation $\overline{\nabla}$ increases and the deformation of the harmonic profile becomes increasingly important. Since the inlet length is proportional to $\sqrt{L/M}$ (2.40) the amplitude modification ratio A_d/A_i will also be affected by the load and lubrication conditions.
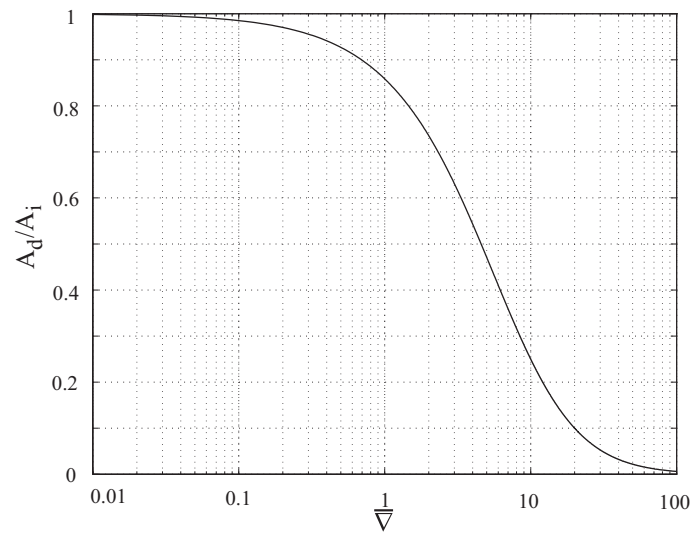
FIGURE 2.6: *Amplitude reduction curve for starved lubrication for a wavy surface and a constant thickness inlet layer*

METHODS

For the study of elasto-hydrodynamic lubrication various numerical and experimental methods have been developed. For transient and starved lubrication the most successful are, no doubt, the *Multilevel Methods* and the *Optical Interferometry Techniques*. Both techniques can be adapted to the study of specific problems involved in transient and starved lubrication, generate detailed maps of lubricant film thickness and pressure distribution and allow parameter studies. In this chapter a description of these methods is given.

3.1 Numerical Methods

The equations presented in Chapter 2 have analytical solutions only for simplified asymptotic cases. Generally a numerical approach is required. To solve the governing equations numerically it is necessary to recast the problem into a purely algebraic form, involving only the basic arithmetic operations. To achieve this, *finite differences* are used for the discretization of the continuum problem, replacing each derivative in the equation by truncated Taylor series. Subsequently, the resulting system of equations for the unknowns at each of the grid points is solved by computer using Multilevel techniques, see [75].

3.1.1 Discrete equations

The computational domain is discretized using a uniform grid with the mesh size h_X and h_Y in the X and Y direction, respectively. The grid points are $X_i = X_a + ih_X$ and $Y_j = Y_a + jh_Y$ for $i \in [0, n_X]$ and $j \in [0, n_Y]$. The time line is given by $T = T_0 + kh_T$, with T_0 the initial time point, h_T the time step and $k \in [0, n_T]$.

The first and second term ($Poiseuille$ terms) of the Reynolds equation (2.20) and (2.21) denoted by Q_x and Q_y, respectively, are approximated at each grid point using a *central second order* discretization (see Figure 3.1).

$$Q_x \equiv \frac{\xi_E P^h_{i+1,j,k} - (\xi_E + \xi_W)P^h_{i,j,k} + \xi_W P^h_{i-1,j,k}}{h_X^2} \tag{3.1}$$

$$Q_y \equiv \frac{\xi_N P_{i,j+1,k}^h - (\xi_N + \xi_S)P_{i,j,k}^h + \xi_S P_{i,j-1,k}^h}{h_Y^2} \tag{3.2}$$

for *wide elliptic contacts*

$$
\begin{aligned}
\xi_N &= \kappa^2 \frac{1}{2\lambda}\left(\frac{\overline{\rho}(P_{i,j+1,k})H_{i,j+1,k}^3}{\overline{\eta}(P_{i,j+1,k})} + \frac{\overline{\rho}(P_{i,j,k})H_{i,j,k}^3}{\overline{\eta}(P_{i,j,k})}\right) \\
\xi_S &= \kappa^2 \frac{1}{2\lambda}\left(\frac{\overline{\rho}(P_{i,j-1,k})H_{i,j-1,k}^3}{\overline{\eta}(P_{i,j-1,k})} + \frac{\overline{\rho}(P_{i,j,k})H_{i,j,k}^3}{\overline{\eta}(P_{i,j,k})}\right)
\end{aligned}
\tag{3.3}
$$

for *narrow elliptic contacts*

$$
\begin{aligned}
\xi_N &= \frac{1}{\kappa^2} \frac{1}{2\lambda}\left(\frac{\overline{\rho}(P_{i,j+1,k})H_{i,j+1,k}^3}{\overline{\eta}(P_{i,j+1,k})} + \frac{\overline{\rho}(P_{i,j,k})H_{i,j,k}^3}{\overline{\eta}(P_{i,j,k})}\right) \\
\xi_S &= \frac{1}{\kappa^2} \frac{1}{2\lambda}\left(\frac{\overline{\rho}(P_{i,j-1,k})H_{i,j-1,k}^3}{\overline{\eta}(P_{i,j-1,k})} + \frac{\overline{\rho}(P_{i,j,k})H_{i,j,k}^3}{\overline{\eta}(P_{i,j,k})}\right)
\end{aligned}
\tag{3.4}
$$

and

$$
\begin{aligned}
\xi_E &= \frac{1}{2\lambda}\left(\frac{\overline{\rho}(P_{i+1,j,k})H_{i+1,j,k}^3}{\overline{\eta}(P_{i+1,j,k})} + \frac{\overline{\rho}(P_{i,j,k})H_{i,j,k}^3}{\overline{\eta}(P_{i,j,k})}\right) \\
\xi_W &= \frac{1}{2\lambda}\left(\frac{\overline{\rho}(P_{i-1,j,k})H_{i-1,j,k}^3}{\overline{\eta}(P_{i-1,j,k})} + \frac{\overline{\rho}(P_{i,j,k})H_{i,j,k}^3}{\overline{\eta}(P_{i,j,k})}\right)
\end{aligned}
\tag{3.5}
$$

For the remaining terms of (2.20) (the wedge and the squeeze term) a *narrow upstream second order* ($NU2$) discretization scheme is used.

for $h_X \leq h_T$ the discrete squeeze term gives

$$
\begin{aligned}
H_x + H_t &\equiv \frac{1.5\overline{\rho}(P_{i,j,k}^h)H_{i,j,k}^h - 2\overline{\rho}(P_{i-1,j,k}^h)H_{i-1,j,k}^h + 0.5\overline{\rho}(P_{i-2,j,k}^h)H_{i-2,j,k}^h}{h_X - h_T} + \\
&\quad + \frac{1.5\overline{\rho}(P_{i,j,k})H_{i,j,k} - 2\overline{\rho}(P_{i,j,k-1})H_{i,j,k-1} + 0.5\overline{\rho}(P_{i,j,k-2})H_{i,j,k-2}}{h_T}
\end{aligned}
\tag{3.6}
$$

and for $h_X > h_T$

$$
\begin{aligned}
H_x + H_t &\equiv \frac{1.5\overline{\rho}(P_{i,j,k}^h)H_{i,j,k}^h - 2\overline{\rho}(P_{i-1,j,k}^h)H_{i-1,j,k}^h + 0.5\overline{\rho}(P_{i-2,j,k}^h)H_{i-2,j,k}^h}{h_X} + \\
&\quad + \frac{1.5\overline{\rho}(P_{i,j})H_{i,j,k} - 2\overline{\rho}(P_{i,j,k-1})H_{i,j,k-1} + 0.5\overline{\rho}(P_{i,j,k-2})H_{i,j,k-2}}{h_T - h_X}
\end{aligned}
\tag{3.7}
$$
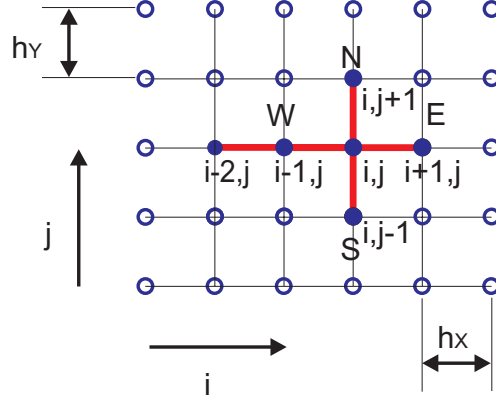
FIGURE 3.1: *Discretization schemes: central second order involving the points* (i, j), $(i-1, j)$, $(i+1, j)$, $(i, j-1)$, $(i, j+1)$ *and upstream second order involving* (i, j), $(i-1, j)$, $(i-2, j)$

The advantage of the $NU2$ scheme compared to a *standard second order upstream* discretization $(SU2)$ is that the former does not show (artificial) numerical damping. The $NU2$ stencil has a zero leading error term for several directions (including $X = T$), producing more accurate transient solutions. For more details the reader is referred to Wijnant [83] and Venner [75].

The discrete Reynolds equation is then given by

$$L_{i,j,k}\langle\overline{P}\rangle = Q_x + Q_y - H_x - H_t = \langle f^h_{i,j,k}\rangle_P \qquad (3.8)$$

The discrete gap height equation reads

$$H_{i,j,k} = H_0 + Z(X_i, Y_j, T_k) + \sum_{l=0}^{n_X}\sum_{q=0}^{n_Y} K_{i,l,j,q}P_{i,j,k} \qquad (3.9)$$

The multi-summation in (3.9) represents the discretized elastic deformation integral (2.12) $K_{i,l,j,q}$, which depends on the distance between the points where the pressure acts (l, q) and the points in which the deformation is calculated (i, j), assuming a constant pressure on the rectangles $h_X \times h_Y$ centered around each grid point, given by

$$\begin{aligned}
K_{i,l,j,q} = \tfrac{1}{\pi I\!\!K} \Big\{ &|X_p|\text{arcsinh}\left(\tfrac{Y_p}{X_p}\right) + |Y_p|\text{arcsinh}\left(\tfrac{X_p}{Y_p}\right) \\
&-|X_m|\text{arcsinh}\left(\tfrac{Y_p}{X_m}\right) + |Y_p|\text{arcsinh}\left(\tfrac{X_m}{Y_p}\right) \\
&-|X_p|\text{arcsinh}\left(\tfrac{Y_m}{X_p}\right) + |Y_m|\text{arcsinh}\left(\tfrac{X_p}{Y_m}\right) \\
&+|X_m|\text{arcsinh}\left(\tfrac{Y_m}{X_m}\right) + |Y_m|\text{arcsinh}\left(\tfrac{X_m}{Y_m}\right) \Big\}
\end{aligned} \qquad (3.10)$$

for *wide elliptic contacts*

$$X_p = X_i - X_l + h_X/2 \qquad X_m = X_i - X_l - h_X/2$$
$$Y_p = (Y_j - Y_q + h_Y/2)/\kappa \quad Y_m = (Y_j - Y_q + h_Y/2)/\kappa \tag{3.11}$$

and for *narrow elliptic contacts*

$$X_p = X_i - X_l + h_X/2 \qquad X_m = X_i - X_l - h_X/2$$
$$Y_p = (Y_j - Y_q + h_Y/2) \cdot \kappa \quad Y_m = (Y_j - Y_q + h_Y/2) \cdot \kappa \tag{3.12}$$

A second-order approximation of the force balance equation is given by

$$\frac{3}{2\pi} h_X h_Y \sum_{i=0}^{n_X} \sum_{j=0}^{n_Y} P_{i,j} = 1 \tag{3.13}$$

3.1.2 Multigrid

Apart from being governed by a complex system of equations, the EHL problem also requires a high resolution solution. Furthermore, the non-linearity of the system of equation and the change from differential to integral character requires a stable solution method. A detailed and well-written motivation for application of Multigrid techniques in EHL, details about implementation, the iterative process, distributive relaxation techniques and other details of this subject are given by Venner and Lubrecht [75].

The fundamental idea behind Multigrid methods is to use different grids in order to reduce error components on different scales. The error components with a wavelength of the same order as the mesh size (high frequency components) are efficiently reduced by the classical iterative methods, but the error is hardly reduced if the wavelength is larger than the mesh size (low-frequency components). Therefore, instead of continuing the iteration process on the fine grid one can switch to a coarser grid for the solution of the error and then the approximation obtained on the coarser mesh is used to correct the solution on the fine grid. If the mesh size of the coarse grid is still too small the convergence of the process will slow down again after a few iterations and one can switch to an even coarser grid until a grid is reached on which the problem can be solved in a few iterations only. The equation from which the error is solved on the coarse grid is the same as the original fine grid problem except for the right hand side, which is now constructed from the fine grid residuals.

In order to transfer the problem right hand sides and the solutions of the error from one grid to the next, *inter-grid operators* are used. A *restriction operator* is used to transfer the residual from the fine grid to the coarse grid in order to obtain a coarse grid representation of the residual. An *interpolation operator* is used to determine the value of the approximation on the fine grid by interpolation of a group of neighbor points from the coarse grid. The process of going from fine to coarse grids and back again is referred to as *cycle* and can be carried out until the reduction

of error per relaxation falls below some prescribed value. In order to smooth the error, before coarsening on each grid, ν_1 iterations are performed. Once the coarsest grid is reached ν_0 iterations are performed to solve the set of equations, then ν_2 iterations are carried out to remove the errors introduced by the interpolation. Typical values for ν_1, ν_0 and ν_2 are 2, 40, and 1, respectively.

3.1.3   Relaxation schemes

The character of the EHL problem changes in the computational domain from elliptic to hyperbolic. This requires two types of relaxations schemes depending on the character of the problem. For the high pressure region the terms Q_x and Q_y are very small compared with $H_x + H_t$, the model problem being dominantly hyperbolic. Here, a *Jacobi distributive* relaxation scheme is applied. For the rest of the domain the terms Q_x and Q_y dominate, this giving an elliptic character to the model problem. Gauss-Seidel line relaxation is well known to give good smoothing properties for the elliptic type problems and this is the relaxation scheme adopted for the low pressure regions. Using these relaxation schemes the unknowns $P_{i,j}$ along each line are updated line by line, in the high pressure region the neighboring lines being also updated. The new approximation of $P_{i,j}$ is then used to evaluate $H_{i,j}$. The changes $\delta_{i,j}$ to be applied at a given line j are solved from a system of equations of the form:

$$A_j \cdot \overline{\delta}_j = \overline{r}_j \qquad (3.14)$$

The residual vector $\overline{r}_j$ and the coefficients $A_{i,k}$ of the matrix A_j are given by the type of relaxation applied, see Appendix B. Depending on the region of the computational domain the unknowns are updated either by Gauss-Seidel line or Jacobi distributive line relaxation. If condition (3.15) is fulfilled Jacobi distributive line relaxation is applied, for the other points Gauss-Seidel line relaxation is used, see [75].

$$|\xi_N/h_Y^2|, |\xi_S/h_Y^2|, |\xi_E/h_X^2|, |\xi_W/h_X^2| \le \xi_{limit} \qquad (3.15)$$

3.1.4   Ellipticity

Depending on the value of κ we can deal with a *circular contact* ($\kappa = 1$), a *wide elliptic contact* ($\kappa < 1$) or a *narrow elliptic contact* ($\kappa > 1$). For circular contacts *point* wise relaxation schemes are good enough to smooth the error in both directions (see [75]). For elliptic contacts a local mode spectral analysis of the system of equations suggests that the optimal iterative method for the EHL elliptic problems is *line* relaxation, see [83]. As mentioned above line relaxation schemes are necessary for elliptic contacts. Along which lines the relaxation process should take place depends on the ellipticity factor κ.

There are three groups of terms characterizing the nature of the Reynolds equation at a given time step. The term Q_x (3.1) is determined by the pressure P in points

(i, j), $(i - 1, j)$ and $(i + 1, j)$ (see Figure 3.1). The term Q_y (3.2) is defined by the pressure P in points (i, j), $(i, j - 1)$ and $(i, j + 1)$. Finally the wedge term (H_x) is defined by gap height H in the points (i, j), $(i - 1, j)$ and $(i - 2, j)$.

In the H_x term the points are coupled on line i (x direction), while for the *Poiseuille* terms (Q_x and Q_y) the coupling depends on the nature of the problem. A $\kappa < 1$ indicates a strong coupling, in x direction. In this case the choice for x line relaxation is obvious, as all terms (Q_x, Q_y and H_x) demand this. By solving a complete x *line* at once the coupling of all points on one line is combined, assuring good error smoothing by the iterative process. The line relaxation solves (completely) the system of equations from one line by means of Gaussian elimination with partial pivoting.

For $\kappa > 1$ the term Q_y is dominant and the coupling is weak in x direction and strong in y direction. In this case choosing the relaxation direction is less straightforward. The weight of the term H_x in relation to the terms Q_x and Q_y is determined by the factor ξ which has different values over the computational the domain. In the contact region ξ is small and the equation will be determined then by the terms H_x, distributive line relaxation in x direction being preferred here. Outside the contact region ξ is large and the *y direction* may give better convergence. Instead of choosing one direction for this area, alternating x and y relaxations are chosen in order to make smoothing robust. In Appendix B, implementation details of relaxation schemes are given for the x and y direction.

3.1.5   Starved lubrication

The numerical approach for the starved lubrication is not very much different from the problem of the fully flooded contact. The difference is that the relaxation is done on θ in the cavitated region and on P in the pressurized region by applying the changes $\delta_{i,j}$ either for $\theta_{i,j}$ or for $P_{i,j}$. Since θ can not exceed unity ($h_{oil} \leq h$) and pressure cannot drop below ambient pressure ($P \geq 0$), after one relaxation sweep P and θ are set to 0 and respectively 1 if the above mentioned conditions are not fulfilled. These complementary conditions can make the relaxation scheme to swap between different solutions and destabilize the numerical process. A cure for this instability can be achieved by an immediate relaxation on the new variable.

For example, if a new approximation $\theta_{i,j}$ exceeds unity its value is set to 1 and a new update $P_{i,j}$ is determined by means of point wise Gauss-Seidel relaxation. On the other hand if after one relaxation sweep $P < 0$ the pressure is set to zero a new approximation of $\theta_{i,j}$ is calculated. If the new update $\theta_{i,j} > 1$ its value is set to 1.

The discrete modified Reynolds equation will have then the term $H_x + H_t$ for $h_X \leq h_T$ given by:

$$H_x + H_t \equiv \left[1.5\theta\overline{\rho}H_{i,j,k}^h - 2\theta\overline{\rho}H_{i-1,j}^h + 0.5\theta\overline{\rho}H_{i-2,j,k}^h \right] \left(\frac{1}{h_X} - \frac{1}{h_T} \right) +$$

$$+ \left[1.5\theta\overline{\rho}H_{i,j,k} - 2\theta\overline{\rho}H_{i-1,j,k-1} + 0.5\theta\overline{\rho}H_{i-2,j,k-2} \right] \left(\frac{1}{h_T} \right) \tag{3.16}$$

and for $h_X > h_T$

$$H_x + H_t \equiv \left[1.5\theta\overline{\rho}H_{i,j,k}^h - 2\theta\overline{\rho}H_{i-1,j}^h + 0.5\theta\overline{\rho}H_{i-2,j,k}^h \right] \left(\frac{1}{h_X} \right) +$$

$$+ \left[1.5\theta\overline{\rho}H_{i,j,k} - 2\theta\overline{\rho}H_{i,j,k-1} + 0.5\theta\overline{\rho}H_{i,j,k-2} \right] \left(\frac{1}{h_T} - \frac{1}{h_X} \right) \tag{3.17}$$

For different EHL problems the performance of the numerical process varies with load conditions but on average a factor two per cycle is obtained. This is sufficient to have a solution with an error small compared to the discretization error in few cycles. An example of converged solution for a starved EHL problem is presented in Figure 3.2. The figure shows a contour plot of the dimensionless pressure P, gap height H, factional film content θ and the product $\theta \times H$. The last can be interpreted as a foot print of the contact. The results are obtained for a variable thickness of the oil layer at the inlet region $H_{oil}(Y)$. The load parameters are $M = 100$, $L = 5$, lubrication parameters: $\overline{H}_{oil}/H_{cff} = 1$, $\mathcal{W}_Y = 0.5$.

3.2 Experimental Methods

For model EHL contacts, a ball immersed in oil and loaded against a flat moving surface is the simplest EHL experiment that can be imagined. As simple as it is, employing such a setup needs much preparation. Assuring smooth functioning, reliability and repeatability of the measurements are critical for comparison of experimental results with numerical calculations. Additionally, the surfaces need to be as smooth as possible and hard enough to endure the high surface stress, free of dust particles, finger prints, etc. Easy access for cleaning and oil evacuation are also important. Moreover, to quantify the performance of such a contact an accurate measurement method is required.

An experimental rig that fulfills these requirements was developed at Imperial College, based on the research carried out by Foord [22], Cameron [8], Wedeven [78], Johnson, Wayte, Spikes, [46], Cann [5], etc. An identical setup is used for the experimental part of this thesis.
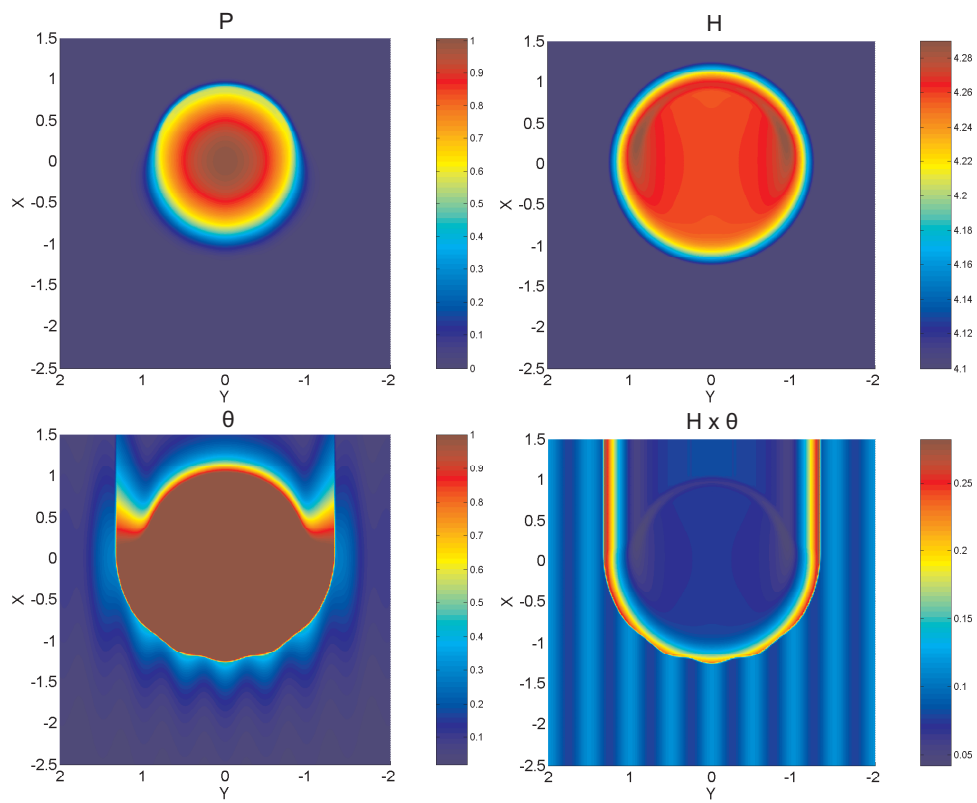
FIGURE 3.2: *Example of converged solution:* $M = 100$, $L = 5$, $\overline{H}_{oil}/H_{cff} = 1$, $\mathcal{W}_Y = 0.5$
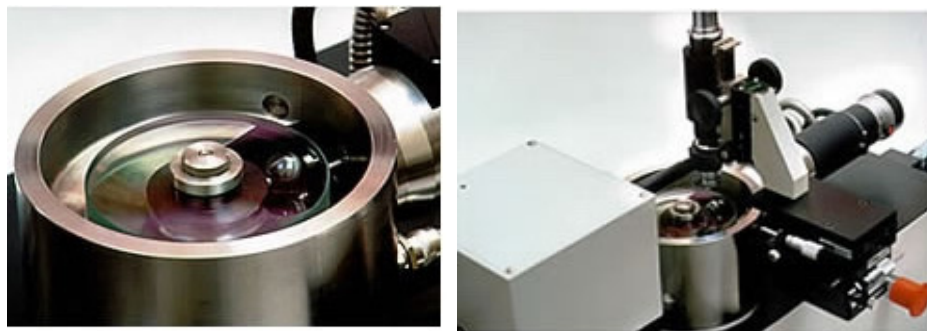
FIGURE 3.3: *Overview of the mechanical part with the steel ball in place, with and without the microscope assembly*

The main component of the experimental equipment is the *mechanical part*, with a pot in which the steel ball/roller can be placed on a carriage. The load is applied on the rolling element from the under side of the pot via the carriage. The disc mounted on a shaft driven by an electric motor is glass made and coated as described below. In pure rolling conditions the rolling element rotates freely on the carriage. It can also be driven by an independent electric motor when slip is investigated. When fully flooded conditions are desired the rolling element is immersed in oil. For starved lubrication experiments only a limited amount of oil is placed on the running track of the disc. A number of 20 tracks can be selected on the disc, with radii ranging from $34[mm]$ to $44[mm]$. An overview of the pot with the disc and the ball on place is shown in Figure 3.3 (left).

Optical interferometry is used used to measure the thickness of the oil film formed between the disc and the rolling element. For that purpose an assembly of optical lenses and a beam splitter allows visualization of the contact region illuminated with a cold halogen light source at $\theta_i \approx 0°$ angle of incidence via an optic fibre cable as shown in Figure 3.3 (right).

A strict cleaning procedure has to be followed for accurate measurements. For each set of measurements the disc and the rolling element are cleaned with toluene in a sonic bath, then ethanol is used to eliminate any traces of toluene. If the test oil is changed all the parts in contact with the oil (eg. the pot, ball/roller carriage, the loading system, etc.) need also cleaning as described above. Avoiding any fingerprints or dust particles on the surface of the disc and the rolling element is also important.

3.2.1   Thin film interference

In everyday life there are many examples of thin film interference. The most common are soap bubbles, oil or gasoline on the pavement (or water), optical coatings, etc. The observed color patterns are the result of interference of light waves reflecting from the top surface of a thin film with the waves reflecting from the bottom surface.
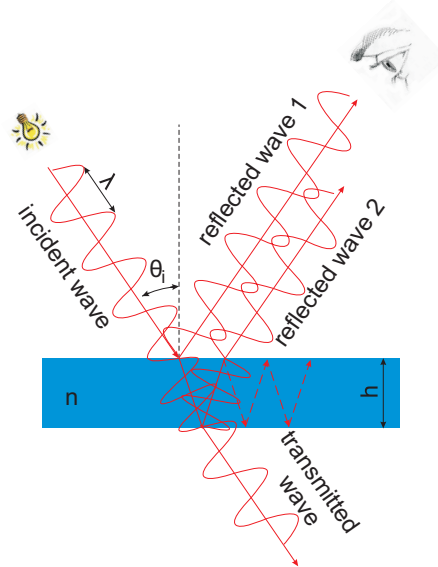
FIGURE 3.4: *Reflection and interference of light waves in a thin film*

A particular light wave (monochromatic light) passing through a dielectric film, changes its phase by an amount proportional to the optical path length, see Figure 3.4.

Depending on their wavelength (λ), thickness of the film (h) and refraction indices (n), light waves can interfere constructively according to

$$h = \frac{(N - \phi)\lambda}{2 \, n \, cos \, \theta_i} \qquad N = 1, 2, 3, ... \tag{3.18}$$

or destructively according to

$$h = \frac{(N + \frac{1}{2} - \phi)\lambda}{2 \, n \, cos \, \theta_i} \qquad N = 0, 1, 2, ... \tag{3.19}$$

with θ_i the incident angle and ϕ the relative change due to reflection.

That means that the reflected waves will add to each other (constructively) or subtract from each other (destructively) resulting in a series of bright and dark fringes. The same phenomena occur for each of the polychromatic light waves passing through the film, the result being a complex color spectrum instead of dark and bright fringes.

Both, monochromatic and polychromatic interferometry, are used to quantify thin layers of given applications. However, there are also limitations of the conventional optical interferometry.
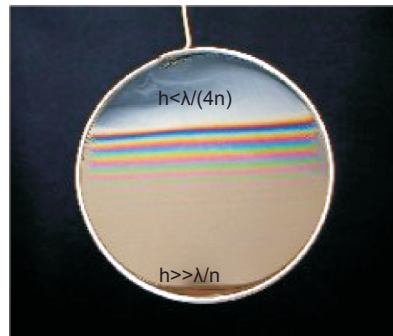
FIGURE 3.5: *Limitations of thin film interferometry: "wedge-shaped" soap membrane*

The thickness of the film to be measured by optical interferometry has to be in the order of the wavelength of the light wave. If the film is much thicker than the largest wavelength of the visible spectra, the fringes overlap making it impossible to distinguish between the different orders of interference. For the case of polychromatic light interferometry the overlapping between different waves takes place at even thinner films, the color separation becoming increasingly unclear as the film augments. On the other hand, according to (3.18) and (3.19), for normal incident waves ($\theta_i \approx 0°$) the minimum film thickness that can be evaluated is $\lambda/(4n)$.

So, films which are few times thicker than the largest visible wavelength (red light, $\lambda \approx 700[nm]$) or thinner than one-quarter of the lowest visible wavelength (blue light, $\lambda \approx 400[nm]$) are not measurable by conventional optical interferometry. This is illustrated in Figure 3.5 by showing a soap membrane which is very thin at the top and gets thicker towards the bottom, under the influence of gravity. Since the top part of the membrane is tinner than approximatively $70[nm]$, a dark-grey region is observed. As the thickness of the membrane increases, the reflected light waves interfere with each other constructively or destructively according to (3.18) or (3.19), respectively. After 4 or 5 fringes the presence of different colors at one point results in a white-grey region.

In addition to the limitations presented above, conventional interferometry has limitations regarding the resolution of the measurement. For films below $1000[nm]$ the reflecting colors can be identified to a resolution of $50[nm]$ for the case of white light interferometry and 150 to $200[nm]$ for the visible monochromatic fringes. For example, using a white light source the minimum measurable film thickness is $\approx 70[nm]$, the next measurable value are $\approx 120[nm]$, $170[nm]$, $220[nm]$, etc.

	air	MgF_2	glass	Cr	SiO_2	oil	steel
reflective index	≈ 1	1.38	1.52	≈ 1.49	1.45	≈ 1.4	∞
reflectance		1 %		18 %		60%	
transmittance		96 %		57 %		0 %	
absorbance		3 %		25 %		40%	

TABLE 3.1: *Reflective indices, reflectance, transmittance and absorbance for different materials and interfaces*

3.2.2 EHL Ultra thin measurement system

Because of the limitations explained above, the measurements of the ultra thin oil layers occurring in starved lubrication by conventional optical interferometry would be difficult if not impossible. The thickness of the oil layers is sometimes below $70[nm]$ and the relatively low resolution could lead to inaccurate measurements. Over the last few decades ingenious ways of surmounting these limitations were proposed, [22], [8], [78], [46]. Nowadays, EHL films can be measured down to a few nanometers with resolutions of $\pm 1[nm]$ if a number of conditions are fulfilled, which will be described bellow.

Primarily, the flat surface in an EHL contact has to be transparent and durable. For this purpose glass, sapphire or diamond discs are the favorite candidates. Depending on the magnitude of the contact stress, sensitivity to thermal conductivity and the costs involved one of the three can be selected.

Secondly, good fringe visibility is required for high accuracy measurements. In that respect an *anti-reflective* coating of MgF_2 (similar to lens coatings applied in photo cameras) improves transmittance of light through the disc. On the opposite side of the disc a *semi-reflective* chromium layer of about $20[nm]$ is deposited to equalize the intensities of reflected beams, and consequently to increase fringe visibility, see [78], [81].

Furthermore, a silica *spacer layer* on top of the chromium lifts the total film above the minimum measurable value ($\lambda/(4n)$), see [46]. In such an optical system, the thickness of the oil and the spacer layer can be measured according to

$$n_{oil}h_{oil} + n_{sp}h_{sp} = \frac{\left(N + \frac{1}{2} - \phi\right)\lambda}{2\,cos\,\theta_i} \tag{3.20}$$

Finally, the use of a spectrometer rather than observing the position of the interference fringes by eye allows to distinguish precisely different hues of the spectrum. This technique was successfully used by Johnson et al. [46] obtaining resolutions of $\pm 1[nm]$. The entire optical system is shown schematically in Figure 3.6. The reflective indices, reflectance, transmittance and absorbance for the materials and interfaces involved are shown in Table 3.1.

Figure 3.7 shows the reflected light waves from a dry contact directed by a beam
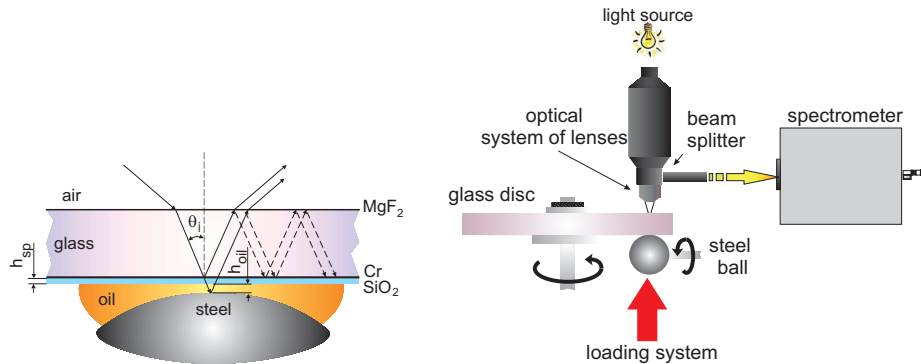
FIGURE 3.6: *Optical system with setup for EHL films measurements*
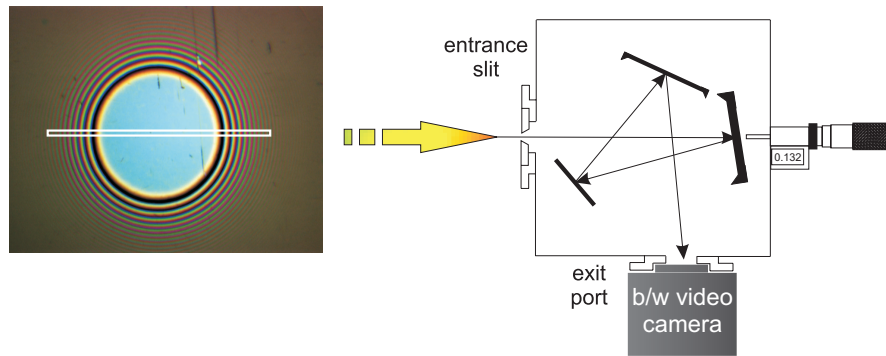
FIGURE 3.7: *Spectrometer used for determining the wavelength along the scanned profiles*

splitter to the spectrometer via a narrow slit. The spectrometer includes an optical configuration of lenses and mirrors, a separating element and an optic-mechanical device for the wavelength selection. By adjusting the movable mirror of the spectrometer, a specific wavelength can be selected so that the merging waves of that wavelength are exactly in phase. This will produce a maximum of brightness for that wavelength (color), which is captured by a black/white video camera and translated to a function of spectral intensity versus wavelength as shown in Figure 3.8. Finally, the wavelength for each pixel of the narrow aperture is obtained as shown in Figure 3.9. Please note that prior calibration of the spectrometer using a source of known wavelength (a mercury lamp for example) and the spectral response of the light source used for the measurements are required.

For the loaded dry contact between a steel ball and a glass disc (coated as described above), the thickness of the silica spacer layer can be found according to
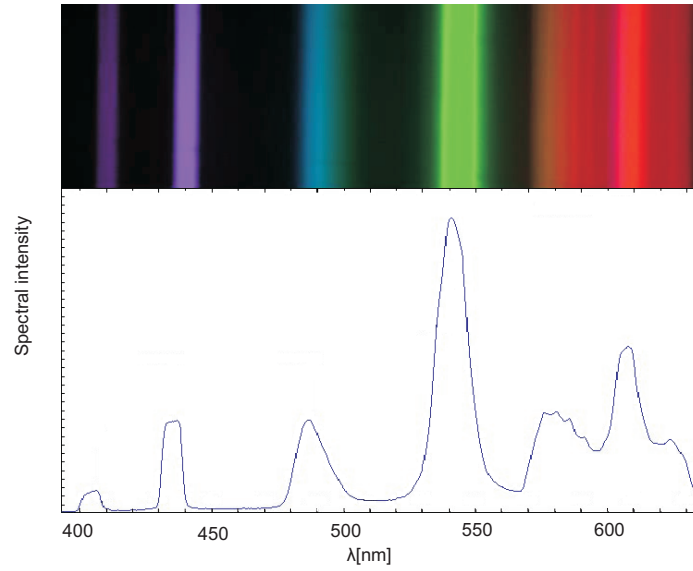
FIGURE 3.8: *Spectral intensity as function of wavelength*
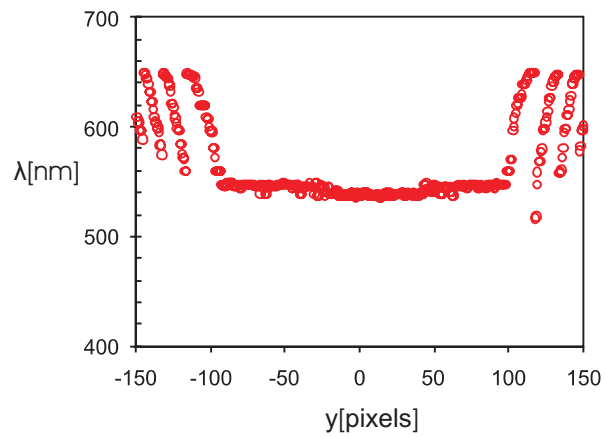
FIGURE 3.9: *Measured wavelength as function of pixel position*
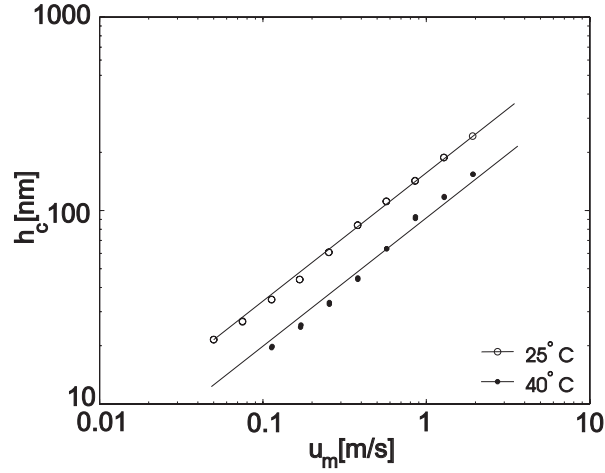
FIGURE 3.10: *Oil film thickness at the center of the contact as function of entrainment speed for TT9 at 25°C and at 40°C, loaded with 18[N]*

$$h_{sp} = \frac{(N - \phi)\lambda_{max}}{2n_{sp}} \tag{3.21}$$

The relative phase change ϕ due to reflection is given by the absolute phase change of the steel surface (ϕ_{steel}) and that of the chromium surface (ϕ_{Cr})

$$\phi = \phi_{steel} + \phi_{Cr} \tag{3.22}$$

For the optical system presented in Figure 3.6 the value of ϕ_{Cr} is close to $-\pi$ (i.e -3.12) and the resulting *relative* phase change $\phi \approx 0.02$. This corresponds with the the observation made by Wedeven [78], that the phase change due to reflection from the steel surface is $\phi_{steel} \approx \pi$ and ϕ_{Cr} is somewhere between 0 and $\pm\pi$.

Figure 3.10 shows the measured value of a lubricated film thickness at the center of the contact as function of the entrainment speed, u_m. The oil used is a standard mineral oil (TT 9). Results are shown for two temperatures ($25[°C]$ and $40[°C]$) and a load fixed at $18[N]$. A slope of approximately 0.67 can be observed in log-log plot, as predicted by Hamrock and Dowson [31].

3.2.3   Oil layer measurements

Although the optical setup presented above is meant for the oil films formed between surfaces in relative motion, with a few minor modifications it can also be used to evaluate the film thickness of the oil layer located on the disc, i.e. not in the contact itself.

Measurements of the thickness of lubricant film on the running track of a rotating glass disc were first attempted by Wedeven and coworkers [79]. It was observed
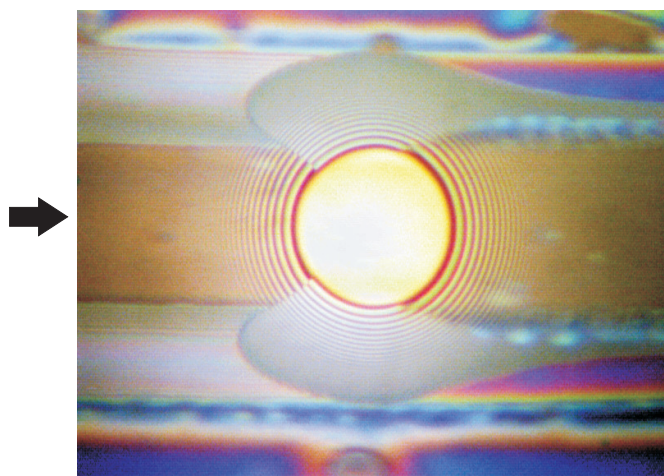
FIGURE 3.11: *Starved EHL contact operating with a limited amount of $TT9$ at $25[^\circ C]$ oil, 20[N]. The arrow indicates the direction of the flow.*

that in the outlet region of the EHL contacts narrow ribs of lubricant remain on the track while thin waves of lubricant form adjacent to the track. Chiu's [12] analysis of lubricant replenishment revealed that the degree of starvation depends strongly on the thickness of the oil layer around the rolling track. The numerical and theoretical work of Chevalier [10] showed that the film thickness in the contact center is dependent on how much oil is available in front of the contact. So, to predict film thickness in starved contacts inlet layer thickness is needed as input and exactly such information is often not available.

Optical interferometry seems to be the most suitable technique for this purpose. An image of the running track during an experiment with a limited amount of oil is shown in Figure 3.11. The concentric interference fringes around the contact area indicate an increase of gap height between the ball surface and the glass disc. Furthermore, the color shifts can be observed along the running track, indicating two side levees on the glass disc. The main idea behind a lubricant measurement technique is to use the propriety of electromagnetic waves to interfere when they pass through a dielectric film. If colors can be distinguished on the surface of a the dielectric film it means that interference of light takes place and the thickness of the film can be determined.

The experimental set up for oil layer thickness measurements is identical to that for the classical film thickness measurements presented above. Alternatively, monochromatic light with a narrow bandpass light filter can be employed to look at thicker oil layers. For the monochromatic light setup, the wavelength λ is a known constant over the sampled region. According to the optical interferometry principle the thickness of a thin layer (h) is given by (3.20).
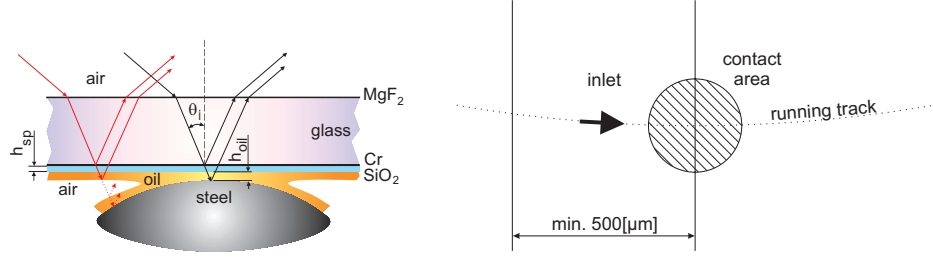
FIGURE 3.12: *Scan position in the inlet and center of the contact*

The phase change at reflection from the oil layer (or the silica spacer, $\phi_{oil} \approx \phi_{SiO_2}$), can be found by calibration performing multiple scans in the neighborhood of a dry contact area, see Figure 3.12. The location of the scan lines should be far enough from the ball surface ($\approx 500[\mu m]$ from contact center) in order to avoid the overlay with interference fringes produced by the oil layer on the ball. A micrometer, mounted on the microscope assembly, controls the location of the scan lines with good accuracy.

Knowing the geometry of the deformed ball, the thickness of the silica layer (h_{sp}), and the refractive index (n_{sp}), the *relative* phase change can be found from (3.21) as $\phi \approx \pi/7$ and the silica phase change, from

$$\phi = \phi_{SiO_2} + \phi_{Cr} \tag{3.23}$$

as $\phi_{SiO_2} \approx 8\pi/7$. Because the optical properties of the oil layer and of the silica spacer layer are close (see Table 3.1) the same value is adopted for ϕ_{oil}. The phase shift on reflection from the chromium layer remains unchanged, i.e. $\phi_{Cr} \approx -\pi$

Figure 3.13 shows the result of a measurement of the spacer layer at the inlet of a dry contact, with the calibrated phase change. The plot also shows the measurement of the gap height at the center of the dry contact. A thickness of about $540[nm]$ is measured at the inlet and in the contact region in accordance with the thickness of the spacer layer. Please note that the relative phase change ϕ is given by (3.23) for the inlet scan line and by (3.22) for the line scanned at the contact center. In the particular measurement shown in Figure 3.13 some discontinuity can be observed around $y = -60[\mu m]$, which is attributed to a possible dust particle or some defect of the silica layer. This type of measurement shows that the method works and can be used to measure thin oil films in the neighborhood of the contact area.

3.2.4 EHL mapping

Instead of measuring the film thickness in a given region of the contact, a complete map of an area of interest can be obtained by a method introduced by Cann et al. [5]. The method makes use of a high resolution CCD color camera that acquires pictures of the contact with a $0.01[ms]$ rate, at a trigger position where prior zero
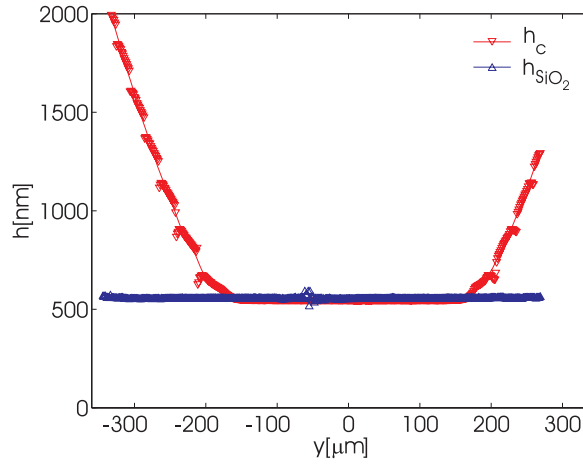
FIGURE 3.13: *Measurement of spacer layer at* $500[\mu m]$ *from the contact center (circles) and of gap height in center of the dry contact (triangles)*

film calibration is carried out. A frame grabber converts the output of the camera (chrominance and luminance) into combinations of red green and blue (RGB), then a specialized program transforms these combinations into hue, saturation and intensity (HSV), which are then used to translate the color of the captured image into values of the film thickness via a calibration file.

The calibration procedure consists of wavelength measurements of the constructive interference, which are related with the corresponding hue values and then converted into film thickness according to

$$h = \frac{\lambda(N - \phi)}{2\,n} \qquad (3.24)$$

Table 3.2 shows combination of red, green and blue with the corresponding wavelength and film thickness obtained for a number of basic colors. For the rest of the spectra different combinations of values between 0 and 1 are found.

Figure 3.14 shows the stages in the mapping for the case of a dry contact between a steel ball loaded with $20[N]$ against the glass disc. In the figure the intermediate RGB values, hue, saturation and intensity are displayed and also the resulting map of the contact. The map can be interpreted as the deformed surface of a ball on a "rigid" flat surface. In Figure 3.15 maps of a contact lubricated with $HVI650$ at a temperature of $80[^\circ C]$ are presented for an entrainment speed u_m of $0.6[m/s]$ are shown for a fully flooded contact and a starved contact. For the starved contact the inlet meniscus can clearly be seen to reach the edge of the Hertzian contact region. As a result a local decrease of the film thickness can be observed.
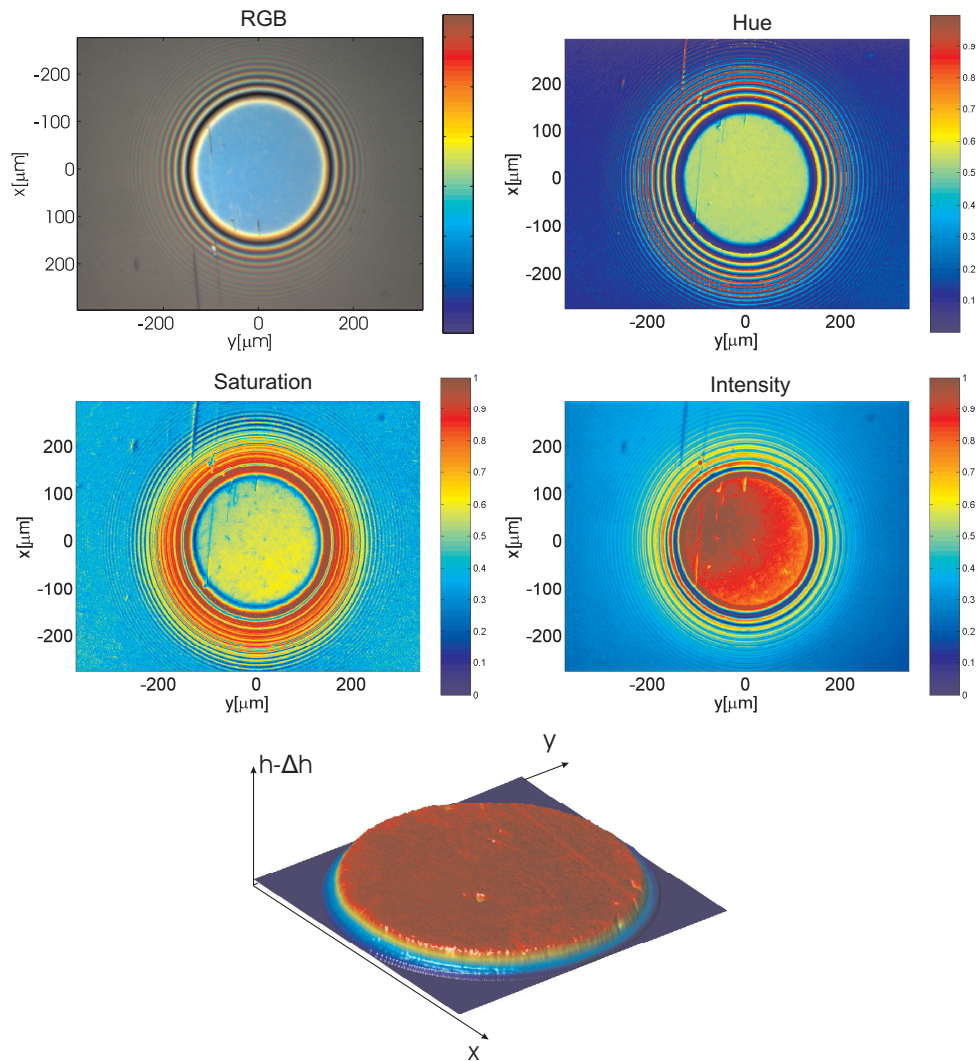
FIGURE 3.14: *Mapping of a dry contact between a steel ball loaded with* $20[N]$ *against a glass disc.*

λ [nm]	Red	Green	Blue	h [nm]			pixel appearance
				$N=1$	$N=2$	$N=3$	
440	0	0	1	149	300	452	■
490	0	1	1	166	335	504	■
510	0	1	0	172	348	524	■
570	1	1	0	193	389	586	■
640	1	0	0	216	437	658	■

TABLE 3.2: *Wavelength of the visible spectra and the RGB combination as a function of film thickness*
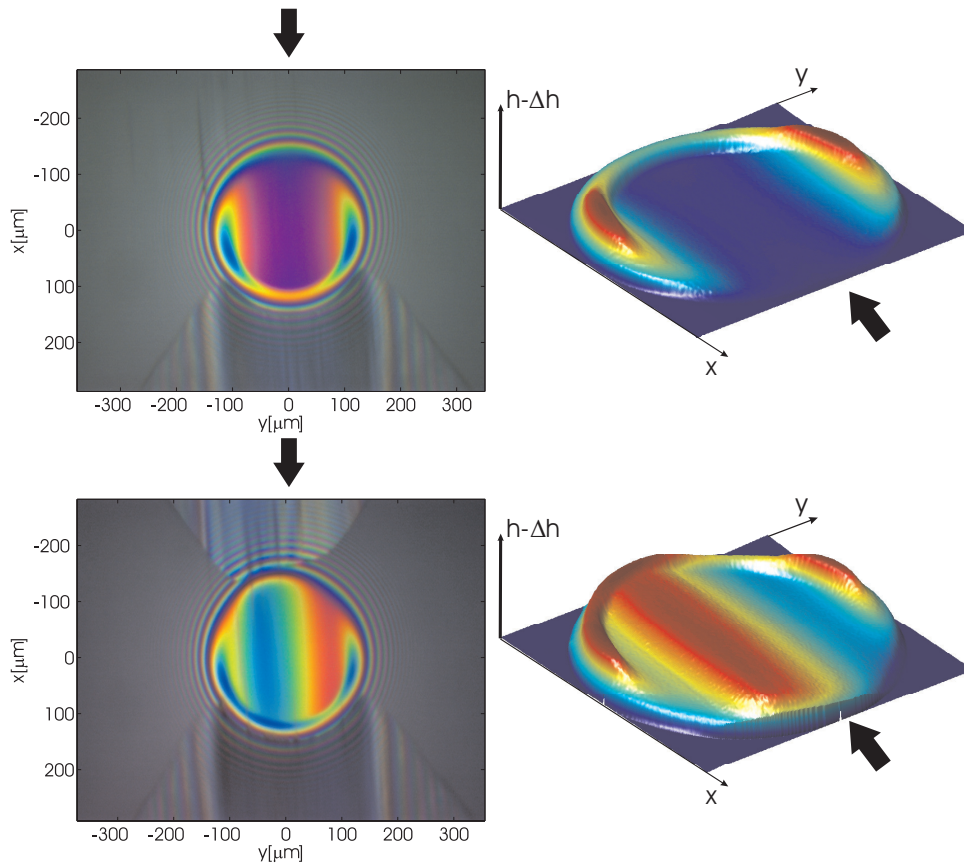
FIGURE 3.15: *Mapping of an EHL contact in fully flooded (top) and starved (bottom) conditions with HVI 650 at 80[°C] with 20[N]. The arrow indicate the direction of the flow.*

STEADY LUBRICATION

In this chapter several aspects regarding the performance of EHL contacts are discussed. For fully flooded conditions the EHL model presented in Chapter 2 is experimentally validated using optical interferometry measurements of the contact between a glass disc and a steel ball. It is shown that for standard mineral oils the model accurately predicts the film thickness, both with respect to its level as well as the local film shape. Next, the potential of tailor-made geometries to form separating oil films is investigated numerically. Subsequently, experimental results for starved EHL contacts are shown, emphasizing the importance of the lubricant distribution. Furthermore, using the EHL model, the effects of limited lubricant supply on the film thickness are studied, in particular, the effect of a spatially varying lubricant supply layer on the film thickness inside the EHL contact. The observed behavior is characterized by dimensionless parameters and captured in simple engineering formulas for practical use. Finally, the thickness and shape of the supplying oil layer is measured using optical interferometry as outlined in Chapter 3.

4.1 Fully flooded conditions

Elasto-hydrodynamic lubrication is very efficient in terms of lubricant usage. Only a limited amount of lubricant is needed to achieve effectively fully flooded lubrication conditions. In this case in the inlet region enough oil is present to enable the maximum film level to be realized given the operating conditions, the geometry of the surfaces and the properties of the lubricant and materials. The state of ample lubricant supply is referred to as fully flooded.

Behaviour of single EHL contacts under fully flooded conditions has been studied extensively and based on numerical results several film thickness prediction formulas have been published, Hamrock-Dowson[31], Chittenden [11], Moes [54], Nijenbanning [57]. In this section, numerical solutions based on the EHL model presented in Chapter 2, experimental results obtained by means of optical interferometry, and prediction of Nijenbanning [57] film thickness formula are compared. For circular

EHL contacts the results are presented for four different oils. Using specially designed rolling elements, wide and a narrow elliptic EHL contacts are investigated experimentally and the measurements compared with results of computations. Subsequently, the effect of the radius ratio on the film thickness is analyzed. Finally, results are presented for the deduced geometries of contact in a Deep Groove Ball Bearing and a Cylindrical Roller Bearing.

4.1.1   Circular EHL contacts

The experimental setup described in Chapter 3 was employed to measure the film thickness inside a single EHL contact as a function of the rolling speed for different oils. Loaded with $20[N]$, a polished steel ball and a flat glass disc share a circular contact area with a radius of $0.134[mm]$ and a maximum Hertzian pressure of $0.5[GPa]$. Fully flooded conditions were ensured by immersing the ball in oil, and pure rolling by allowing the ball to rotate freely on the carriage. The central film thickness was measured as a function of rolling speed for the oils *HVI 650*, *HVI 160s*, *HVI 60*, and *TT 9*. The viscosities at ambient pressure and the pressure-viscosity indices are listed in Appendix C.

The calculations were carried out with input conditions according to the experimental conditions presented above and perfectly smooth surfaces. For high speeds, or for strongly piezoviscous oils (e.g. *HVI 650*) it is important that the computational domain is chosen sufficiently large to allow the pressure to build up in the inlet region. If the inlet boundary is too close, the pressure generation is inhibited by the boundary condition ($P = 0$), resulting in underestimation of the film thickness. The need for a sufficiently large domain is illustrated in Figure 4.1 for *HVI 650*, *HVI 160s* and *TT 9*. It can be seen that for identical operating conditions, the *HVI 650* oil needs a longer inlet region than the *HVI 160s* or *TT 9* oils. For thin oils (e.g. *TT 9* and *HVI 60*) and low speeds the pressure field is limited and smaller domains are sufficient. For these cases a computational domain $x \in [-2.5a; 1.5a]$, $y \in [-2b; 2b]$ with an uniform grid of 257×257 points yields sufficiently accurate results. For a more viscous oils (e.g. *HVI 650* and *HVI 160s*) larger domains and more nodes are used to maintain accuracy. For example, the computations with the viscosity and the viscosity pressure index corresponding to *HVI 650* are carried out using a grid with 513×513 nodes on the domain $x \in [-6.5a; 1.5a]$ and $y \in [-4b; 4b]$.

As a qualitative illustration, Figure 4.2 shows an interferometric image of the contact running at $0.57[m/s]$ with *TT 9* at $25[°C]$ (right) and a contour map of the numerical solution for gap height presented in a similar way (left). As can be seen the qualitative agreement is very good. In both pictures the characteristic horseshoe shape in the film can be seen with the minimum film thickness occurring in the two side lobes and a smaller local constriction in the film thickness just before the exit region where cavitation starts to occur. In the interferometric image the cavitated region can clearly be seen.
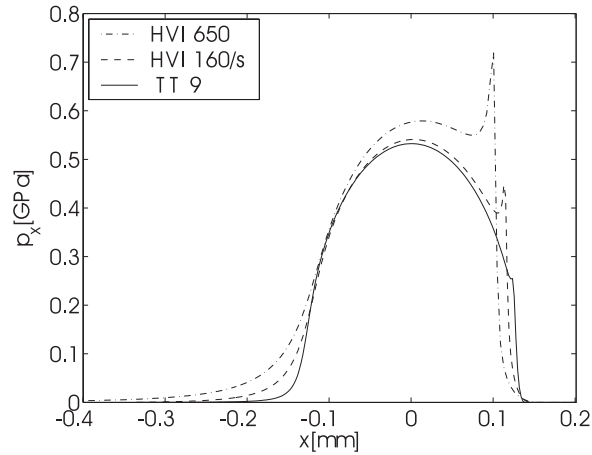
FIGURE 4.1: *Pressure profiles along the running direction for different mineral oils; high viscosity oils require a larger field to build up the pressure*

In Figure 4.3 the film thickness in the center of the contact is plotted as function of rolling speed for the four oils considered at a temperature of $40[°C]$. As expected and shown in many studies before, the central film thickness increases with the rolling speed. In the classical Hamrock and Dowson [30] film thickness prediction formula the central film thickness is proportional to the entrainment speed to the power 0.67. In the range of operating conditions of the ball on disc setup this prediction is very accurate as is confirmed by the results of the numerical computations. A more general prediction formula was developed by Nijenbanning and co-workers [57], see Appendix A. The predictions of this formula are shown as solid black lines in the figure. From the results it is clear that for the case of a standard mineral oil the central film thickness in the contact can be predicted and measured very accurately.

The early film thickness formulae [30] were based on numerical results obtained with a very limited number of nodes. Nowadays, very accurate solutions can be computed, and using the EHL mapping method presented in Chapter 3, precise details of the film shape inside the contact can be revealed. In Figure 4.4 measured film thickness maps are presented for *TT 9* at $25[°C]$ and different speeds. Also shown are centerline profiles of the film thickness in the direction of rolling x and in the cross-stream direction y.

At low speeds the central region of a circular EHL contact tends to be flat and the oil film is very thin. The horse shoe shape is present but restricted to the edge of the contact. This is typical for results in the elastic-isoviscous regime (small L, large M). As the rolling speed increases, the lubrication regime changes from elastic-isoviscous to elastic-piezoviscous (M decreases, L increases). This leads to an increase in the film thickness and at the same time the horse shoe shape becomes more pronounced, i.e. smaller gap heights near the downstream boundary of the contact.
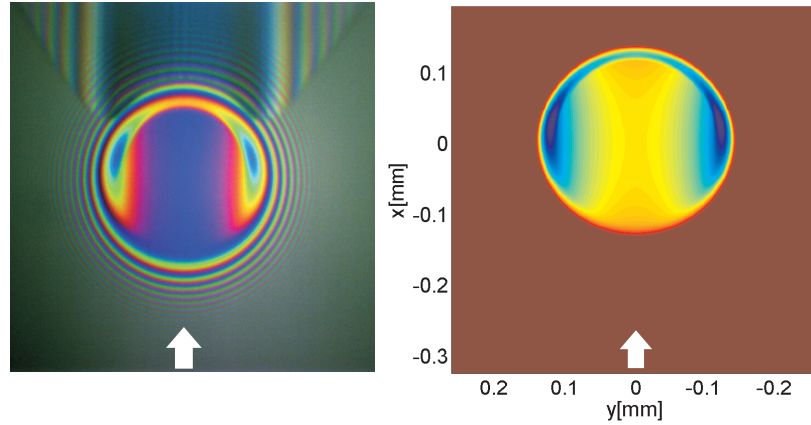
FIGURE 4.2: *Circular EHL contact: interferometric image (left), gap height solution (right) for TT 9 at $25[^{\circ}C]$, $0.57[m/s]$ and $20[N]$. The arrow indicate the direction of flow.*

FIGURE 4.3: *Film thickness as function of rolling speed for different mineral oils at $40[^{\circ}C]$. Note: The faster film thickness decrease at low speeds for the numerical result for $TT9$ and $HVI60$ is a numerical artefact. For these cases a denser grid should be used.*
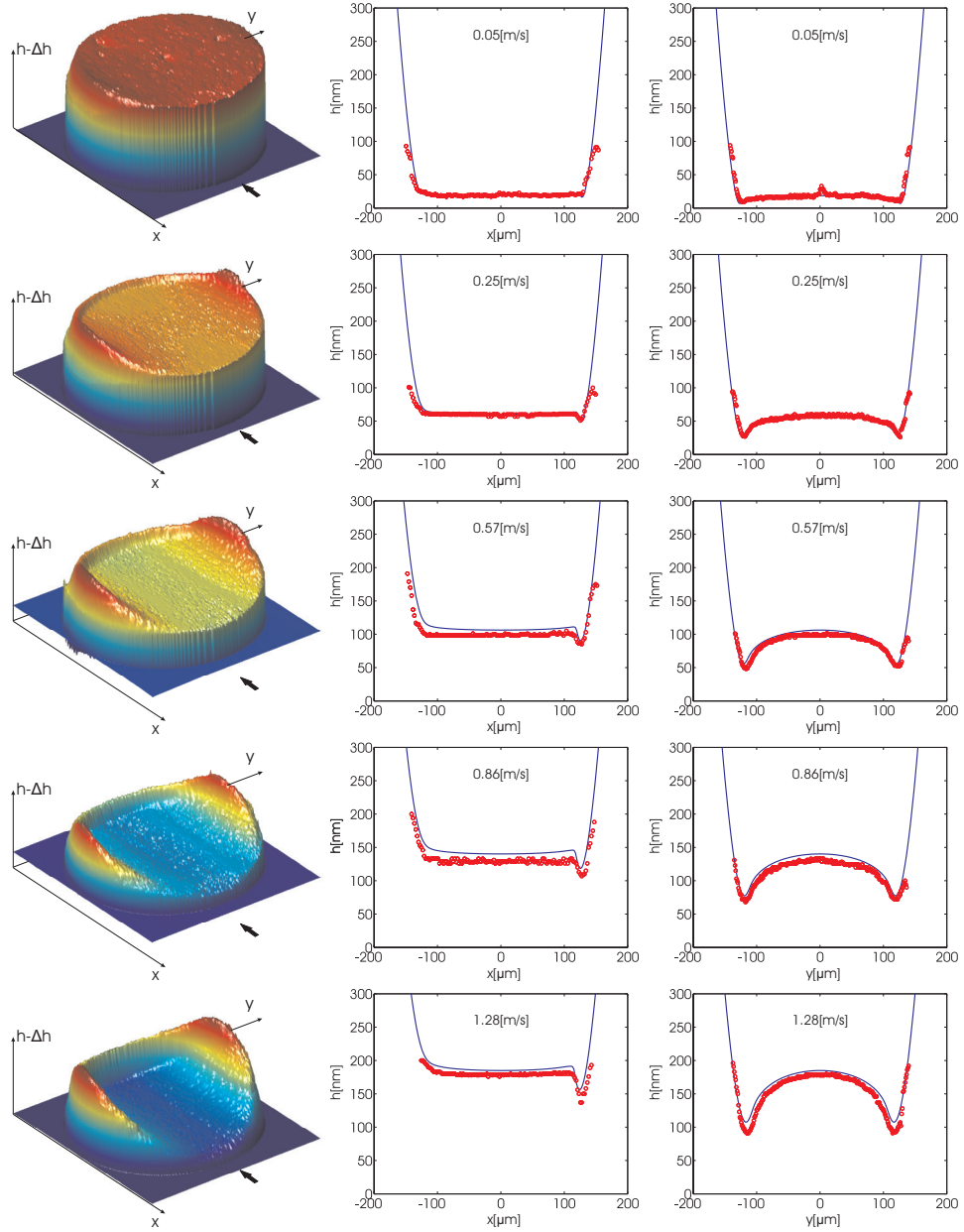
FIGURE 4.4: *EHL contact maps (left column) and film profiles (middle and right column) for TT 9 at* $25[°C]$ *and different rolling speeds; solid line - numerical results, symbols - experimental results.*

In the centerline film thickness profile graphs also the results of numerical calculations are shown as solid lines. As can be seen, both the level of the film thickness as well as the local changes in the horse shoe shape are predicted very accurately.

4.1.2 Wide elliptic EHL contacts

Most of the EHL contacts encountered in practice are elliptic. A prediction formula of the central film thickness for elliptic EHL contacts with the major axis perpendicular to the direction of rolling has been presented by Nijenbanning and coworkers [57]. Their formula was based on a function fit to results of numerical calculations. Compared to circular EHL contacts, in the specific literature only few experimental results are available for elliptic EHL contacts. In this study, experimental results for wide elliptic EHL contacts have been obtained by replacing the ball with a roller. The ratio of curvatures in x and y direction for the used roller is $I\!D = 0.136$. For the steel-glass contact at a load of $10[N]$ the resulting Hertzian contact area is an ellipse with the *major* axis $b = 0.272[mm]$, perpendicular to the running direction and the *minor* axis $a = 0.073[mm]$. The calculated surface pressure in the center of the contact is $p_H = 0.240[GPa]$. To achieve pure rolling conditions the roller rotates freely on a carriage that holds the roller on the track with a spring. Fully flooded conditions are ensured by filling the lubricant reservoir such that the roller is half submerged in oil. The oil used for these experiments is *TT 9* at a temperature of $25[°C]$.

The numerical simulations are run for similar conditions, and considering perfectly smooth surfaces. For wide elliptic EHL contacts it is also important to choose a sufficiently large domain to avoid "numerical starvation". The results presented in this section were obtained using a domain $x \in [-6.5a; 1.5a]$, $y \in [-2b, 2b]$ and a uniform grid with 513×513 points.

An interferometric image of the contact running at $0.8[m/s]$ and a contour plot of the computed film thickness for these conditions is presented in Figure 4.5. The qualitative agreement is obviously quite good. In a wide elliptic contact the horseshoe shape still appears, but often is less pronounced. In many cases the overall minimum film thickness occurs on the central line near the exit. At very high loads it occurs again in the side lobes (as for the case of circular EHL contacts). Under the same operating conditions, the film thickness of wide elliptic contacts is larger than in an equivalent circular contact (same R_x). This is explained by the fact that the wide elliptic contact tends to reduce the oil flow around the contact. In other words the amount of side leakage is smaller in wide elliptic contacts.

In Figure 4.6 the measured central film thickness as a function of the rolling speed is shown. Also shown are the predictions of the numerical simulations and the values predicted by the approximate Nijenbanning formula. As can be seen for low rolling speeds all values are in a close range and obviously the model predicts the film thickness accurately. However, with increasing speed the difference increases and the measured film thickness is smaller than the predicted values. This is most

FIGURE 4.5: *Wide elliptic EHL contact ($\mathbb{D} = 0.136$): interferometric image (left), gap height solution (right) for TT 9 at $25[°C]$ and $0.8[m/s]$. The arrow indicates the direction of the flow.*
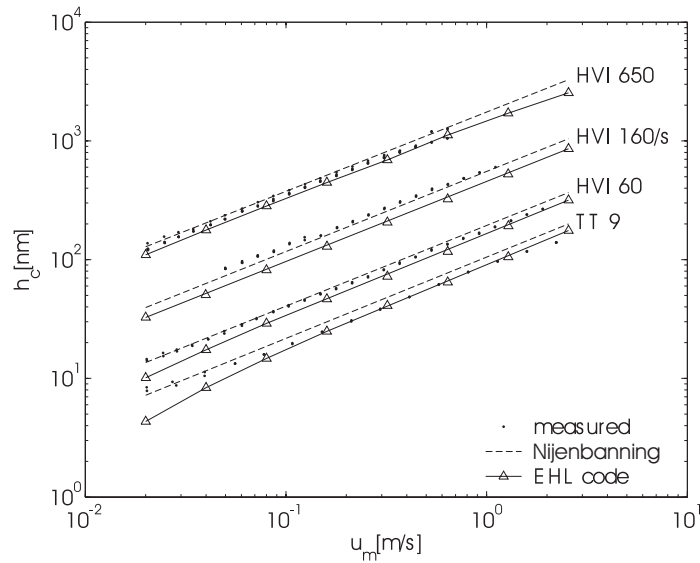

FIGURE 4.6: *Film thickness as function of rolling speed for a wide elliptic contact ($\mathbb{D} = 0.136$) lubricated with TT 9 at $25[°C]$*

likely attributed to the fact that in the experiment the roller at high speeds tends to slip as a result of which the actual entrainment speed, and thereby the film thickness, is lower.

4.1.3 Narrow elliptic EHL contacts

In some machine parts (e.g. worm gears) the contact ellipse is oriented parallel to the rolling direction. From a film generation point of view this is a detrimental situation. For narrow elliptic contacts the lubricant can very easily flow around the contact. In general the film thickness in narrow contacts is therefore significantly smaller than for an equivalent circular contact (same R_x). Also, the difference between the minimum and the central film thickness tends to be much larger as the formation of side lobes is much more pronounced. Narrow elliptic contacts have been extensively studied by
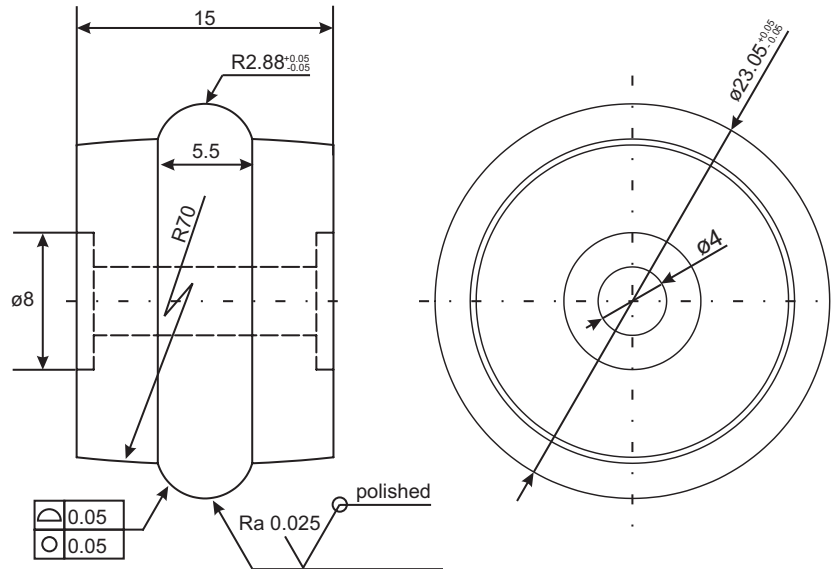
FIGURE 4.7: *Rolling element used for experiments with narrow elliptic EHL contacts*

Evans and coworkers [20], [21]. In the present study an experimental validation for narrow elliptic EHL contacts calculations has been attempted.

To obtain a narrow elliptic contact a special rolling element was designed. To facilitate good validation of the EHL model (which assumes perfectly paraboloid surfaces), the surface of the roller should be sufficiently smooth and hard, with precise radius of curvature and tight tolerances to circularity and surface profile. Finally, the resulting major axis of the contact ellipse should not be too long, otherwise the inflow into the contact is not parallel to the major axis due to the fact that it rolls on a circular track on the disc. Figure 4.7 shows a drawing of the rolling element used in the present measurements. The ratio of the radii of curvature of the roller in x and y direction is $I\!D = 4$.

The hardness that could be achieved within the limits of the local workshop capability for heat treatment was $\approx 350[HV]$. Typically, rollers in standard roller bearings have a hardness of about $800[HV]$. The implications of this difference for the measurement results will be explained below.

During the experiment the rolling element rotates freely on an adapted carriage that holds the rolling element on the running track. An applied load of $10[N]$ creates a contact ellipse with the the minor axis $b = 0.055[mm]$ perpendicular to the rolling direction and major axis $a = 0.139[mm]$. The calculated maximum Hertzian pressure is $0.620[GPa]$. The results are presented for fully flooded conditions with the *TT 9* oil at $25[^{\circ}C]$.

The input values for the computations are identical to the experimental setup presented above. In the computations a number of 257×129 nodes is used on the finest

grid and 33×17 nodes on the coarsest grid. More points along the x line helps to restore the loose (weak) coupling . The under-relaxation factors were 0.3 for Gauss-Seidel part, 0.1 for Jacobi and 0.05 for the force balance relaxation. The size of the integration patches $(m_{1x}, m_{2x}, m_{1y}, m_{2y})$ are proportional to the ellipticity ratio κ, as recommended by Wijnant [83].

In Figure 4.8 an interferometric image of the contact running at $0.57[m/s]$ and a contour plot of the numerical solution for the gap height are shown. As explained above, the oil much more easily flows around the contact hampering the film formation. This reflects in a much larger difference between the central and minimum film thickness which is evident because as the side lobes are much narrower and tend to penetrate deeper into the film. As can be seen from the figure the qualitative agreement between the measured and computed results is quite good. Quantitative film thickness results are presented in Figure 4.6. The plot shows the measured values of the central film thickness as a function of the rolling speed. The values displayed represent the values obtained during several sweeps of increasing and decreasing speed. Also shown are the computed values and the values predicted by Nijenbanning's curve fit formula [57]. Please note that the curve fit formula was derived for ellipses with the major axis perpendicular to the rolling direction (wide elliptic contacts). Even so, this approximation is quite good for moderate values of $I\!\!D$. For oil films above $\approx 50[nm]$ the agreement between the predicted and measured values is very good. At lower film thicknesses the difference between measurements and computations increases. Moreover, the measured values decrease during consecutive speed sweeps. A possible explanation is that the spacer layer is worn during the experiment as a result of the rolling element surface damage. This illustrates the importance of adequate hardness of the highly loaded surfaces in applications like bearings and gears. Nevertheless, it is concluded that also for narrow elliptic EHL contacts good agreement between experimental results and numerical predictions exists.

4.1.4   Effect of ellipticity on the EHL performance

In the previous sections results for three types of EHL contacts were presented. In this section an overview of the EHL performance as a function of the curvature ratio ($I\!\!D = R_x/R_y$) is given. Numerical simulations were performed for a wide range of values of ellipticity keeping the load, speed, viscosity and viscosity-pressure index fixed. In Table 4.1 the computed film thickness is displayed for each case. Measurements for ellipticities corresponding to R_x/R_y ratios of 1 and 0.136 are also available. For reference, the values of Moes's dimensionless parameters M and L, the ellipticity ratio κ and the maximum Hertzian contact pressure p_H for the resulting cases are also shown in the table. For the case of fixed external force the direct effect of increasing the radius of curvature in y-direction is a variation of the ellipticity factor κ. Also the Hertzian contact pressure decreases and thus the contact becomes less loaded per square meter as the contact area increases.
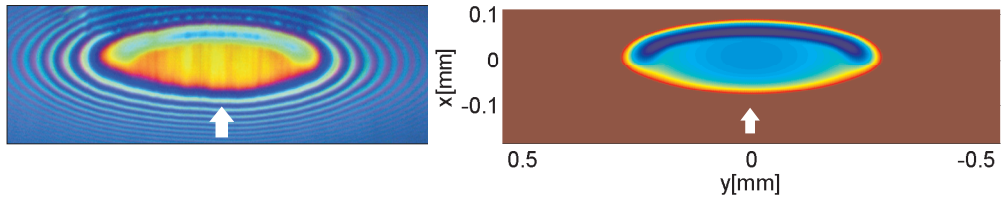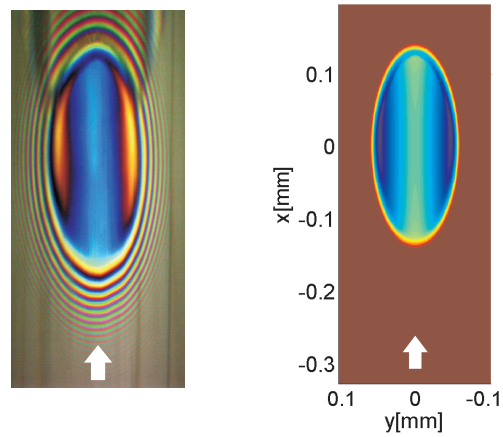
FIGURE 4.8: *Narrow elliptic EHL contact ($I\!D = 4$): interferometric image (left), gap height solution (right) for TT 9 at $25[°C]$ and $0.6[m/s]$. The arrow indicates the direction of the flow.*

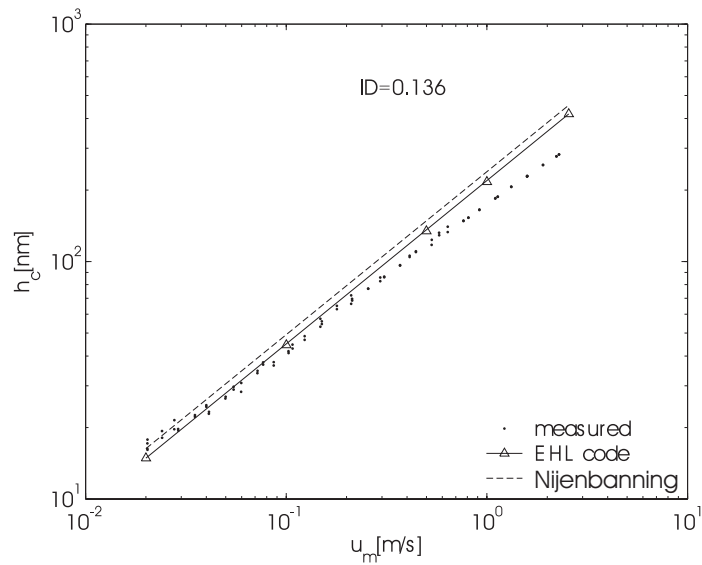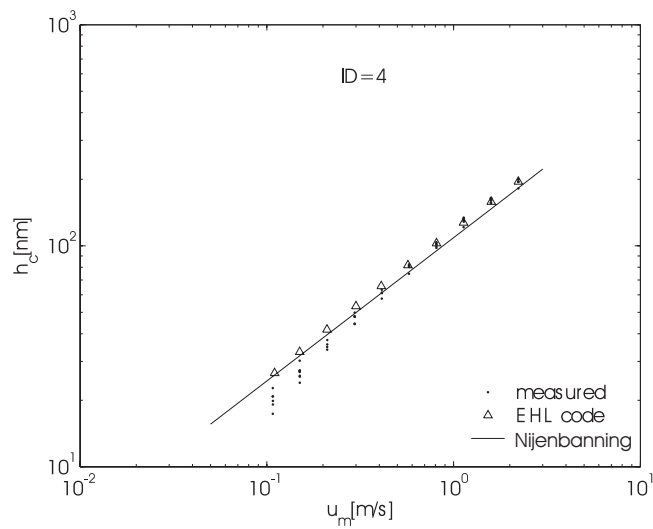FIGURE 4.9: *Film thickness as function of rolling speed for a narrow elliptic contact ($I\!D = 4$) lubricated with TT 9 at $25[°C]$*

The numerical results are graphically illustrated in Figure 4.10. For $I\!D \leq 1$ (wide elliptic contcts) an increasing film thickness can be observed. At extremely low values of $I\!D$, relatively small changes of the film thickness in comparison to the increment of R_y are observed. On the other side of the range ($I\!D > 1$, narrow elliptic contact), the variation of the film thickness with $I\!D$ is much stronger.

An illustration of the effect of the radius of curvature on the local film shape inside the contact is presented in Figure 4.11. This figure shows representative profile plots of the numerical solutions for pressure and gap height at the centerline of the contact in the direction of the flow ($y = 0$) and across the contact ($x = 0$). The pressure and film profiles clearly show how, with decreasing $I\!D$ (wider contacts), the solution approaches the rigid isoviscous regime of very little deformation and small pressure. On the other side, with increasing $I\!D$ (narrower contacts), as a result of the increasing side leakage the solution shows more extreme local film effects, i.e. the side lobes are much deeper, and the ratio central to minimum film thickness is much larger. Also, the pressure in the lubricant film inside the contact is closer to the Hertzian pressure profile.

The results presented in this section illustrate how wider elliptic EHL contacts enhance the film formation capacity and generate a more favorable pressure distribution. For ideal lubrication conditions wide elliptic contacts are more likely to work well because they tend to force the lubricant through the contact, rather then permitting side leakage and flow around the contact. Based on these findings, it is recommended to avoid narrow elliptic EHL contacts, as the probability of film collapse and metal to metal contact is much higher than in the case that the same contact ellipse is rotated $90[°]$. If, for the sake of functionality (e.g. worm gears), that is not possible, appropriate lubricants, materials and surface treatment should be selected.

With wide elliptic EHL contacts special care should be taken with lubrication. These contacts need large (spatially extensive) pressure fields in order to build up their separating film and therefore are more likely to work under starved lubrication conditions, especially for high speed applications. In bearings for example, an appropriate distance between the rolling elements should be assured. Otherwise, the load capacity gained by increasing the number of rolling elements increases the probability of metal-to-metal contact and implicitly reduces the life of the bearing.
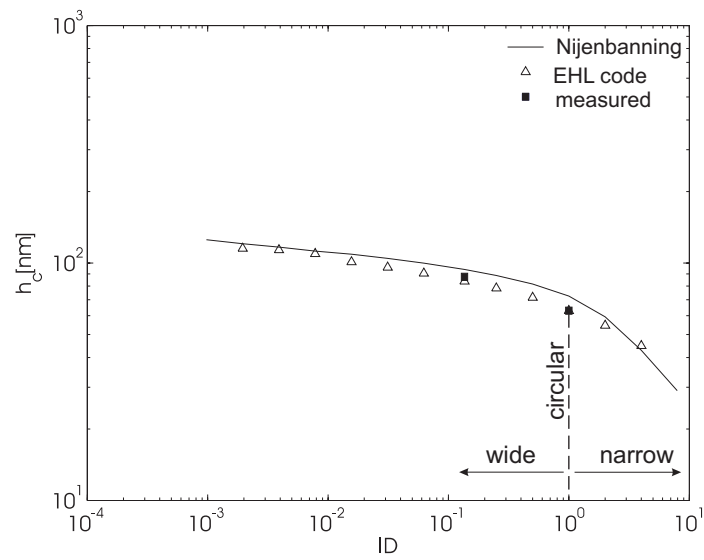
FIGURE 4.10: *Central film thickness for different ellipticity factors for TT9 at* $40°C$

type of contact	F [N]	u_m [m/s]	R_x [mm]	R_y [mm]	$ID = R_x/R_y$	κ	p_H [GPa]	M	L	h_c approx. [nm]	h_c EHL [nm]	h_c measured
							TT 9 @ 40[°C]					
← narrow	18	0.57	9.525	2.38	4	0.4	0.857	683.75		42.9	44.79	–
	18	0.57	9.525	4.76	2	0.633	0.654	483.49		59.3	54.54	–
circular	18	0.57	9.525	9.525	1	1	0.512	341.79		72.6	62.91	63.0
wide →	18	0.57	9.525	19.05	0.5	0.633	0.412	241.69		81.60	71.53	–
	18	0.57	9.525	38.10	0.25	0.4	0.34	170.89		88.60	78.34	–
	18	0.57	9.525	70.00	0.136	0.27	0.292	126.08	4.35	94.00	83.70	87.47
	18	0.57	9.525	152.4	0.063	0.165	0.243	85.45		99.90	90.41	–
	18	0.57	9.525	304.8	0.031	0.108	0.209	60.42		104.60	95.83	–
	18	0.57	9.525	609.6	0.016	0.071	0.181	42.72		108.90	101.02	–
	18	0.57	9.525	1219	0.008	0.047	0.158	30.21		112.28	109.30	–
	18	0.57	9.525	2438	0.004	0.032	0.138	21.36		116.60	113.53	–
	18	0.57	9.525	4877	0.002	0.021	0.121	15.10		120.60	115.09	–

TABLE 4.1: *Central film thickness for different values of $ID = R_x/R_y$ ratio*

4.1.5 Implementation of tailor-made geometries

Following the development of a general purpose solver for EHL contacts with varying geometry (as in bearing applications) the attention is now directed to two typical examples of radial bearings: a Deep Groove Ball Bearing ($DGBB$) and a Cylindrical Roller Bearing (CRB), see Figure 4.12. The results obtained for $DGBB$ are compared with existing film thickness approximations. For the CRB geometry a logarithmic profile was implemented for the roller and a cylindrical-straight profile for the outer raceway.

In order to account for the geometry of a specific application (bearing, gear, knee joints, etc.) the main modification to the EHL model (see Chapter 2 and 3) is the gap height equation (2.4). The initial (undeformed) gap between the surfaces in contact $z(x, y)$ is described by two functions $z_1(x, y)$ and $z_2(x, y)$ containing the characteristics of the two surfaces:

$$z(x, y) = z_1(x, y) + z_2(x, y) \qquad (4.1)$$

The functions $z_1(x, y)$ and $z_2(x, y)$ can be defined using data imported from real applications or described by functions describing the macro-geometry. Below, two examples of how the geometry of a specific bearing can be used in an EHL analysis are given.

One of the characteristics used to judge bearing performance regards the load transfer from one ring to the other via its rolling elements. The load distribution is determined on each ball or roller and the performance of the heaviest loaded EHL contact is evaluated. In the present study thrust load and dynamic effects are neglected, which implies low rotational speeds and purely radial loads. Moreover, the rolling motion in a bearing is accompanied by a degree of sliding and skew. The spinning motion can be important when the contact angle is nonzero. In order to avoid further complex phenomena occurring in sliding and with skew in this study these effects are neglected. Their importance is acknowledged and is recommended as future research. The main point here is to investigate the basic aspects of EHL for the case of specific geometry configurations.

When the bearing is functioning, the rolling elements orbit around the bearing axis and simultaneously revolve about their own axis. These rotational speeds translate to surface velocities u_m relative to the inner or outer raceway. For the bearings studied here inner ring rotations are considered, with a stationary outer ring. For rotational speeds of the inner ring between 100 and 1500 [rpm] the corresponding surface velocities u_m are presented in Table 4.2 and 4.3. For details regarding the way in which the operating conditions from a bearing are translated to individual EHL contacts see [32].

The lubrication conditions are assumed to be ideal. According to [32], for low rotational speeds and a pitch diameter of 100 [mm] the minimum required lubricant
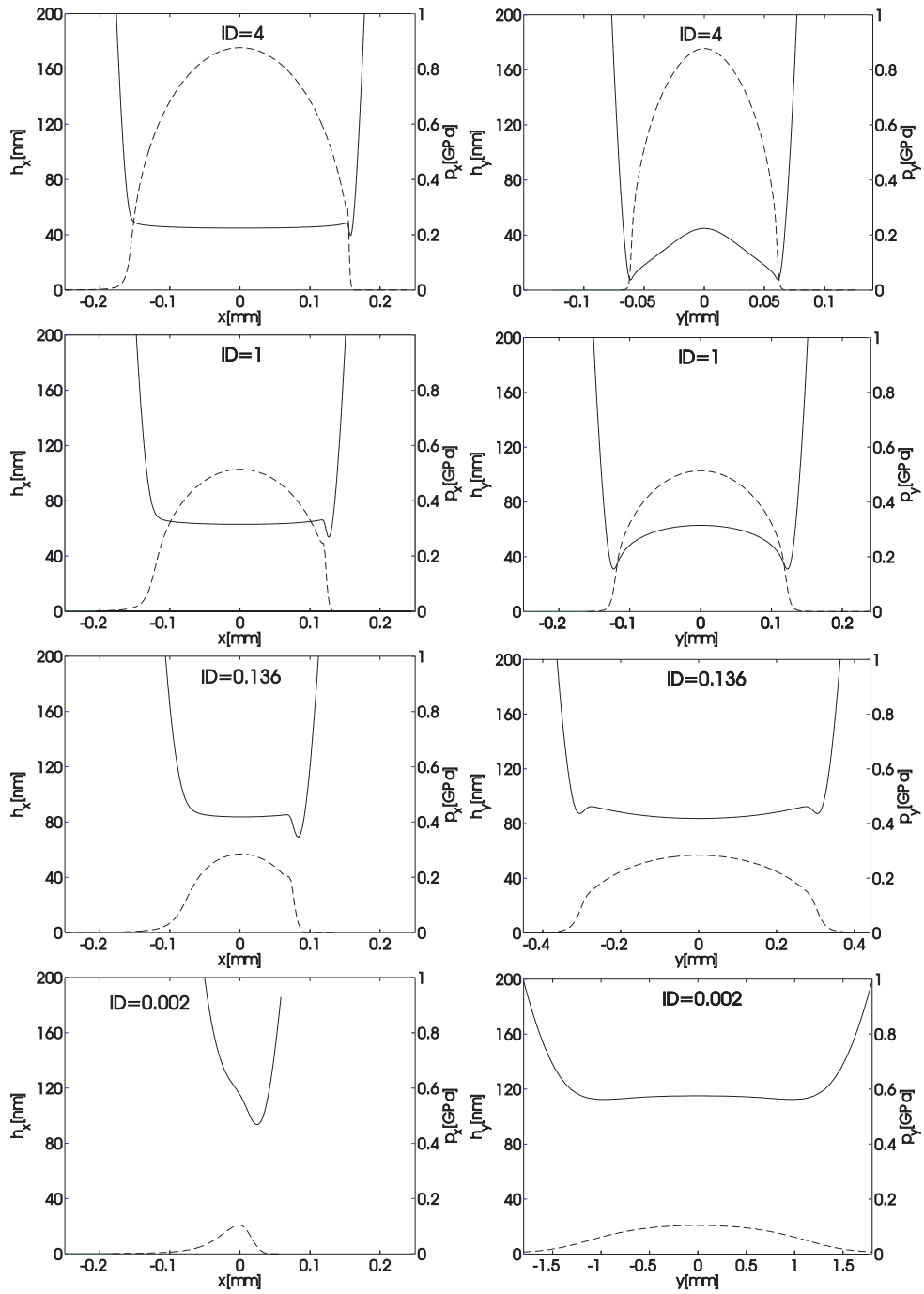
FIGURE 4.11: *Gap height (solid line) and pressure profiles (dashed line) along and across the rolling direction for different ellipticity factors*
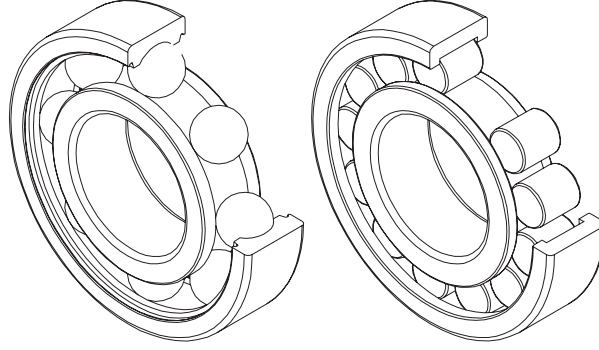
FIGURE 4.12: *Single row $DGBB$ (right), and CRB (left)*

viscosity is about 8 [cSt]. At an operating temperature of $40[°C]$, *TT 9* seems to be an acceptable choice. A further motivation for this choice is that this oil is a well known Newtonian fluid, intensively used for the experiments in previous research.

Deep Groove Ball Bearings($DGBB$)

Single row deep groove ball bearings are used in a wide variety of applications. They are simple in design, non-separable and robust in operation. The geometry of Deep Groove Ball Bearings and the close conformity between raceway grooves and balls, enable these bearings to accommodate axial loads in addition to radial loads and function for a long time with little or no maintenance. On the other hand the close conformity makes the analytical solution for the dry and lubricated contact to be inexact (see the non-conformity assumption).

Figure D.1 and Table 4.2 shows the principal dimensions for the single row deep groove ball bearing 6312 as deduced from [89] and [32], which will be used in this study.

In this study, outer raceway contact area is considered (see Table 4.1). The geometry of the ball, $z_1(x, y)$, is described by a hemisphere of radius $D/2$, see Figure 4.13. The outer raceway geometry, $z_2(x, y)$, is a semi-ellipsoid with the semi-major axis $d_o/2$ and the semi-minor axis r_o for the region within the groove region and a cylinder of radius $d_o/2 - \Delta z$ on the sides of the groove. Both surfaces are considered perfectly smooth. The resulting expressions for z_1 and z_2 are given by (4.2) and (4.3).

$$z_1(x, y) = \frac{D}{2} - \frac{D}{2}\sqrt{1 - \left(\frac{x}{D/2}\right)^2 - \left(\frac{y}{D/2}\right)^2} \tag{4.2}$$

$$z_2(x, y) = \begin{cases} \frac{d_o}{2} - \frac{d_o}{2}\sqrt{1 - \left(\frac{x}{d_o/2}\right)^2 - \frac{y^2}{d_o r_o/2}} & if \ -\frac{l_g}{2} \leq y \leq \frac{l_g}{2} \\ \frac{d_o}{2} - \frac{d_o}{2}\sqrt{1 - \left(\frac{x}{d_o/2}\right)^2 - \frac{(l_g/2)^2}{d_o r_o/2}} & otherwise \end{cases} \tag{4.3}$$
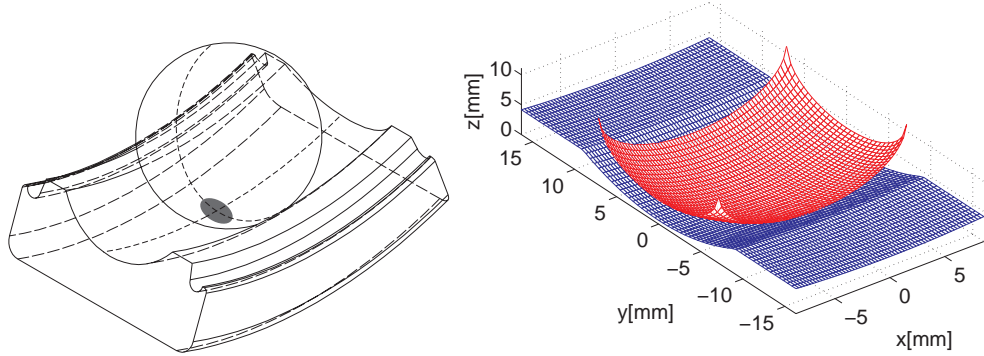
FIGURE 4.13: *Ball-outer raceway contact of single row deep groove ball bearing*

At a radial load of $400[N]$ on the bearing, the calculated maximum load on the ball is about $220[N]$, see Table 4.1. The dry contact parameters such as contact pressure (p_{Ho}), semi-axes of the contact ellipse (a_o and b_o) and mutual approach (c_o) can be calculated with Hertz's formulae. For the operating conditions from Table 4.1, the Moes dimensionless parameters M and L can be calculated and the central film thickness approximation h_{cN} is found with the formulae from Appendix A.

The EHL computations were done on a computational domain $x \in [-6.5a_o; 1.5a_o]$, $y \in [-4b_o; \le 4b_o]$ with 513×513 points. A relatively large inlet region is preferred to avoid "numerical starvation".

An illustration of numerical results is given in Figure 4.14, where the pressure and gap height distribution for a rotational speed $n_i = 1500[rpm]$ are shown. In the bottom row of Figure 4.14, profiles of the considered surfaces are shown. On the left hand side, the surfaces in contact are shown along (xOz) axis; the dashed lines lines represent the surfaces tangent while the solid lines depict profiles of the loaded surfaces in relative motion.The elastic deformation is equally distributed to both surfaces. Note that the mutual approach δ_0 is attributed exclusively to the surface z_1. The narrowing region towards the outlet region can be recognized on this plot. The gap height can also be distinguished on the profile yOz (bottom right).

Numerical results for other test cases are presented in Table 4.2 and Figure 4.15. When the computed film thickness (h_{cDGBB}) is compared with the Nijenbanning's film thickness approximation (h_{cN}) a difference of about 20% can be noticed. A very small disagreement exists with the calculated central film thickness (h_c) obtained with the gap height as given by (2.4) and (2.7).

In Figure 4.15 the difference between the film thickness approximation and the full numerical calculations are visualized. The plot shows the central and the minimum film thickness as a function of mean velocity u_m plotted in a logarithmic scale. The overall observation of these results is that, the analytical approximation overestimates the central film thickness of a ball bearing with a close conformity.
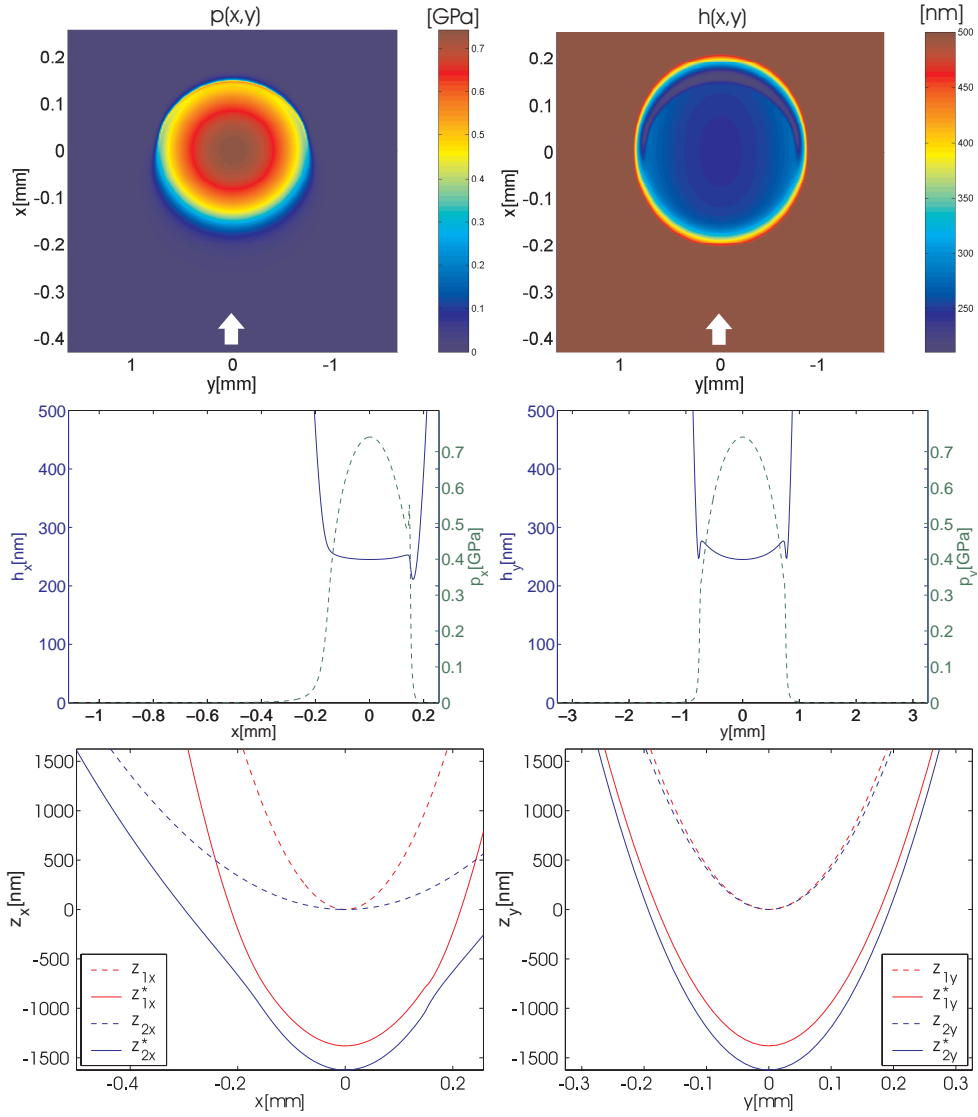
FIGURE 4.14: *Pressure distribution, gap height and surface deformation of the heaviest loaded EHL contact from a DGBB 6312 loaded with 400[N] at $n_i = 1500[rpm]$.*

n_i	u_m	M	L	h_{cN}	h_c	h_{cDGBB}
$[rpm]$	$[m/s]$				$[nm]$	
100	0.191	1536.76	5.01	41	32.87	32.87
200	0.381	915.56	5.95	67.1	54.78	54.73
300	0.572	675.05	6.59	89.7	73.67	73.62
400	0.762	544.39	7.08	110.1	90.7	90.63
500	0.953	460.32	7.48	129.2	105.84	106.52
600	1.143	401.65	7.83	147.1	120.48	121.42
700	1.334	357.7	8.14	164.3	134.46	135.68
800	1.524	323.7	8.42	180.6	147.75	149.29
900	1.715	296.26	8.67	196.5	160.6	162.47
1000	1.905	273.81	8.9	211.7	172.93	175.16
1100	2.096	254.88	9.12	226.6	184.93	187.55
1200	2.287	238.74	9.31	241.1	196.58	200
1300	2.477	224.87	9.5	255.2	207.85	211.32
1400	2.668	212.69	9.68	269	218.9	222.82
1500	2.858	202	9.86	282.4	229.63	234.02

TABLE 4.2: *Central film thickness, rolling speed and values of the dimensionless numbers characterizing 'Moes' operating conditions of an individual EHL contact as function of the rpm of a $DGBB$ 6312 loaded with $400[N]$*
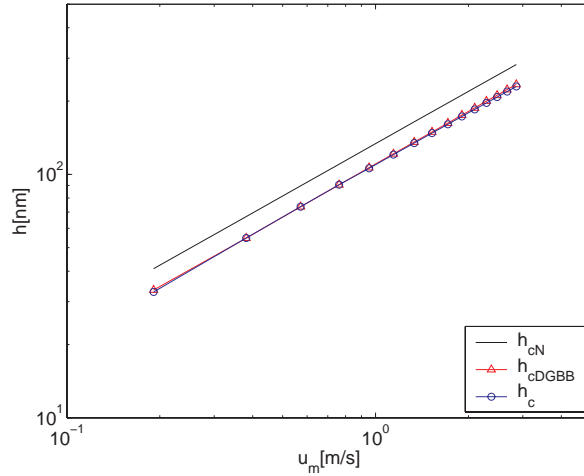
FIGURE 4.15: *Central and minimum film thickness of the heaviest loaded EHL contact from a DGBB 6312 loaded with $400[N]$ as function of rolling speed*
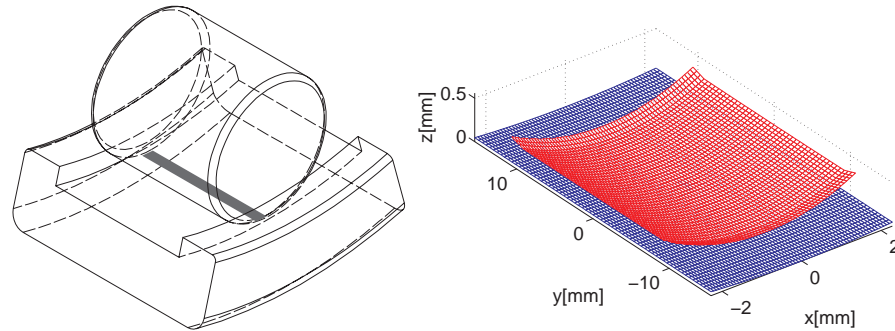
FIGURE 4.16: *Roller outer raceway contact of single row CRB*

Cylindrical Roller Bearings (CRB)

Cylindrical Roller Bearings are designed to accommodate high loads through the relatively large contact areas they form between rollers and raceways, see [89]. Although the rolling elements are called "cylindrical", they are not exactly cylinders. True cylinders would produce stress concentrations at the ends of the roller-race contact producing wear and subsurface cracks. Instead, rollers are usually crowned or end-relieved. Early laboratory tests showed that changes of a few micrometers to the roller profile have a positive effect on bearing life. Lundberg [50], [51] showed that a logarithmic contact profile between roller and raceways significantly reduces the risk of edge stresses and provides optimal load distribution.

An analytic prediction of the EHL performance of cylindrical roller bearings with different roller profiles is not available at the moment. A numerical approach is needed to calculate the film thickness and pressure distribution required in models for the prediction of bearing life. In the present study, the geometry of the bering $NJ312ECP$ is investigated. The principal dimensions are given in Table 4.4 and Figure D.2. These dimensions are deduced from [89] and [32].

The profile of the roller used as input, $z_1(x, y)$, is given by (4.4). Although, in reality the raceway of $NJ312ECP$ bearing has "open flanges" (see Figure D.2), here the raceway is considered cylindrical according to (4.5). The need of this simplification comes from the assumption regarding the small height compared with the length and width of the contact area. Both surfaces are assumed perfectly smooth.

$$z_1(x,y) = \begin{cases} \frac{D}{2} - \frac{D}{2}\sqrt{1 - \left(\frac{x}{D/2}\right)^2} - ln(1 - \frac{y}{l_s}) & if \ -\frac{l_s}{2} \leq y \leq \frac{l_s}{2} \\ \frac{D}{2} - \frac{D}{2}\sqrt{1 - \left(\frac{x}{D/2}\right)^2} - \frac{y^2}{DR_r/2} \\ -\frac{D}{2} - \frac{D}{2}\sqrt{1 - \left(\frac{x}{D/2}\right)^2} - \frac{(l_s/2)^2}{DR_r/2} \\ +\frac{D}{2} - \frac{D}{2}\sqrt{1 - \left(\frac{x}{D/2}\right)^2} - ln(1 - \frac{(l_s/2)}{l_s}) & otherwise \end{cases}$$

$$\text{(4.4)}$$

$$z_2(x,y) = \frac{d_o}{2} - \frac{d_o}{2}\sqrt{1 - \left(\frac{x}{d_o/2}\right)^2} \qquad \text{(4.5)}$$

The length of the contact "rectangle" a_o and the width b_o are calculated with :

$$a_o = \frac{l_s}{2} \qquad \text{(4.6)}$$

and

$$b_o = \frac{8 F_N D}{2\pi E' l_s} \qquad \text{(4.7)}$$

As a first approximation for the pressure distribution the following expression is used:

$$p(x,y) = \begin{cases} p_{Ho}\sqrt{1 - \left(\frac{x}{a_o}\right)^2} & if \ \left(\frac{x}{a_o}\right)^2 \geq 1 \ \& \ -\frac{l_s}{2} \leq y \leq \frac{l_s}{2} \\ 0 & otherwise \end{cases} \qquad \text{(4.8)}$$

Due to the low radius ratio a large pressure field is expected in the inlet region. In order to avoid artificial pressure decay in the inlet boundary x_a is set at $-6.5a_o$; the outlet boundary is $x_b = 1.5a_o$ and the side boundaries y_a and y_b are set at the edge of the outer ring at $-l_o/2$ and $l_o/2$, respectively. As the geometry of the roller profile in y direction changes rapidly near the roller end, more points are needed in this direction. The domain used for these computations is 129×1025. The motivation of choosing such a small mesh size in y direction is the need of an accurate description in gap height near and beyond the roller end. The geometry is changing rapidly once $y < -l_s/2$ and $y > l_s/2$. This can cause large fluctuations in the solution at the neighboring points. As a result, large errors can occur in the restriction and interpolation process from one grid to the other, making the numerical process unstable. Beside that, more points in y direction helps to restore the loss of coupling

in this direction. Choosing small ratios h_y/h_x is a simple, effective (and efficient) trick to avoid singularities at the roller ends and numerical instabilities. The drawback of small ratios h_y/h_x is that it is not optimal for transient problems due to the larger truncation errors, see [83]. Among the alternatives of solving this problem more efficiently, non-uniform grids and adaptive correction patches can be considered. The non-uniform grids should have the focal line at the roller edge and the multi-integration scheme should be also modified. The other option implies correction patches, similar to those used in the multi-integration scheme, applied in the nodes were the pressure increases uncontrolled and also to the neighboring nodes.

In Figure 4.17 the solution for a roller with a logarithmic profile (4.4) and a cylindrical raceway, given by (4.5) is shown.

In the contact center, the film thickness and the pressure profile is similar to a line contact solution, see Venner [70], but with a slightly smaller absolute value than the corresponding value for an infinitely long contact. In Figure 4.17 in the pressure map (top left), two pressure spikes are observed near the edge of the roller. A significant narrowing of the gap height can be also be noticed in the neighbourhood of the pressure spike. The magnitude of the pressure peaks in these regions can reach about two times the pressure in the contact center.

If for a dry contact a logarithmic profile of the rollers is an adequate way to reduce the edge stress, for the lubricated contact this measure turns out to be insufficient. In reality the rollers of CRB units are guided between "open flanges" on the rings, that combined with the specially designed and surface-treated roller ends, reduce the side leakage and the high hydrostatic pressures at the edge of the contact.

In Table 4.3 the computed values of central and minimum film thickness are displayed for different rolling speeds. Figure 4.18 shows a plot of these values as a function of the relative mean velocity u_m in a logarithmic scale. For this particular surface configuration ("CRB") the minimum film thickness shows a dramatic drop as the rolling speed decreases, indicating significant side leakage effects.

Conclusion on implementation of tailor-made geometries

Implementation of geometries from specific bearing applications was attempted by adapting the gap height equation for the input of specific surfaces. The geometries of two bearings were deduced from literature and used as input.

For the geometry of the $DGBB$ the available analytical approximations and the numerical results showed important differences. Large computational domains were assured at the inlet to avoid "numerical starvation", and the results for different mesh sizes were compared. It is concluded that the equations are solved accurate enough and the eventual differences originate from the inaccuracy of either model. The good agreement found for geometries with lower conformity (ball on flat surface) points to the analytical approximation.
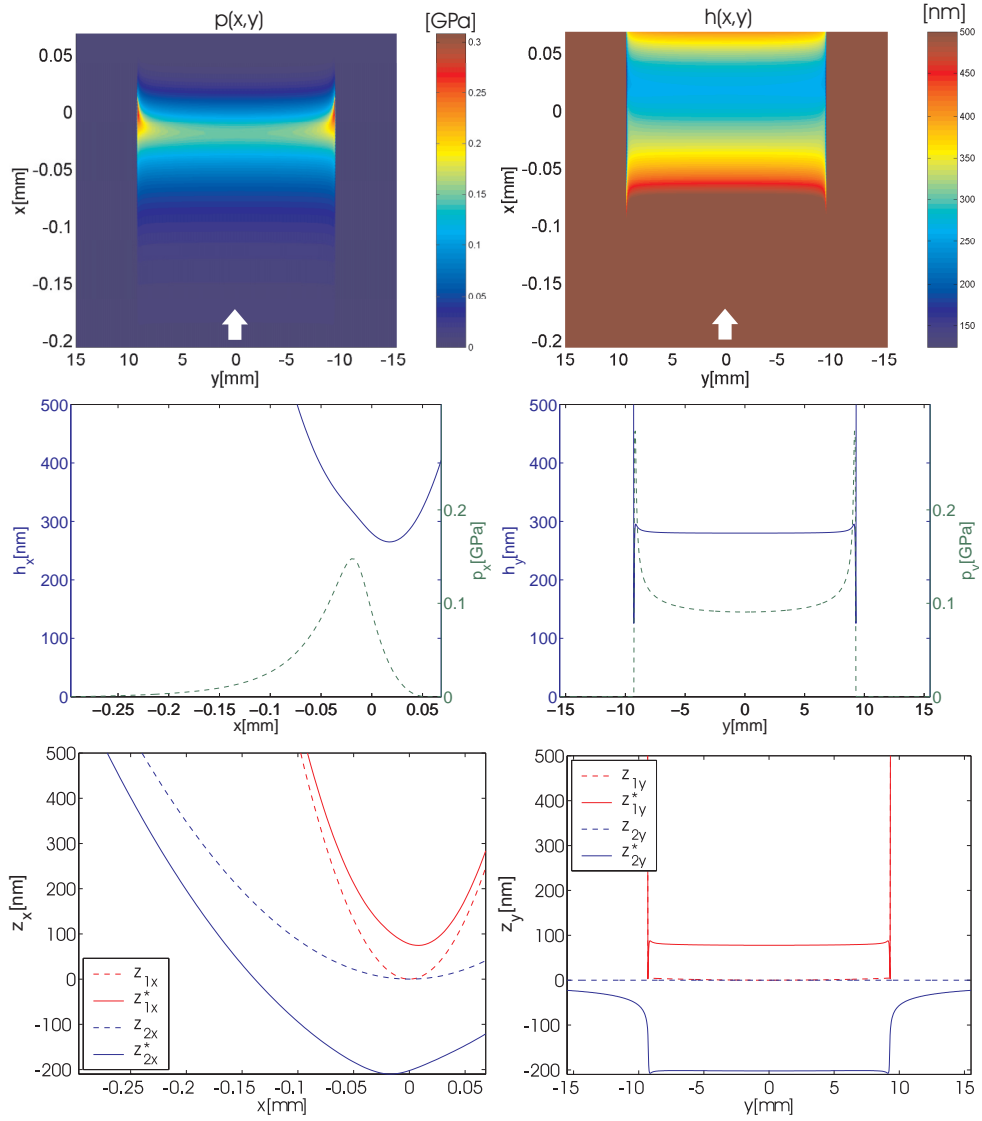
FIGURE 4.17: *Pressure distribution, gap height and surface deformation of the heaviest loaded EHL contact from a CRB NJ312ECP loaded with* $700[N]$ *at* $n_i = 1500[rpm]$

n_i	u_m	h_c	h_{min}	p_c	p_{max}
$[rpm]$	$[m/s]$	$[nm]$		$[GPa]$	
400	0.806	131.42	0	0.2	0.4
500	1.008	151.83	5	0.2	0.3
600	1.21	167.35	15	0.2	0.3
700	1.411	183.83	28.05	0.2	0.3
800	1.613	197.25	42.13	0.2	0.3
900	1.814	210.01	55.24	0.2	0.3
1000	2.016	222.39	67.95	0.1	0.3
1100	2.217	234.36	79.98	0.1	0.3
1200	2.419	245	91.7	0.1	0.3
1300	2.621	257.63	103.04	0.1	0.3
1400	2.822	268.85	114.05	0.1	0.3
1500	3.024	279.93	124.92	0.1	0.3

TABLE 4.3: *Central film thickness, rolling speed and values of the dimensionless numbers characterizing 'Moes' operating conditions of an individual EHL contact as function of the rpm of a $CRB\ NJ312ECP$ loaded with $700[N]$*

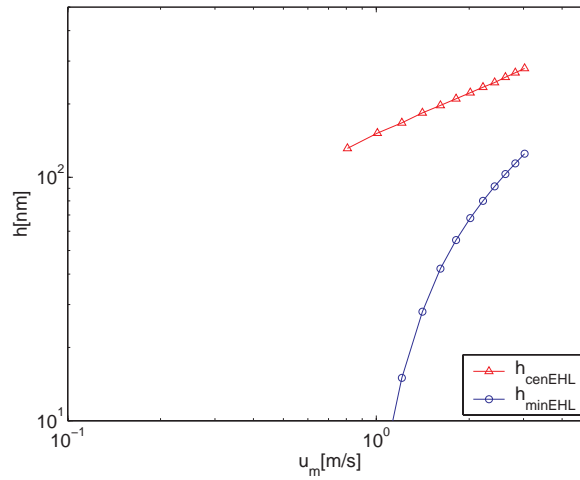FIGURE 4.18: *Central and minimum film thickness of the heaviest loaded EHL contact from a $CRB\ NJ312ECP$ loaded with $700[N]$ as function of rolling speed*

For the CRB geometry the "open flanges" could not be implemented because of the limitations of the present EHL model to small heights. For the case of a roller with a logarithmic contact profile loaded on a cylindrical surface a dramatic drop of the minimum film thickness was recorded. In the absence of "open flanges", this effect is attributed to important leakages taking place on the side of the rollers.

For the "CRB" geometry large pressure fields were observed in front of the contact. This agrees with results presented in the previous section and [57], which showed that the EHL regime moves towards elastic-piezoviscous conditions as the shape factor $I\!D$ decreases. From lubrication point of view, this means an increased probability of starvation.

Higher loads and complex geometries make the numerical process increasingly difficult. The convergence is not always ideal for such circumstances. Further research is needed to make this approach reliable.

4.2 Starved lubrication in steady state conditions

So far, ideal lubrication conditions were assumed. In practical situations there are a number of factors that influence the lubricant distribution at the inlet: local geometry, cage effects (in a bearing), viscosity, rolling speed, centrifugal forces, etc. The amount of lubricant supplied at the inlet is not always sufficient to accomplish ideal lubrication conditions. In such circumstances the performance of an EHL contact is also affected by the amount and the distribution of lubricant carried by surfaces. One of the important motivations for studying starved lubrication is that it represents particular aspects of the phenomena that appear in grease lubricated bearings, which account for the majority of rolling bearings used in the world. It is assumed that during operation the grease is pushed to the side of the running track. As a result, the individual roller-raceway contacts are lubricated by a thin layer of base oil, bleeding on the track from the side embankments [6], [7]. The resulting lubricant layer and its replenishment depend on the type of grease, the properties of the base oil, the contact geometry, the degree to which the grease has been worked, and many other factors. Therefore, film thickness and life prediction of grease lubricated contacts is extremely difficult and many aspects are not fully understood yet.

Using the starved lubrication model as described in Chapter 2 and optical interferometry measurements, the basic effects of starvation are illustrated bellow. Some experimental results of the starved lubrication are shown. Subsequently, results obtained with the theoretical model for the case of a constant lubricant layer are reminded. Finally, a general model of lubricant starvation is presented. The model can be used to predict the effect of a varying lubricant supply across the width of the contact on the gap height inside the contact.

4.2.1   Experimental investigation of starved lubrication

The first step towards the understanding of starved lubrication is the study of a limited lubricant supply to a single contact under controlled conditions. The optical interferometry technique is very well suited for this purpose. At any time the image of the contact provides not only the gap height but also crucial information regarding the location of the inlet meniscus.

A typical result of a central film thickness measurement as a function of speed for a starved and for a fully flooded contact is presented below. The results were obtained for an applied load of $20[N]$ which gives a calculated radius of the Hertzian contact area of $0.134[mm]$ and a maximum contact pressure of $0.5[GPa]$. For the experiments with starved lubrication, instead of having the ball immersed in oil, only a very small amount of oil was employed. A low viscosity oil (*TT 9*) was injected on the running track with a syringe having attached to it a high accuracy dispenser $(3 \times 0.2[\mu l])$. To spread the oil along the track, the disc was driven at a low speed for several minutes, then the running track was inspected with a $5\times$ magnification lens to check whether the oil was uniformly spread. Subsequently, the film thickness was measured as a function of speed. The sequence of tested speeds starts with $0.02[m/s]$ and increase with 20% increments up at $0.5[m/s]$. Higher speeds can be tested, but the oil distribution would be seriously affected by the centrifugal force. In Figure 4.19 the central film thickness (h_c) is plotted versus entrainment speed (u_m) for starved and fully flooded conditions. Up to $0.08[m/s]$ the central film thickness for starved conditions coincides with the corresponding value for the fully flooded case. However, above $0.1[m/s]$ the speed is too high for sufficient oil replenishment on the track to accomplish a fully flooded lubricant film. Consequently, the central film thickness drops below the fully flooded value. Please note that the points plotted in Figure 4.19 for the case of starved lubrication are still in a transient state. The film thickness at the corresponding entrainment speed will decrease even more until a steady replenishment rate is reached.

The effect of replenishment rate can be investigated observing an EHL contact functioning with a high viscosity oil (*HVI 650* @ $80[^\circ C]$) and varying the rolling speed. In this way the time delay between consecutive overrollings is changed and with it the replenishment rate. Figure 4.20 shows maps of the contact loaded with $20[N]$, rolling at different entrainment speeds. Each map can be interpreted as a deformed ball surface in contact with a flat "rigid" surface. The map corresponding to $0[m/s]$ shows the state of the contact after prior running with an uniform lubricant distribution. Trapped lubricant can be observed inside the contact region. As the disc begins to rotate ($0.04[m/s]$) a thin EHL film is formed, with two minima along the sides of the contact. For the next speed in the sequence ($0.07[m/s]$) a narrow strip with film thickness values comparable with those from the contact side emerges. As the rolling speed increases (0.15 and $0.18[m/s]$), the strip enlarges towards the sides
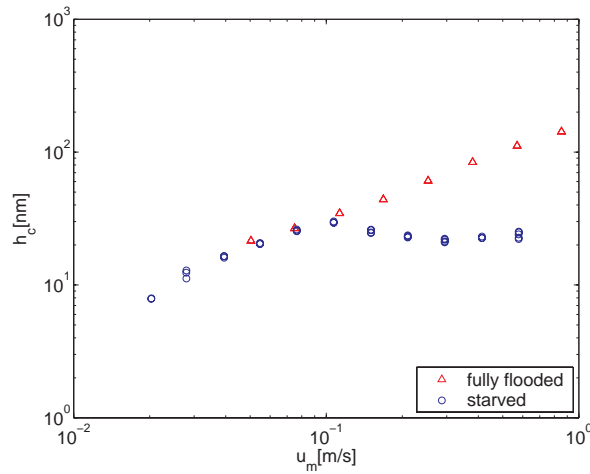
FIGURE 4.19: *Central film thickness as function of mean entrainment speeds in starved and in fully flooded conditions using a steel ball $R_x = R_y = 9.525[mm]$, a TT9 oil at $25[°C]$ and $20[N]$ load*

of the contact and records even lower values that those from the side of the contact. For the maps corresponding to 0.21 and $0.31[m/s]$ it becomes clear that the central region of the contact is severely starved, while the sides of the contact remain well lubricated due to the combination of side flow and replenishment. Moreover, for the $0.53[m/s]$ map it can be noticed that one side of the contact is better lubricated than the other. This is due to the effect of the centrifugal force that favors the lubricant from one side to flow towards the running track or away from the running track on the other side. Another observation is that around $0.5[m/s]$ the inlet meniscus reach the contact region, which is when the central film thickness starts to be affected.

Depending on the type of application and its magnitude the centrifugal force can be beneficial or harmful. For example the lubrication of a thrust bearing is positively influenced by a large centrifugal force because the oil is pushed to the locations where is mostly needed, i.e. on the running track. To support this statement an experiment was conducted with steel ball loaded against the glass disc and a limited amount of *HVI 60* oil was supplied to the running track of a glass disc at room temperature ($25[°C]$). The speed of the disc was increased from 0.1 to $2.3[m/s]$ with 20% increments while the ball was rotating freely on a carriage (pure rolling). The central film thickness was measured at different rolling speeds. The results are presented in Figure 4.21. In the same plot measurements for fully flooded conditions are shown. The measurements show a drop of the film thickness below the corresponding fully flooded values at speeds around $1[m/s]$. As the rolling speed is increased even further, the central film thickness recovers and eventually reaches the fully flooded value. Compared to a fully flooded situation, the central film thickness starts to decrease around
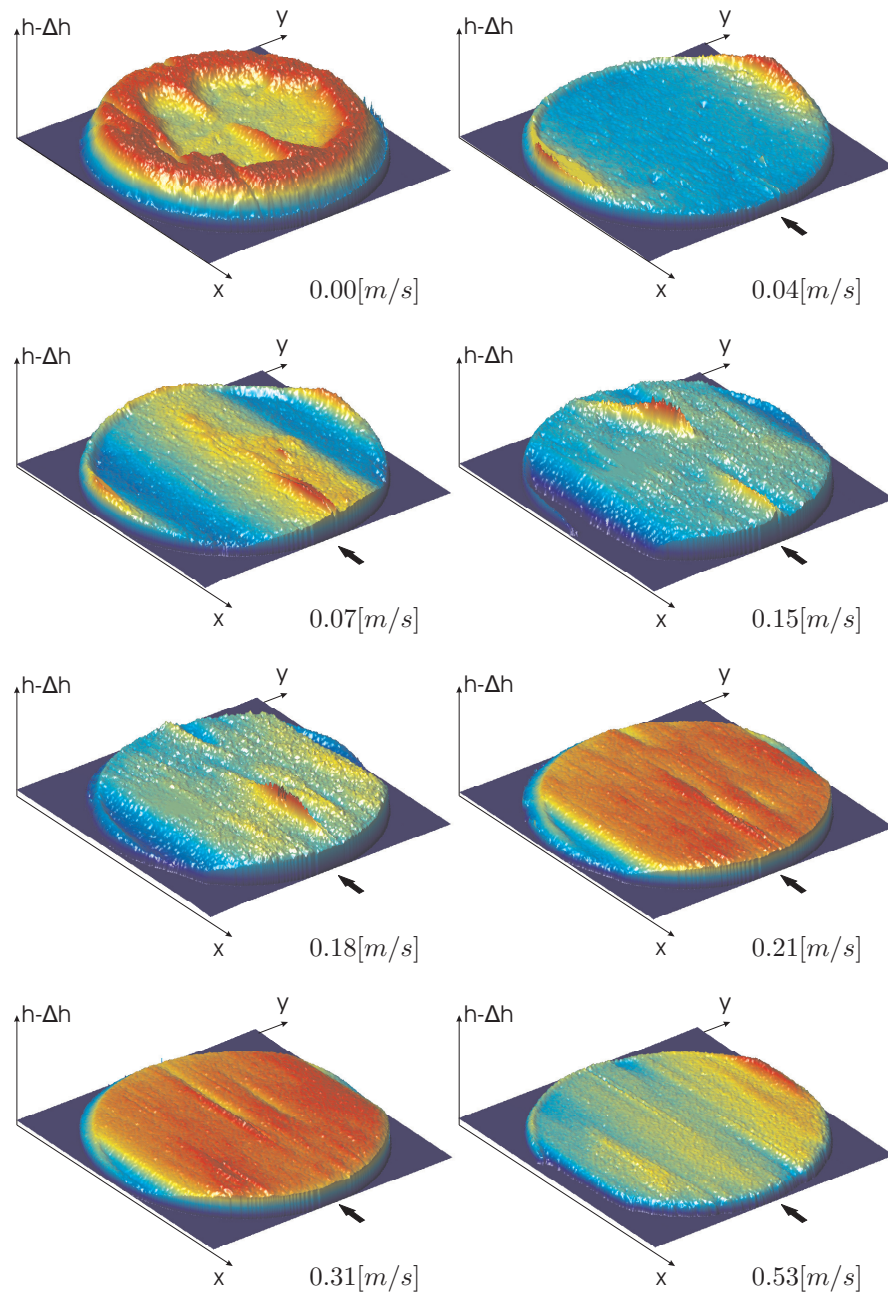
FIGURE 4.20: *Maps resulting from interferometric images of an EHL contact lubricated with 200 [μl] of HVI 650 at 80[°C], loaded with 20[N] at different speeds. The arrow indicates the direction of flow.*
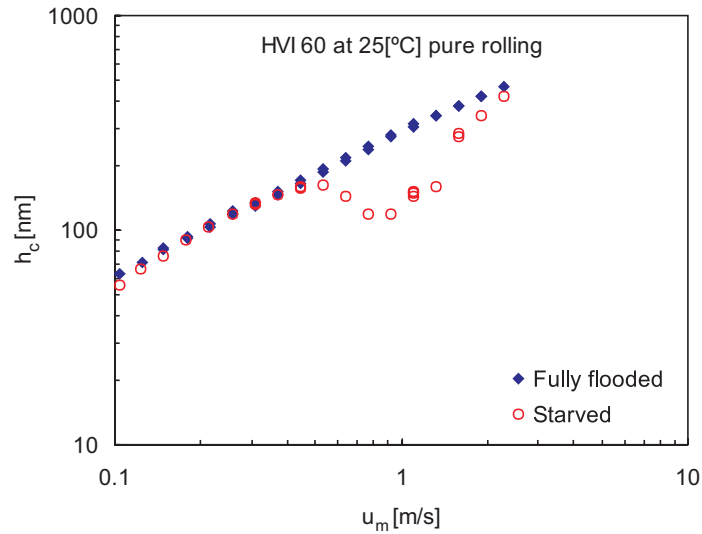
FIGURE 4.21: *The central film thickness as function of rolling speed in fully flooded and starved conditions under the influence of centrifugal force*

$0.5[m/s]$, it has a minimum value at around $0.9[m/s]$, then its value teds towards the fully flooded value again. At $2.3[m/s]$ the oil available on the disc is completely pushed to the running track, resulting in fully flooded conditions.

Interferometric images and film profiles transversal and longitudinal to the running direction are shown in in Figure 4.22 for a number of representative rolling speeds. In these images it can be noticed that around $0.5[m/s]$ the central film thickness is already influenced by the oil wake left by previous over-rollings. As the rolling speed increases, the wake has less time to recover, and starved lubrication takes place. Around $1.1[m/s]$ the effect of the centrifugal force on the oil distribution plays an important role, the oil replenishment on the running track becomes more effective on one side of the oil track and less effective on the other side.

4.2.2 Measurements of the inlet oil layer

The objective of measurements is to analyze the response of an EHL contact to the lubricant supply at different rolling speeds. For this purpose an oil layer that can be controlled, reproduced and measured is an essential prerequisite. To obtain starved lubrication and an oil layer that can be measured (in the range of the white light wavelength), only a limited supply of oil is necessary. The amount of lubricant that would give starved lubrication and optimal (oil layer) measurement conditions was found in the range 0.2 to $10[\mu l]$. An oil which is easy to handle in these conditions is TT 9, see Appendix C.

The gap height in the center of the contact and the oil layer at $500[\mu m]$ from the contact center was measured. Measurement of the oil distribution in the outlet in

FIGURE 4.22: *Interferometric images and film profiles at $x = 0$ and $y = 0$ (HVI 60 at $25[^\circ C]$ and $20[N]$)*

this way is feasible, but more difficult, because the fringe visibility is too low to distinguish between different interference orders. This is partly due to air bubbles and specific shape of the cavitation pattern in the outlet region, e.g. "tails" of the outlet meniscus, which extend far behind the contact.

The measurements were conducted in two modes:

- measurements of the wavelength along the scanned profile with white light, using a $10\times$ magnification lens (improved accuracy);

- image acquired with monochromatic light, using a $5\times$ magnification lens (improved overview)

The reader, should note that the scans for a given speed are made one at a time. This implies that the lubricant distribution can change during the scan at the inlet and at the contact center. This change is caused by the random pockets of lubricant adjacent to the running track.
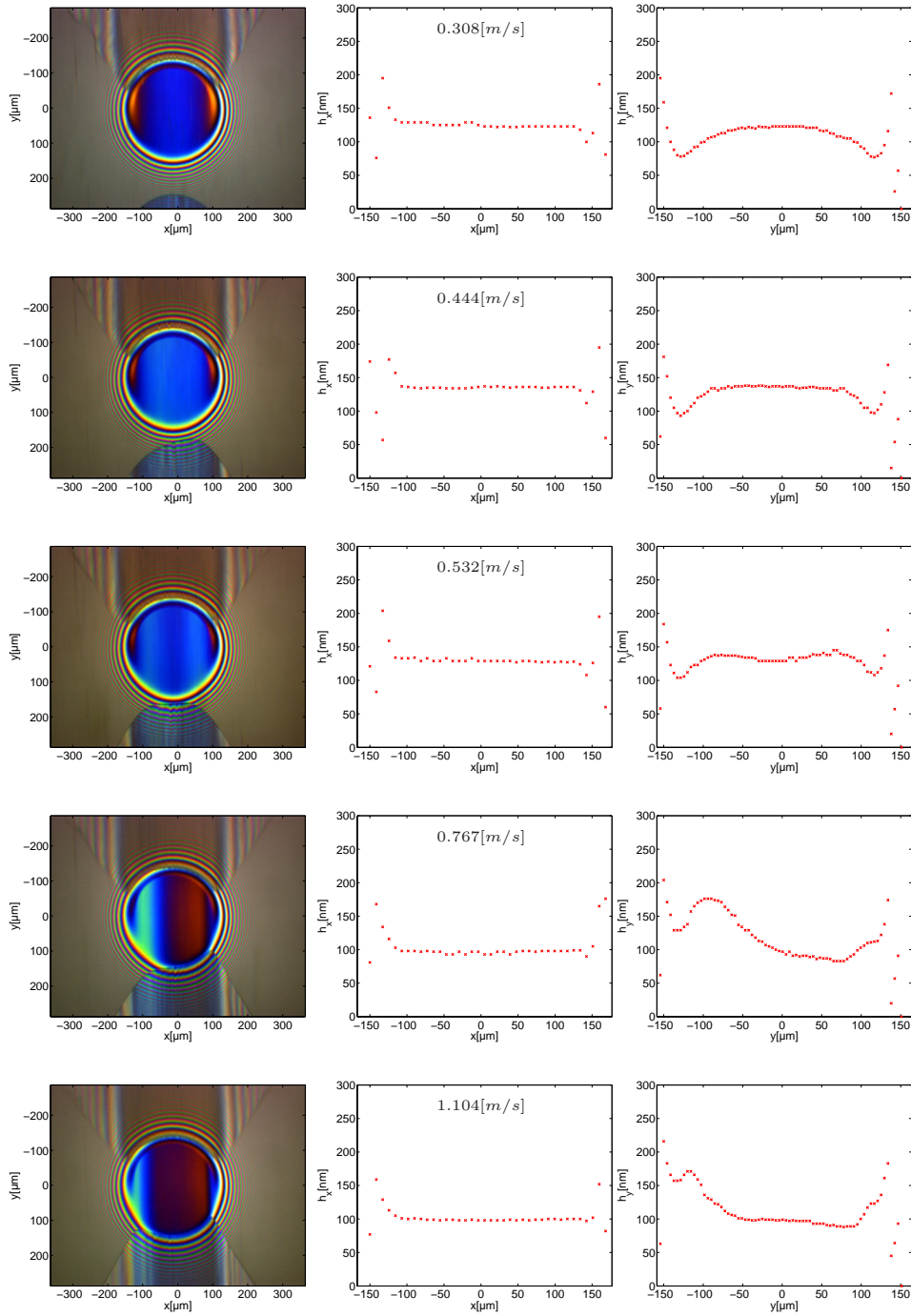
Figure 4.23 shows interferometric images (left) and scanned profiles (right) acquired at different rolling speeds for $20[N]$ load, $0.6[\mu l]$ of *TT 9* injected on the running track. In the plots corresponding to $u_m = 0.020$ and $0.04[m/s]$ the lubricant distribution in the inlet looks very much like a normal (Gaussian) distribution. At these low speeds the gas dissolved in oil spreads in a large bubble at the exit of the high pressure region. This bubble does not break through the outlet meniscus and the lubricant distribution in the outlet is given by the oil present in the gap between the ball and the disc. This distribution can be found in the inlet region, though somehow flattened if the elapsed time between overrolings is large (low speeds). The same behavior is observed in the acquired interferometric images.

As the rolling speed increases the gas bubble breaks through the meniscus and two side levees (embankments) are formed. The levees are partly visible in the last two plots from Figure 4.23. Up to $0.08[m/s]$ a difference between the inlet oil profiles can be distinguished at different speeds, above this speed the change is either too small or affected by the centrifugal force. The observation that the lubrication conditions does not change much is supported also by Figure 4.3 which shows that the central film thickness remains at the same level regardless of the magnitude of the entrainment speed.

The height of the levees is about $2300[nm]$, except for $0.08[m/s]$, for which the height of the ridges appears to be around $1500[nm]$ if the fringes are counted one by one, starting with order 3 ($548[nm]$ spacer layer). However, it can be argued that the fringe orders jump from 3 directly to 6. If this is true the height of the ridges reaches $2300[nm]$ as for the other cases.

For the monochromatic setup the fringe visibility decreases as the disc speed is increased. The fringes can still be distinguished and counted for the image corresponding to $0.04[m/s]$ from Figure 4.23, the other interferometric images being of

use for qualitative analysis. Still, the images with poor fringe visibility from Figure 4.23 give a good indication about the location of the levees.

The oil layer was measured only on the disc; whatever oil layer exists on the ball could not be quantified. Even so, a crude estimate can be made taking into account the length of the running track on the disc and assuming there is no loss of lubricant. On a running track with a radius of $40[mm]$ and a ball radius of $9.525[mm]$ about 80% from the total amount of oil should be found on the track from the disc and 20% on the ball circumference.

4.2.3   Theoretical results: Constant inlet layer

A thin, uniform layer of lubricant is hardly ever encountered in practice. However, this theoretical case is an excellent example for the establishment of some basic effects of lubricant starvation on the pressure distribution and film thickness. Some results are presented for an elliptic EHL contact with operating conditions from the experimental setup of a roller with $I\!D = 0.136$ loaded against the glass disc with $18[N]$, a rolling speed of $1.28[m/s]$ and pure rolling conditions. The viscosity at the ambient pressure and the viscosity-pressure index were chosen for the *TT 9* oil at $40[^\circ C]$ (see Appendix C). The oil distribution in the front of the contact was considered as a uniform layer with a given thickness h_{oil}. The thickness of the oil layer is specified relative to the value of the central film thickness under fully flooded conditions. The range varies from "fully flooded" ($h_{oil} = 8h_{cff}$) down to a thickness of $1/8$ from the central film thickness in fully flooded conditions.

As explained in Chapter 2 the starved contact model uses a variable referred to as the fractional film content, θ. By definition the product of θ with the computed film thickness H yields a graph that can be seen as the footprint of the contact in a single layer of oil. Inside the contact region, where pressure is generated, it represents the film thickness. In the cavitated/starved region it represents the total amount of lubricant present in the gap as if projected on one of the surfaces. As an illustration of a starved contact, Figure 4.24 shows such a plot for the conditions mentioned above and $h_{oil}/h_{cff} = 1$.

In Figure 4.25 the response of the central and minimum film thickness to the supplied oil layer thickness is given. The trend that should be observed is that of a decreasing central and minimum film thickness as a result of reducing the oil supply. For $h_{oil} > 2h_{cff}$ the contact achieves its full film formation capacity. For $h_{oil} \leq 2h_{cff}$, with a decreasing oil supply the central and minimum film thickness are dramatically reduced. For inlet oil layers of $h_c \propto h_{oil}/(\rho(p_h)$ a remarkable efficiency of a starved contact can be noticed. Almost all the available lubricant contributes to the separation of the surfaces. Furthermore, it can be noticed that for a decreasing oil supply, the central and minimum film thickness become equal. This implies that the film thickness in heavily starved contacts tends to be uniform across
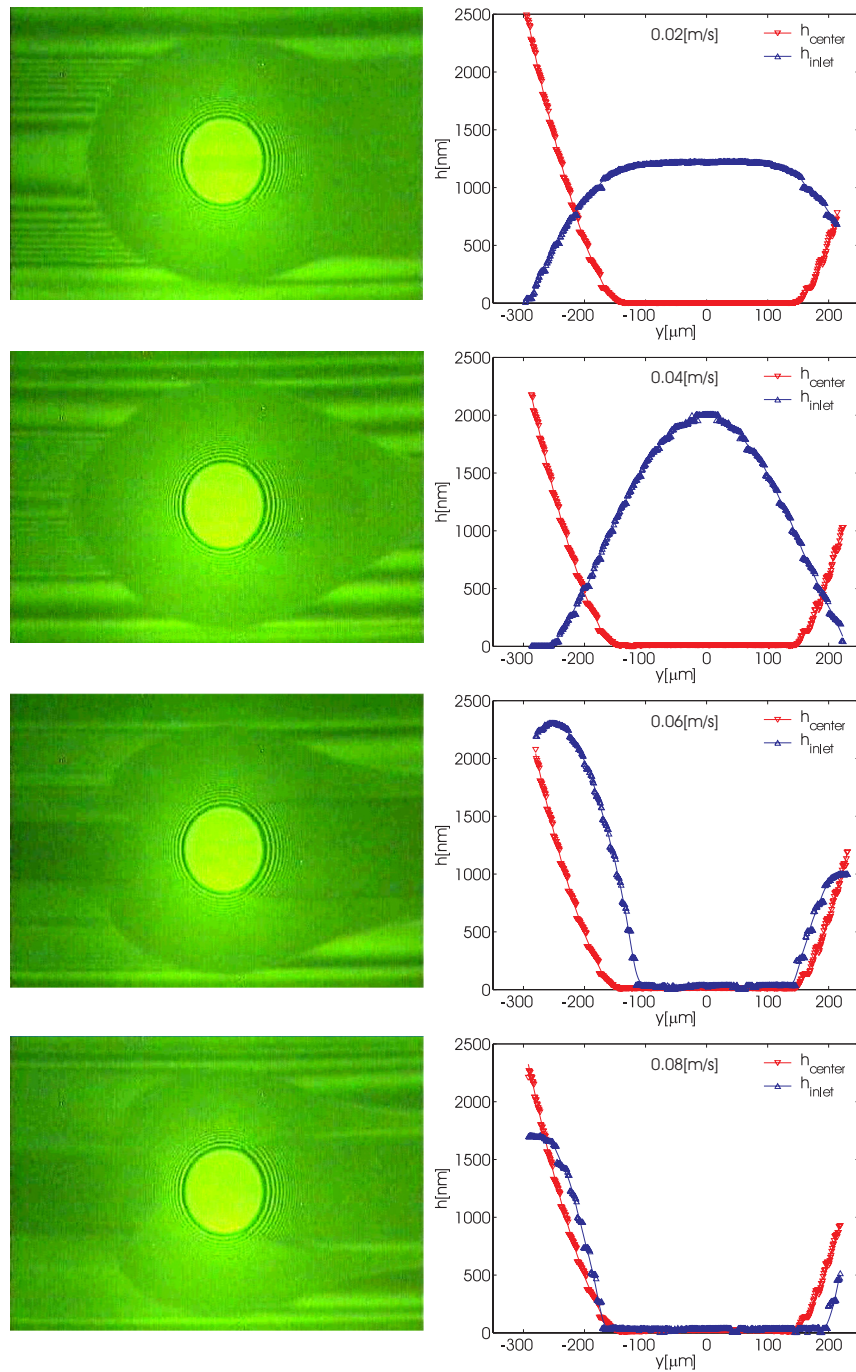
FIGURE 4.23: *Oil layer measurements: interferometric images (left) and scanned profiles (right) acquired at different rolling speeds for $20[N]$ load, $0.6[\mu l]$ of TT 9 injected on the running track, and room temperature ($25[^\circ C]$). The inlet profiles are acquired at $500[\mu m]$ from the contact center, see Figure 3.12*

the contact. This is to be expected as the limiting case is the dry contact with $h = 0$ as the solution.

These effects are illustrated more clearly in Figure 4.26, where profiles of lubricant distribution, gap height, pressure and fractional film content (θ) are displayed. Notice that the shape of the film thickness and pressure distribution change as the amount of oil is diminished. The side lobes disappear, the film profile flattens gradually and the pressure distribution approaches the Hertzian solution. More extensive series of results are given by Damiens [18].

4.2.4   Theoretical results: Variable inlet layer

The assumption of a constant lubricant supply layer is a major simplification of the situation that appears in contacts in real rolling bearings. Each contact runs on the footprint left behind by the previous contact. Replenishment from the sides in the time between overrollings as well as cage effects will alter the shape of the layer. Recently, Damiens [18] investigated the relation between harmonic oil layer variations in the inlet and the resulting local film thickness variations inside the contact. The results presented in this section follow the same approach. The objective is to derive a simple engineering formula that predicts the amplitude of the film oscillation inside the contact as a function of the amplitude of the layer oscillation and the operating conditions, including the degree of starvation. Combining such a formula with Fourier analysis of the oil layer harmonics, yields the possibility to predict the film shape inside the contact resulting from an arbitrary shape of the inlet supply layer. This approach has been very successful for the prediction of surface roughness effects on the film thickness, see Venner and Morales [74], Venner and Berger [76], Hook [38], etc. Because the fractional film content and the film thickness appear together in the advective terms in the Reynolds equation one may expect that a similar approach will work when predicting the film thickness oscillations resulting from spatial oil supply variations.
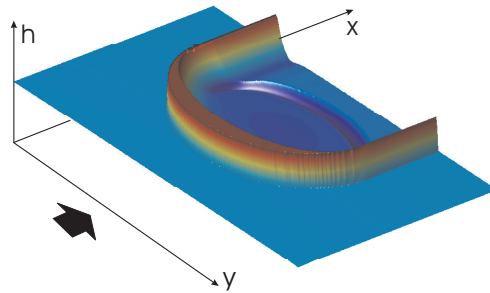
FIGURE 4.24: *Lubricant distribution $\theta \times h$ for $h_{oil}/h_{cff} = 1$, TT 9 oil at $40[°C]$ $18[N]$ load, $I\!D = 0.136$ radius ratio and $1.28[m/s]$ entrainment velocity*
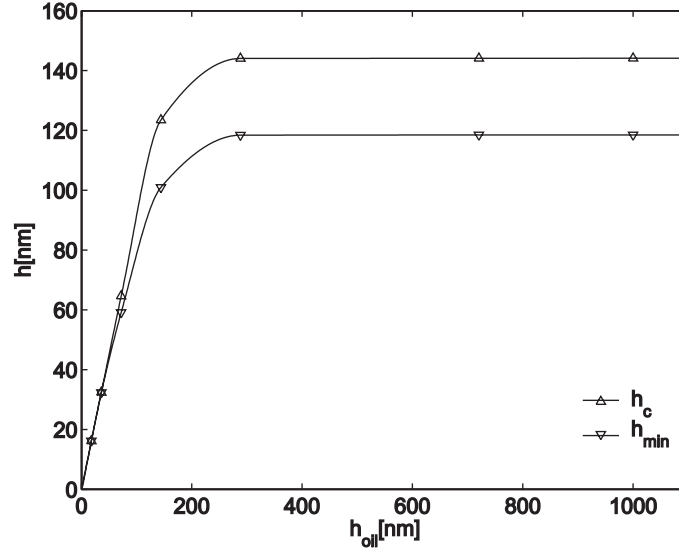
FIGURE 4.25: *Central and minimum film thickness for TT 9 at* $40[°C]$, $F = 18[N]$, $D = 0.136$, $u_m = 1.28[m/s]$ *as function of oil supply*

The steady state problem is considered with oil layers which are introduced at the inlet boundary by

$$H_{oil}(Y) = \overline{H}_{oil}\left[1 - f_a cos\left(2\pi\frac{Y}{\mathcal{W}_Y}\right)\right] \tag{4.9}$$

The amplitude of the oil layer harmonics is given by $A_i = \overline{H}_{oil} \times f_a$, with $f_a \in [0,1]$. Figure 4.27 shows a typical solution. The figure shows the footprint of the contact and the cross-stream centerline profiles of pressure, film thickness, and oil layer distributions. It can be seen that the oil layer variations affect the pressure distribution and generate a harmonic oscillation of the gap height with the same wavelength as the input layer variation. However, the inlet layer oscillations are not fully transmitted into the contact. The amplitude of the film thickness oscillations is smaller than the amplitude of the inlet layer oscillation. The ratio of amplitude of the film oscillations in the contact to the amplitude of the layer oscillation has been studied in relation to the operating conditions and the degree of starvation. The fact that it will depend on the degree of starvation is obvious. When the nominal thickness of the layer increases the contact will appear more fully flooded and the resulting film oscillations will be smaller.

By means of numerical simulations the behavior of the reduced corrected amplitude $\rho(p_H)A_c$ in the center of the EHL contact was monitored in relation to the operation conditions, wavelengths and the degree of starvation. The correction for the
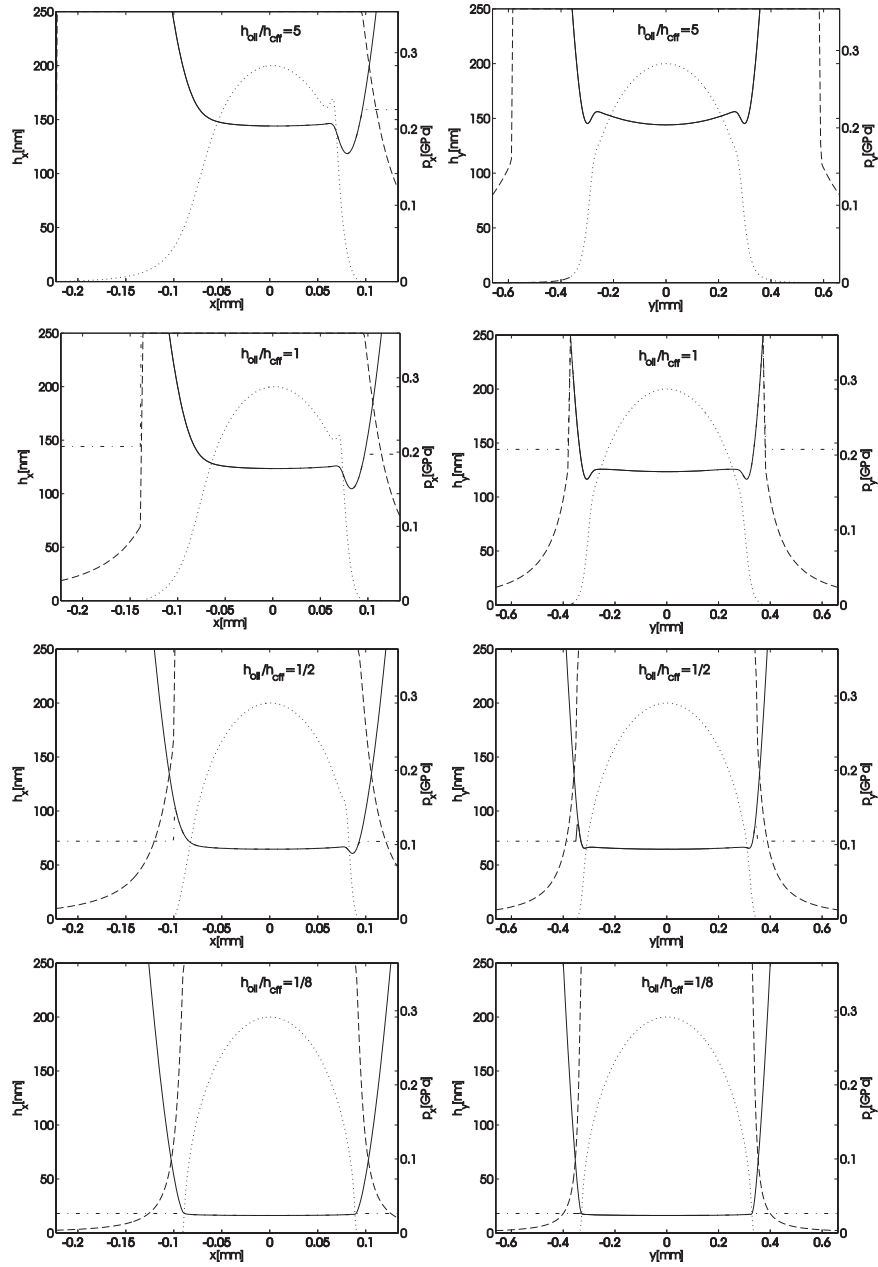
FIGURE 4.26: *Profiles of lubricant distribution (dash-dotted line), gap height (solid line), pressure (dotted line) and the fractional film content (dashed line) for TT 9 at* $40[°C]$, $F = 18[N]$, $D = 0.136$, $u_m = 1.28[m/s]$
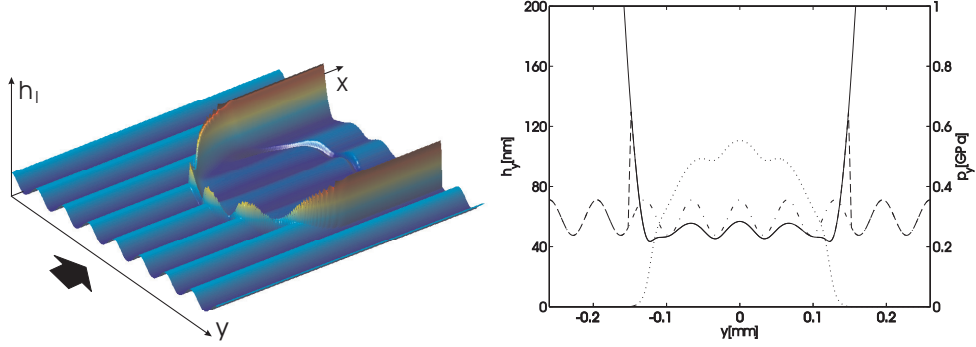
FIGURE 4.27: *Lubricant content and cross section of the pressure distribution and gap height at $X = 0$ for $M = 100$, $L = 5$, $\overline{H}_{oil}/H_{ff} = 0.5$, $f_a = 0.2$, $\mathcal{W}_Y = 0.5$*

M	L	$\mathcal{W}_Y$	$\overline{H}_{oil}/H_{cff}$
		0.25	0.1
100	10	0.5	0.25
100	5	1	0.5
20	10	2	0.75
20	5	4	1
			1.5

TABLE 4.4: *Input conditions for longitudinal lubricant layer oscillations*

compressibility $\rho(p_H)$ is introduced to allow the $\rho(p_H)A_c/A_i$ ratio to reach unity, as explained in more detail by Damiens [18].

Assuming small variations one may expect the ratio gap height oscillation amplitude to the inlet oil layer oscillation amplitude be independent of the last. In other words, in the present simulations the relative variation of the inlet oil layer oscillation is fixed. In the present study, a variation factor f_a of 0.2 was used.

The results of numerical calculations with combinations of input parameters presented in Table 4.4 are shown in Figure 4.28 in a plot of $\rho(p_H)A_c/A_i$ as a function of an operating conditions parameter C_D, introduced by Damiens [18]

$$C_D = \frac{r\kappa}{\mathcal{W}_Y}\sqrt{\frac{L}{M}} \qquad (4.10)$$

with r a dimensionless relative lubricant layer thickness given by H_{oil}/H_{cff}.

A curve that describes the distribution of the computed values can be written as:

$$\frac{\rho(p_H)A_c}{A_i} = \frac{1}{1 + C_D + 5C_D^2 + 50C_D^3} \qquad (4.11)$$

The parameter C_D (4.10) contains the degree of starvation ($r = H_{oil}/H_{cff}$), the
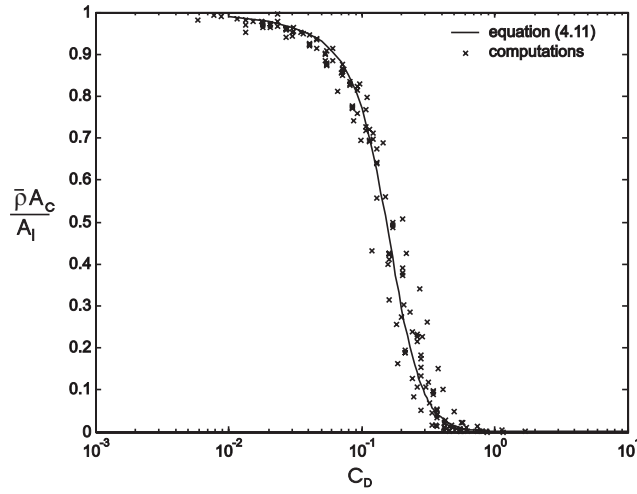
FIGURE 4.28: *Amplitude modification factor as function of C_D*

inlet length of the contact ($\sqrt{L/M}$), the wavelength of the harmonic pattern $\mathcal{W}_Y$, and the geometry of the contact κ.

Please note that Figure 4.28 shows the same behavior as was found for the deformation of roughness in the contact, see Figure 2.6 or [74], [76], [38]. This was to be expected as explained above.

The role of the different parameters can be understood as follows. For a decreasing degree of starvation (increasing H_{oil}/H_{cff}), the contact approaches the fully flooded conditions and is thus less sensitive to supply variations. Hence, layer oscillations do not lead to film thickness oscillations. For a given degree of starvation the extent to which the inlet oil layer oscillations are advected into the contact as film thickness oscillations depends on the ratio of the wavelength of the oscillation to the inlet length of the contact. Over this distance the transition from Poisseuille flow dominance to shear flow dominance takes place.

If the wavelength is small compared to the inlet length the layer oscillations are advected into the contact with an amplitude equal to the initial oil layer amplitude corrected by $\rho(p_H)$ which accounts for the compressibility effect. On the other hand, for an increasing wavelength of the oil layer oscillation at the inlet, the influence decreases in importance and any layer oscillation cancels upstream of the contact.

The effect of contact geometry (κ) shows that wide elliptic contacts hamper the the side flow and favor the transfer of the inlet oil layer oscillation to the contact center. Please note that this is true only for circular and wide elliptic contacts. Narrow elliptic contacts have not been included in the present study.

TRANSIENT LUBRICATION

Detailed understanding of a single EHL contact behavior under time varying conditions is required for many applications. Time varying conditions lead to vibrations that are carried to the surrounding structure and contribute to the generation of noise. In order to predict or prevent these undesired phenomena much research has been carried out to develop models that can predict how a single EHL contact behaves under time varying operating conditions. This is also the subject of the present chapter, namely the response of a single EHL contact to start up for ideal as well as poor lubrication conditions, the effect of a sudden increase of load, variable lubricant supply, the repeated overrolling, and the replenishment rate in the inlet region.

5.1 Start-up of EHL contacts

The start up motion for a single contact between a steel ball and a glass disc has been studied recently by Glovnea and Spikes, [24]. In their experiments large oscillations (not predicted by theory) were observed when the central thickness was measured. This problem was also studied theoretically by Zhao et al. [66] and Holmes et al. [34]. For moderate accelerations the results were as expected: the film thickness increased with time until the steady state value was reached, with good agreement between theoretical and experimental results. However, the oscillatory behavior observed in experiments, could not be explained satisfactory. In this section a model for the experimental start-up setup will be described. The model is used to investigate the influence of system dynamics on the film thickness in an EHL contact during start-up. The results are also presented in [61] and [77].

In Figure 5.1 a representation of the loading system that was used for the ball on disc apparatus by Glovnea and Spikes [24] is given. The load is applied by a system consisting of a mass m_2 via a lever and a spring. The dimensionless equation of motion for this case can be written as

$$\frac{1}{\Omega^2}\frac{d^2\Delta}{dT^2} + \frac{3}{2\pi}\iint_S P(X,Y,T)dXdY + \overline{K}\cdot\Delta = 1 + \overline{K}\cdot\Delta_\infty \qquad (5.1)$$
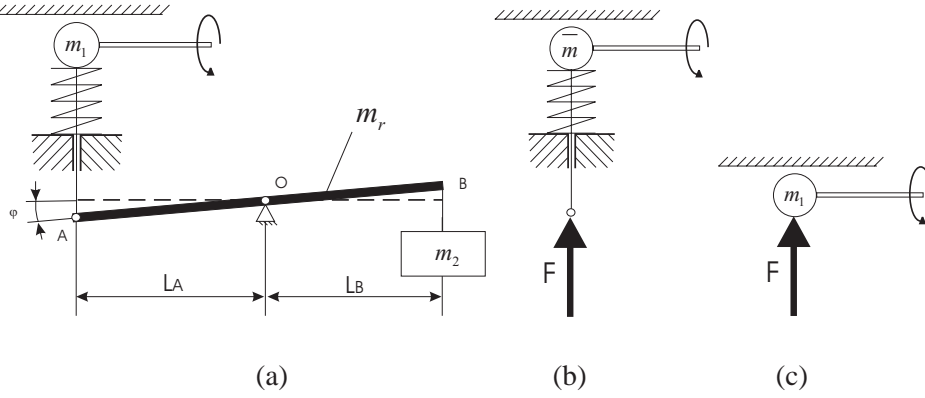
FIGURE 5.1: *(a) Loading system with lever and mass, (b) Representation as single mass system, and (c) Simplification to only inertia effect*

where Δ_∞ is the value of the approach at equilibrium, taken equal to the value of Δ for the steady state lubricated contact and Ω is the dimensionless natural frequency

$$\Omega = \sqrt{\frac{F_N \cdot a^2}{\overline{m} \cdot c \cdot u_m^2}} \qquad (5.2)$$

in which $\overline{m}$ denotes the equivalent mass of the system defined as

$$\overline{m} = m_1 + m_2 + \frac{I_O}{L_A^2} \qquad (5.3)$$

with m_1 representing the mass of the ball, and m_2 of the weight. The parameter $\overline{K}$ in (5.1) is a dimensionless parameter given by

$$\overline{K} = \frac{K \cdot c}{F_N} \qquad (5.4)$$

where K represents the dimensional spring constant, F_N the nominal load, and c the Hertzian approach. The other parameters are explained in the Nomeclature.

In this system two effects influence the dynamic behavior of the contact: an inertia effect and an elastic effect. The system can be represented by the loading system model shown in the Figure 5.1 b taking the equivalent mass $\overline{m}$ instead of m_1. When removing the spring it reduces to the system depicted in Figure 5.1 c which was used by Wijnant et al. [82], [83], [84] and for which the dimensionless equation of motion is given by

$$\frac{1}{\Omega^2}\frac{d^2\Delta}{dT^2} + \frac{3}{2\pi}\iint_S P(X,Y,T)dXdY = 1 \qquad (5.5)$$

Finally, considering Ω infinitely large (neglecting inertia effects) Equation (5.5) reduces to the dimensionless force balance condition (2.29), generally used in EHL calculations.

Wijnant et al. [82], [83] have shown that the Hertzian dry contact is a very useful reference for interpreting the dynamic behavior of the lubricated contact. For dry contact the relation (dimensionless) force to (dimensionless) approach is known and, as a result, the dimensionless equation of motion (5.1) for this problem can be written:

$$\frac{d^2\Delta}{d\mathcal{T}^2} + \Delta^{3/2} + \overline{K} \cdot \Delta = 1 + \overline{K} \cdot \Delta_\infty \qquad (5.6)$$

with the dimensionless time given by

$$\mathcal{T} = t\sqrt{\frac{F}{mc}}$$

For the case of small oscillations around the equilibrium solution $\Delta_\infty \approx 1$, an analytic solution to the linearized equation is found as follows:

$$\Delta = 1 + \mathcal{A}\cos\left(\sqrt{3/2 + \overline{K}}\,\mathcal{T} + \Phi\right) \qquad (5.7)$$

where $\mathcal{A}$ and Φ are the amplitude and phase-shift determined by the initial conditions. For small amplitude oscillations the period of the oscillations is:

$$\lambda_{\mathcal{T}} = \frac{2\pi}{\sqrt{3/2 + \overline{K}}} \qquad (5.8)$$

In terms of the lubricated contact this means that the changes in the contact conditions will induce oscillations with a dimensionless period of oscillation:

$$\lambda_T = \lambda_{\mathcal{T}}/\Omega \qquad (5.9)$$

which are damped due to the dissipation in the lubricant film.

To check how accurate this analytical prediction is, numerical computations were carried out, based on the EHL model described in Chapter 2 and considering the equation of motion (5.1) instead of the force balance equation 2.29. The change of velocity $\overline{u}$, relative to the (nominal) steady state velocity u_m is controlled by the dimensionless velocity $\Lambda(T)$ starting up from zero speed with a certain acceleration until the target velocity u_m is reached as follows:

$$\Lambda(T) = \frac{\overline{u}(t)}{u_m} = \max(1, A_{cc}T) \qquad (5.10)$$

where A_{cc} is the dimensionless acceleration.

For the start up configuration the dry contact is the initial solution, with zero film thickness and the Hertzian pressure distribution in the contact region. This is achieved in a way similar to what is described in detail by Holmes et al.[35]. The film thickness is computed from (2.27) and the value of Δ is set such that the central film thickness is zero. Subsequently, the EHL equations (2.20), (2.27), (2.31), (2.30), and Equation (5.1) are solved simultaneously at each time step except for the points where the calculated film thickness is negative. For these points the film thickness is set to zero and the pressure to the Hertzian solution. As the transient solution develops and the film thickness builds up, small changes in the pressure distribution occur. Concerning the film build-up upstream of the contact region, this develops as if it was building up from a solution of the Reynolds equation with a very thin film.

The operating conditions are taken from the experiments with the ball on disc rig as given by Glovnea and Spikes [24], see Table 5.1. For the final entrainment speed, $u_m = 0.2[m/s]$, the measured value of the central film thickness given by Glovnea and Spikes [24] is about $108[nm]$. In Figure 5.2 the measured film thickness as a function of time is given for different accelerations. For an acceleration of $50[m/s^2]$ a large oscillation of the film thickness occurs before the contact settles at the steady state level. For the conditions listed in Table 5.1 on a 257×257 grid the steady state value obtained for the central film thickness is $101[nm]$. On a grid with half the mesh size a value of $102[nm]$ is obtained and on a grid with twice the mesh size $h_c = 97[nm]$. This indicates that the numerical error in the steady-state result is about one percent. When compared to the experimental result the predicted film thickness is about 7 percent too low. This difference may be due to inaccuracies in the EHL model or in the input parameters.

In order to separate the inertia and the stiffness effect first the results are presented for different values of Ω keeping $\overline{K} = 0$ (no spring) and then for a given value of Ω the effect of $\overline{K}$ on the contact behavior is shown. The objective is to illustrate the general trends occurring when these these parameters vary. With respect to the values these parameters have in the experimental setup, taking only the mass of the ball into account, the effective mass would give $\Omega \approx 5$ and when considering the effect of the lever and the additional mass this would drop to about $\Omega \approx 1$. For stiffness a value of $K = O(10^4)$ was given, which would give $\overline{K} = O(10^{-3})$. To reach a value of $\overline{K} = O(1)$ a spring with a constant of $K = O(10^7)$ would be required.

5.1.1   Inertia effect

In Figures 5.3 to 5.6 results are presented for the case $\Omega = 5.13$. In Figure 5.3 the profiles of the film thickness at the centerline of the contact $y = 0$ are shown at different times during the start up. Results for four values of the acceleration are shown: $a_{cc} = $ "∞" (sudden step), 50, 20, and $10[m/s^2]$. By sudden step it is meant that the final entrainment speed ($u_m = 0.2[m/s]$) is reached at the first time step. In Figure 5.6 the central film thickness and the mutual approach are shown as a function
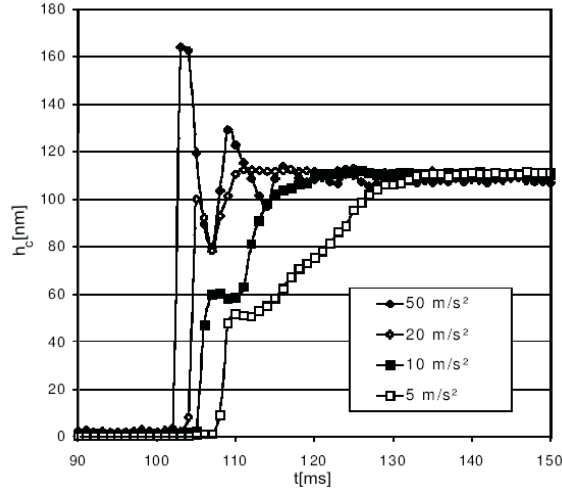
FIGURE 5.2: *Central film thickness h_c as a function of time t for different acceler-
ations $a_{cc} = 50, 20, 10$ and $5[m/s^2]$ as measured with the ball on disc apparatus
(courtesy Glovnea and Spikes [24])*

Parameters	Value	Dimension
F_N	20	$[N]$
R_x	9.525×10^{-3}	$[m]$
E_1 (*steel*)	210×10^9	$[Pa]$
E_2 (*glass*)	75×10^9	$[Pa]$
ν_1 (*steel*)	0.3	
ν_2 (*glass*)	0.25	
η_0	52×10^{-3}	$[Pa \cdot s]$
α	19.6×10^{-9}	$[Pa^{-1}]$
u_m	0.2	$[m \cdot s^{-1}]$
Hertzian Parameters		
a	1.369×10^{-4}	$[m]$
c	1.967×10^{-6}	$[m]$
p_H	5.098×10^9	$[Pa]$
Dimensionless Parameters		
M	213	
L	4.59	

TABLE 5.1: *Parameters of the contact on the ball on disc apparatus.*
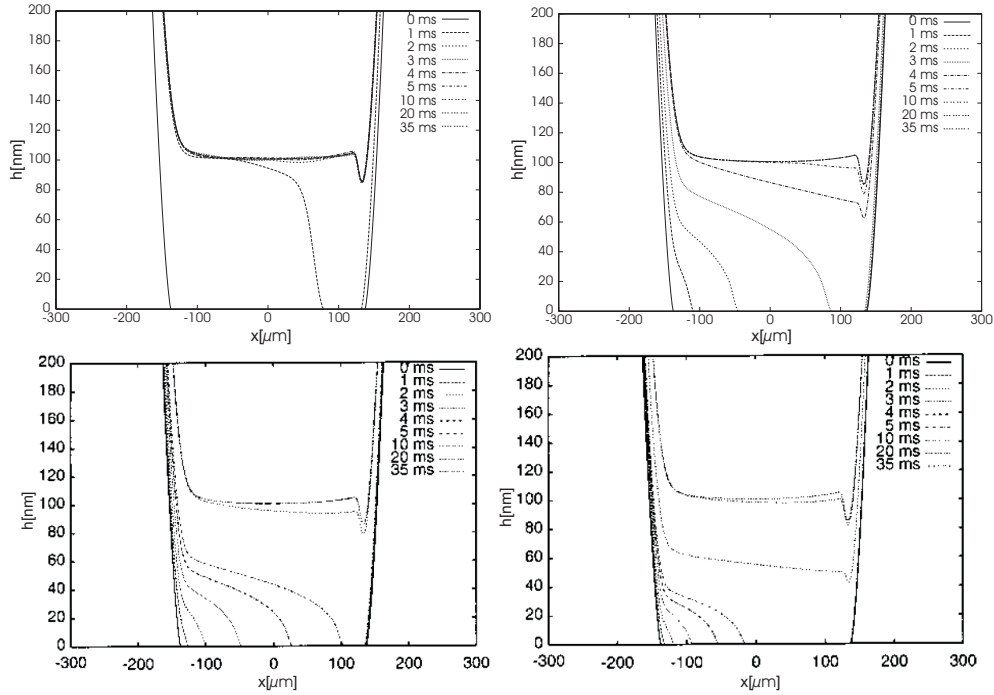
FIGURE 5.3: *Film thickness h at $y = 0$ (center line) as a function of x at different times when starting up with accelerations $a_{cc} = $ "∞" (top left), 50 (top right), 20 (bottom left) and 10 (bottom right) $[m/s^2]$, $\Omega = 5.13$*

of time for different accelerations.

For 50, 20, 10, and $5[m/s^2]$ Holmes et al. [35] have shown that, when assuming a fixed mutual approach, the central film thickness increases with time from the moment the film front reaches the center of the contact. The position of this front, i.e. the location of the separation point between the dry and lubricated part of the contact, is seen to move ahead at the entrainment speed $\overline{u}$. The position of the front wave as a function of time could be predicted straightforwardly from the entrainment speed versus time curve. The results presented here show the same overall behavior: an increasing film thickness in time with the slope depending on the acceleration. This aspect of the start up behavior is predicted quite accurately. In the numerical results presented here an oscillatory variation of the film thickness can be seen, which is caused by the inertia effects. However, the amplitude of the oscillation is small and its effect is hardly visible in the film thickness profiles shown in Figure 5.3. Nevertheless, for the larger accelerations the oscillatory behavior can be seen quite clearly in a central film thickness versus time plot such as Figure 5.6.

For the sudden step the amplitude of the oscillation in the central film thickness is about $1[nm]$ around $t = 3[m/s]$ and decreases with time due to the damping
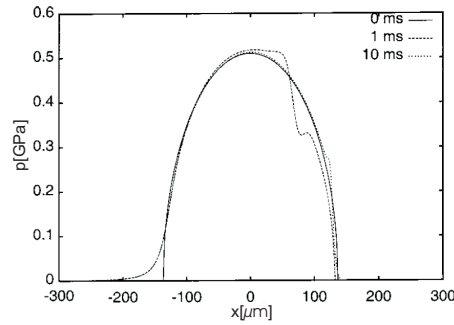
FIGURE 5.4: *Pressure p at y = 0 (centerline) as a function of x at different times when starting for $a_{cc} = $ "∞", $\Omega = 5.13$*
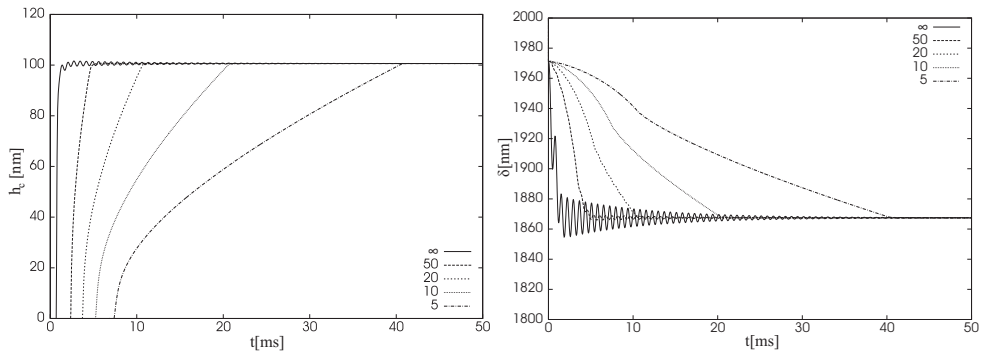
FIGURE 5.5: *Central film thickness h_c (left) and mutual approach (right) as a function of time t for different accelerations $a_{cc} = \infty$, 50, 20, 10, and $5[m/s^2]$; $\Omega = 5.13$; $\Delta t = 0.02[ms]$*
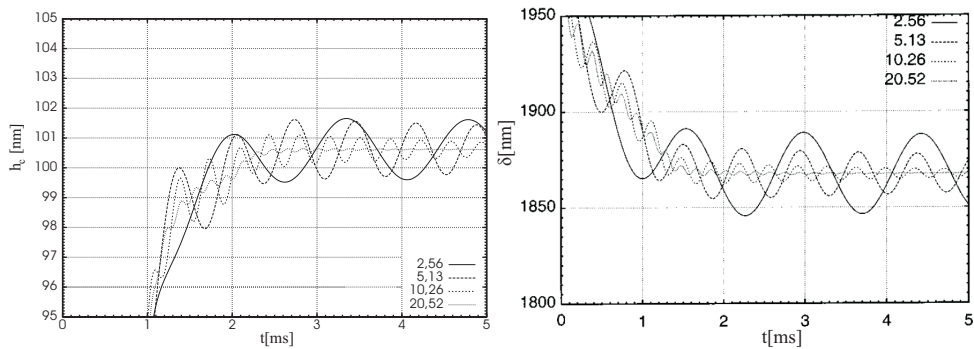
FIGURE 5.6: *Central film thickness h_c (left) and mutual approach δ (right) as a function of time t for $a_{cc} = \infty$ and $\Omega = 2.56$, 5.13, 10.26, and 20.52*

effects of the lubricant film. It has been reduced to $0.81[nm]$ around $t = 5[ms]$, to $0.5[nm]$ around $t = 10[ms]$ and at $t = 20[ms]$ it is $0.2[nm]$. As can be seen from the figures, the amplitude of the oscillation in the mutual approach is much larger. For the times $t = 3$, 5, 10, and $20[ms]$ the amplitude is 11.8, 9.5, 5.7, and $2.0[nm]$, respectively. This large difference in amplitude (between film and mutual approach oscillation) is explained as follows. Due to the high viscosities in the central region the film is so stiff compared to the elastic materials that the contact accommodates the oscillations by means of variation of the mutual approach, i.e. by means of the elastic deformation. It is therefore concluded that due to the high stiffness of the film in the central region, the dynamic behavior in terms of oscillation frequency can quite accurately be predicted from an analysis of the Hertzian dry contact. For example the wavelength of the oscillations in film thickness and approach in Figure 5.6 is $0.70[ms]$ with an estimated error of about $0.02[ms]$ (the size of the time step). The predicted value based on the analysis for the dry contact problem, see Equation. (5.9), is $\lambda_T \approx 5.13/\Omega$ which gives $\lambda_t \approx 0.68[ms]$.

So far only film thickness results were shown. Naturally also the pressure changes during the start up process. As an example in Figure 5.4 some of the pressure profiles associated with the film thickness results presented in Figure 5.3 ($a_{cc} = $ "∞", sudden step) are shown. In the figure the initial pressure distribution at $t = 0$ is shown, the pressure associated with the solution when the contact is already fully flooded at $t = 10[ms]$, and an intermediate solution at $t = 1[ms]$ when there is still partial contact. It can be seen that, when there is still contact, the pressure distribution in the flooded part (in particular in the inlet) is already very similar to the pressure profile for fully flooded conditions, whereas in the contact part it is still very close to the Hertzian starting solution. In the transition region from full film to zero film a clear pressure disturbance is observed associated with the moving film front, and the need to satisfy the equation of motion.

In Figure 5.6 the effect of the value of the inertia parameter Ω on the results is shown. The figure shows the central film thickness h_c and the mutual approach δ as a function of time obtained for $\Omega = 2.56$, 5.13, 10.26, and 20.52. For clarity only the first 5 milliseconds are displayed and an enlarged scale is used. The wavelength in time of the oscillation for the four cases is 1.43, 0.70, 0.36, and $0.19[ms]$, respectively, again with an estimated error of about $0.02[ms]$. So, doubling Ω means a twice larger oscillation frequency, exactly as predicted by the dry contact analysis, and the oscillation frequency predicted based on this theory is indeed observed in the calculations. Finally, in Figure 5.6 it can be seen that the amplitude of the oscillation decreases with increasing Ω. This is natural as a larger Ω implies a smaller inertia and a quicker response of the contact to changes. Eventually for large enough Ω a smooth curve will result as when assuming force balance.

Summarizing, from vibrational point of view, during the start up the lubricated
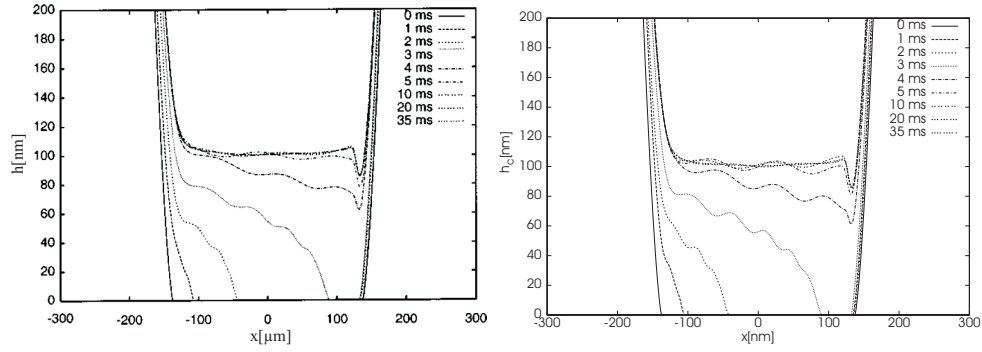
FIGURE 5.7: *Film thickness h_c at $y = 0$ at different times during start up, $\Omega = 5.13$, $a_{cc} = 50[m/s^2]$, $\overline{K} = 1$ (left), $\overline{K} = 2(right)$*

contact behaves like the Hertzian dry contact except for the fact that the oscillation is damped. In the lubricated contact the damping is caused by the dissipation occurring in the lubricant film.

5.1.2 Stiffness effect

In the previous subsection it was shown that the effect of inertia on the film thickness during the start up is rather small for the assumed load conditions. Oscillations do occur but only for large accelerations the amplitude is sufficiently large for these oscillations to be visible in a film thickness versus time plot. Even for the sudden step their amplitude is less than a few percent of the steady state film value. As a result, in the graphs of film thickness as a function of space the oscillations are barely visible. This picture can change significantly when the elastic effect of the spring in the loading system is included. Based on the analysis for the Hertzian dry contact (presented above) it can be expected that the oscillation frequency increases. For $\Omega = 5.13$ and an acceleration of $50[m/s^2]$ the effect of the dimensionless spring constant $\overline{K}$ on the dynamic response of the contact in the start up process is illustrated in the Figures 5.7 and 5.8.

In Figure 5.7 the centerline film thickness profiles at different times during the start up process are shown for the cases $\overline{K} = 1$ and 2 (for $\overline{K} = 0$, see Figure 5.3). For $K \neq 0$ the profiles are no longer smooth functions. For $\overline{K} = 1$ they seem to exhibit a stepwise pattern but with increasing $\overline{K}$ it becomes clear that what is visible is an oscillatory pattern with an amplitude that increases with $\overline{K}$. The mechanism behind it is as follows. The combined effect of spring and inertia causes relatively large oscillations in the mutual approach. Because the response of the contact to mutual approach change is a narrowing or widening of the contact region (or high viscosity region), the main film changes occur in the inlet (or film front) region, and the outlet region. The effect visible in the graphs is the propagation of the changes that have occurred in the inlet (at the film front) into the contact or into the high viscosity
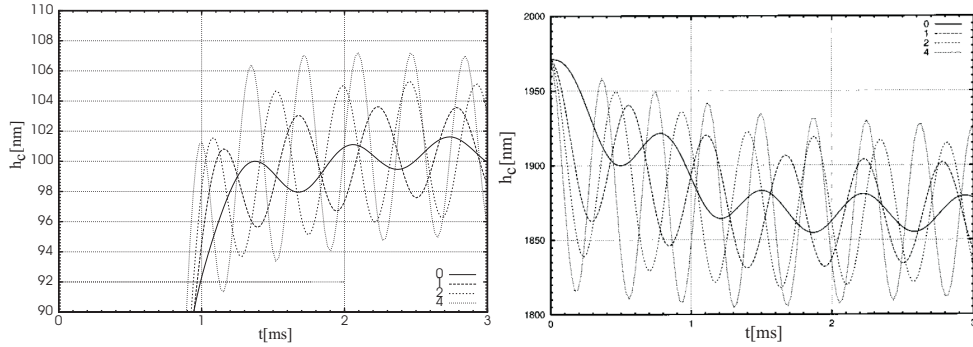
FIGURE 5.8: *Central film thickness h_c as a function of time for $\Omega = 5.13$, $a_{cc} = 50[m/s^2]$ and $\overline{K} = 1.0$ (right) and 2.0 (left)*

region. This propagation (advective) behavior is due to the shear flow dominance and is governed by the wedge and squeeze term of Reynolds equation (2.20). Note that in itself this mechanism has nothing to do with the spring. The same effect occurred for the case $\overline{K} = 0$ but there the amplitude of the changes was so small that it was hardly visible in the centerline film thickness graphs. Only for the sudden step Figure 5.8 a trace of it can be seen.

At any moment the changes occurring in the inlet are sent into the contact with the entrainment speed. If the entrainment speed is constant the propagation velocity is constant and a pattern emerges in the film profiles with a fixed wavelength. If λ_t is the wavelength at which the inlet oscillates in the high viscosity region as a function of x the pattern will have a wavelength $\lambda_x = \overline{u}\lambda_t$. For the problem considered here the entrainment speed starts at zero and increases with time. This leads to a situation in which a pattern of gradual elongation of the wavelength in space appears in the film profiles. This is most clearly visible for the curves for $t = 3[ms]$ in Figure 5.7. Going from the film front back into the inlet, the distance between the local minima, or steps, increases. The waves closer to the inlet are the result of an oscillation propagated at a higher entrainment speed, so it appears in the profile with a larger wavelength in x. This gradual elongation of the wavelength continues until the final entrainment speed is reached and pattern with a fixed wavelength in x direction emerges.

In Figure 5.8 the central film thickness and mutual approach as a function of time are shown for $\overline{K} = 0$, 1, 2, and 4. It can clearly be seen that the amplitude of the oscillations increases with increasing $\overline{K}$. Around $t = 3[ms]$ the amplitude of the film thickness oscillations is 1, 3, 4, and $6[nm]$, for $\overline{K} = 0$, 1, 2, and 4, respectively. The period of the oscillations in the computed results is 0.70, 0.56, 0.47, and $0.37[ms]$ with an estimated error of about $0.02[ms]$. The predicted values obtained from the dry contact analysis of Equation 5.9 are 0.68, 0.53, 0.45, and $0.36[ms]$. From $\lambda_x = \overline{u}\lambda_t$ it follows that the wavelength in x with which these disturbances will appear in the film profile will eventually be 136, 106, 90, and $72[\mu m]$.
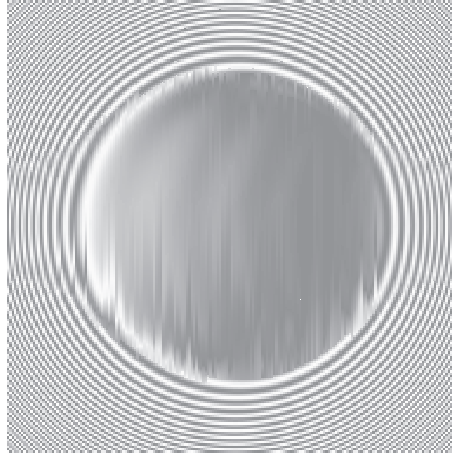
FIGURE 5.9: *Pseudo-interferometry plot of $H(X, Y)$ at $t = 3.4\ [ms]$ for $a_{cc} = 50$ $[m/s^2]$, $\Omega = 5.13$ and $\overline{K} = 2$*

Summarizing, the results presented here confirm that the dynamic behavior of the lubricated contact, in terms of the oscillation frequencies, is the same as that of the dry contact. So, the EHL contact accommodates force variations by means of the elastic deflection of the bodies and the EHL film is sufficiently stiff to remain relatively unaffected. In retrospect to [24] the results could have been expected in a situation where the deflection exceeds the film thickness by an order of magnitude.

To illustrate how the oscillations affect the film shape in the direction perpendicular to the entrainment Figure 5.9 presents a pseudo-interferometry picture of the film thickness at $t = 3.4\ [ms]$ in the start up process for the case $\overline{K} = 2$, $\Omega = 5.13$, $a_{cc} = 50[m/s^2]$. In the first few time steps the region in which the contact is still dry can be recognized. The film front with its semi-circular shape can clearly be seen to move ahead and out of the contact. Also the oscillations induced by the combined inertia and spring effect can be seen. Note that the propagated oscillations also appear with the same curved shape and that the wavelength in x of the oscillations increases (until it equals $\lambda_x = u_m \lambda_t$). Finally, the amplitude of the oscillations decreases with time due to the damping of the film and eventually the contact reaches the steady-state situation associated with the final entrainment velocity.

5.1.3 The effect of lubricant starvation

The effect of a limited lubricant supply on start up has also been investigated with the input parameters given in Table 5.1. For this case the solved equations are: (2.20), (2.27), (2.31), (2.30) and Equation (5.1), with the complementary condition (2.26).

In Figure 5.10 results are shown for $a_{cc} = 50$, $\overline{K} = 2$, $\Omega = 5.13$ and an inlet condition fully flooded, $h_{oil} = 100$, 50, and 25 $[nm]$ respectively.

The computed steady state film thickness for the contact for these starved cases is

$h_c = 77.1, 42.6$, and $21.5 \, [nm]$ respectively. These values illustrate a characteristic of the starved problem mentioned in Chapter 4. It is very efficient in terms of the ratio of the lubricant actually used for film formation to the amount of lubricant supplied in the inlet. For $h_{oil} = 100[nm]$ the layer of oil supplied is roughly equal to the central film thickness for the fully flooded case, and thus much smaller than the amount of oil supplied when the contact is fully flooded. Yet, the central film thickness for the starved contact is only 25 % smaller than the fully flooded value. This shows that most of the oil normally supplied will simply flow around the contact. With increasing degree of starvation the contact becomes even more efficient. When supplying a layer of $25 \, [nm]$ one obtains a central film thickness of $22 \, [nm]$ so in that case almost all the oil supplied is actually used to form the lubricant film. For a vanishing inlet oil layer, the value of the central film thickness for a starved contact will be $h_c = h_{oil}/\rho(p_H)$.

Figure 5.10 (left) shows the film thickness at $y = 0$ as a function of x at different times during the start up for $a_{cc} = 50 \, [m/s^2]$, $\Omega = 5.13$, $\overline{K} = 2$ and $h_{oil} = 100 \, [nm]$. The figure is very similar to the result obtained for the fully flooded contact, Figure 5.7, except that now the final level of the film thickness is smaller. The oscillations induced by the contact dynamics can still clearly be seen.

Also shown in Figure 5.10 is the ratio $h_c(t)/h_{cff}$ where h_{cff} is the steady state central film thickness for the fully flooded contact. For the start up problem, the general behavior of the starved EHL contact in terms of film thickness increasing in time is the same as for the fully flooded problem, except that the steady film thickness level is now attained earlier, namely at the value of the steady state film thickness for the starved contact. This implies that the start up time of the starved contact is shorter. An interesting further difference with the results for the fully flooded contact is that there is a small overshoot, i.e. the film thickness rises above the steady state starved value and then gradually approaches this value from above. The relative magnitude of this overshoot (relative to the steady state starved central film thickness) increases with increasing degree of starvation.

Superimposed on the film thickness behavior described above the oscillations induced by the contact dynamics occur. The frequency of the oscillations is not affected by the starvation which could be expected as the starved problem is closer to the limit of the dry contact problem. However, the absolute amplitude of the oscillations decreases. Another change is that with increasing degree of starvation the oscillation damps more slowly. This can be explained as follows. The oscillation is driven by the elastic deformation which is why the frequency is so accurately predicted by an analysis based on the Hertzian contact. However, it is damped because of the presence of the lubricant film with the major contribution to this damping coming from the low viscosity region immediately around the Hertzian contact region. With increasing degree of starvation the size of this region decreases and thus the damping.
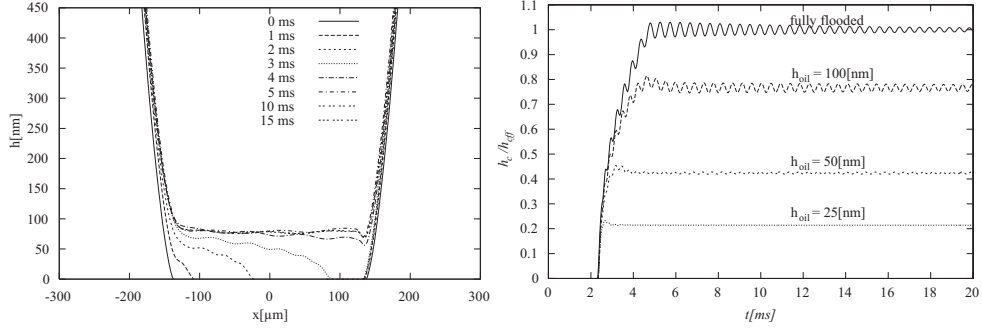
FIGURE 5.10: *Film thickness h as a function of x at $y = 0$ at different times during start up for $h_{oil} = 100$ [nm] (left) and ratio $h_c(t)/h_{cff}$ as a function of time for fully flooded, $h_{oil} = 100, 50,$ and 25 [nm]. $\overline{a} = 50$ [m/s^2], $\Omega = 5.13$, $\overline{K} = 2$(right)*

Finally, in Figure 5.11 a pseudo-interferogram of the dimensionless quantity $\theta \times H$, is shown. The white shape at the right of the picture is the footprint left behind by the contact at $t = 0$ when there was still contact everywhere.

5.2 The effect of impact on lubrication

The subsequent studied transient problem is that of a load increase in a short time interval. The load variations are described by the dimensionless function $\mathcal{F}(T) = F(T)/F_N$ and the results are presented as the response of the EHL contact to a linear increase of the load during a certain time interval according with:

$$\mathcal{F}(T) = \min(1 + \frac{\Delta \mathcal{F}}{\Delta T}T, 1 + \Delta \mathcal{F}) \qquad (5.11)$$

with $\mathcal{F}(T)$ a dimensionless load function given by $F(T)/F_N$ and F_N the nominal load. In this case the dimensionless equation of motion (5.1) becomes

$$\frac{1}{\Omega^2}\frac{d^2\Delta}{dT^2} + \frac{3}{2\pi}\iint_S P(X,Y,T)dXdY + \overline{K}\cdot\Delta = \mathcal{F}(T) + \overline{K}\cdot\Delta_\infty \qquad (5.12)$$

Similar to the analysis made for the start up, for a dry contact the relation between load and mutual approach is known and Equation (5.12) can be written as:

$$\frac{d^2\Delta}{dT^2} + \Delta^{3/2} + \overline{K}\cdot\Delta = \mathcal{F}(\mathcal{T}) + \overline{K}\cdot\Delta_\infty \qquad (5.13)$$

For small amplitudes the period of the oscillations for the dry contact is given by (5.8) and for the lubricated contact by (5.9).

Numerical simulations were run for load changes of 5, 10 and 20 [N] in a time interval of 1 [ms]. The input parameters are the operating conditions as listed in
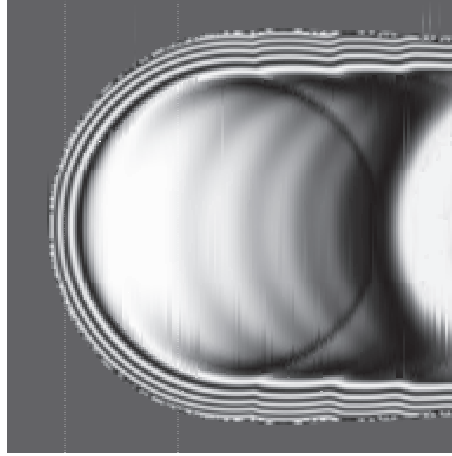
FIGURE 5.11: *Pseudo-interferometry plot of the "film layer"* $\theta \times H(X, Y)$ *at* $t = 3.4$ $[ms]$ *for* $\overline{a}_{cc} = 50\ [m/s^2]$, $\Omega = 5.13$, $\overline{K} = 2$ *and* $h_{oil} = 100\ [nm]$.

Table 5.1. The corresponding (central) film thickness for the final loads (25, 30 and $40[N]$) on a grid with 257×257 nodes is 97.4, 95.1 and 91.2 $[nm]$ respectively. Some results are presented in Figure 5.12, which shows the evolution of the central film thickness as a function of time for the different load changes. For ease of comparison the results are scaled on the steady state central film thickness corresponding to the final load. This has been done to show how the amplitude of the oscillation is related to the magnitude of the load change. Note that this leads to curves that do not start at the same value at $t = 0$. In the simulations for all cases the starting conditions were exactly the same.

Because of the high viscosity in the center of the contact the main effect of the change of the mutual approach associated with the increase of the load is that the film thickness in the region surrounding the Hertzian contact circle decreases. This effect is propagated into the contact at the entrainment speed. This explains why the central film thickness initially changes very little, see Figure 5.12. The further evolution in time is again the combined effect of the oscillatory behavior of the mutual approach driven by the contact dynamics causing film changes in the outer region, which are propagated into the contact. The amplitude of the oscillations increases with load; at $t \approx 2[ms]$ it is about 5, 9 and $15[nm]$ for the cases $F_l = 25$, 30 and $40[N]$. Note that the amplitude of the film thickness oscillations induced by the load change are much larger than those observed for the case of the start up problem where only the speed changes. The period of the oscillation taken from the results is 0.68, 0.64 and $0.61[ms]$. The small difference in the period explains why the curves are initially in phase and gradually run out of phase. The value predicted by equation (5.8) is $0.68[ms]$ for all load cases. However, this value is valid for small amplitude oscillations; with increasing amplitude it will become less accurate and the difference

FIGURE 5.12: *Central film thickness ratio h_c/h_{cF_1} as a function of time for $F_N = 20[N]$ $\Omega = 5.13$ and $F_l = 25$, 30, and 40$[N]$, $\delta_t = 1\ [ms]$*

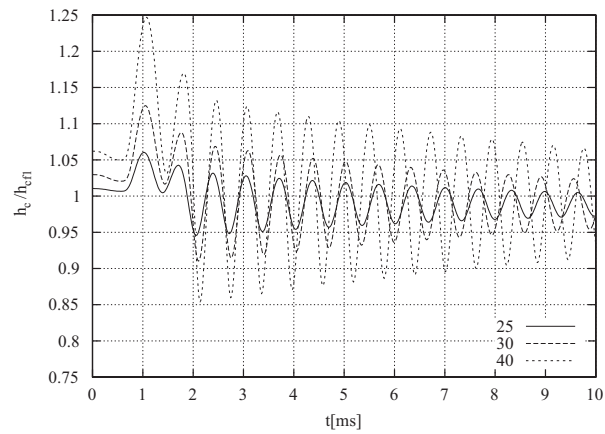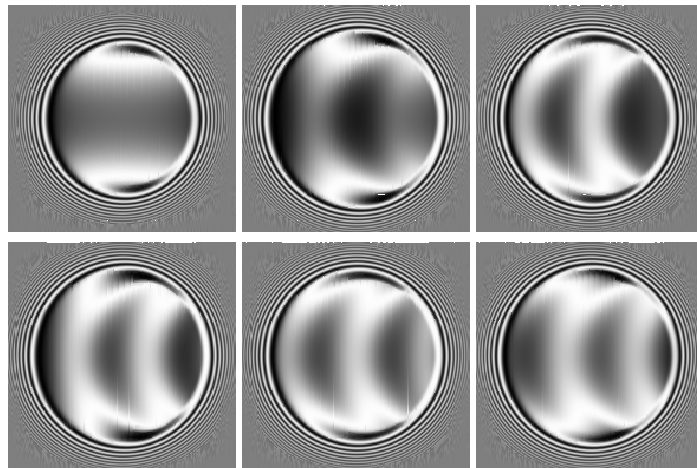FIGURE 5.13: *Pseudo-interferometry pictures of the dimensionless film thickness H at times $0, 1, 2, 3, 4$ and $5\ [ms]$ for $F_l = 30\ [N]$.*
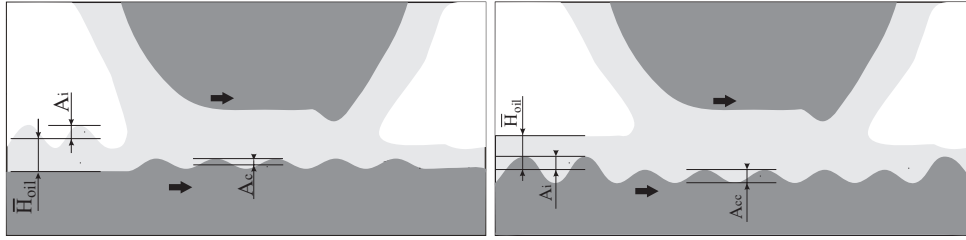
FIGURE 5.14: *Oscillatory lubricant supply: on a smooth surface (left); on a wavy surface (right)*

in the period observed for the different cases is possibly due to the non-linearity.

Finally, in Figure 5.13 pseudo-interferometry plots of the dimensionless film thickness are shown at different times. As expected, in these figures the propagated oscillations appear as crescent shapes. Also visible is the increase of the contact region, caused by the increase of load.

5.3 Surface modification in starved EHL contacts

Variations in the shape of the inlet layer cause film thickness modulations in the contact. In Chapter 2 it was shown how based on numerical simulations an engineering tool for the prediction of film thickness oscillations induced by roughness was developed. In Chapter 4 the film thickness response to steady inlet layer oscillations was described. In this section the results are extended to time varying situation. As H and θ appear together in the advective terms it is anticipated that a relation similar to 2.41 can be found.

Two situations of oscillatory lubricant supply can be distinguished. The first is an oscillatory layer on a perfectly smooth surface. The second is a constant layer on a non-smooth surface. The first case resembles the study for steady state case considered in section 4.2.4. The second case is a combination of the first case and a rough surface.

5.3.1 Oscillatory lubricant supply

The lubricant flow in EHL contacts is described by three effects represented in the Reynolds equation (2.20): Poiseuille terms (left hand side), wedge term $(\partial(\theta\overline{\rho}H)/\partial X)$ and squeeze term $(\partial(\theta\overline{\rho}H)/\partial T)$. In the shear flow terms, the gap height H and the fractional film content θ are playing a crucial role in the mechanism of amplitude reduction of the surface waviness problem, see Section 2.5.3. On the other hand, the film thickness inside an EHL contact and the local degree of starvation are determined by local transport phenomena. As a result, it is expected that a relation between the oscillation of the lubricant supply and the film thickness variation can be found in terms of a dependence on the EHL regime (inlet length), frequency of the
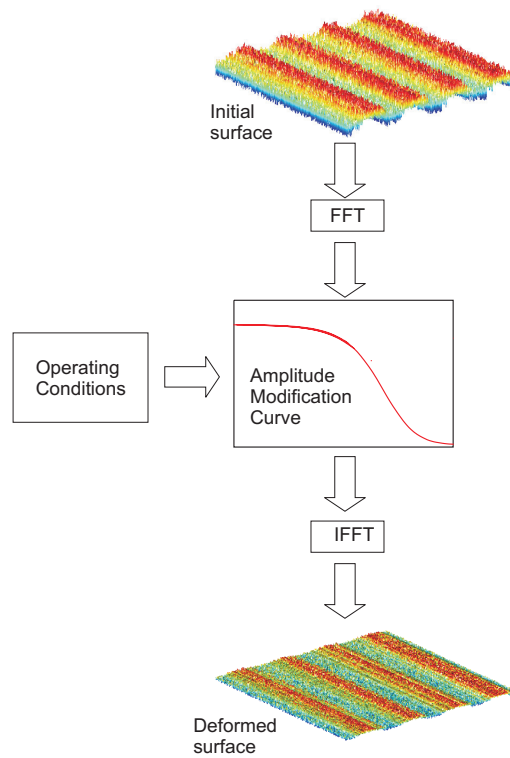
FIGURE 5.15: *Calculation of the amplitude modification under given operating conditions*
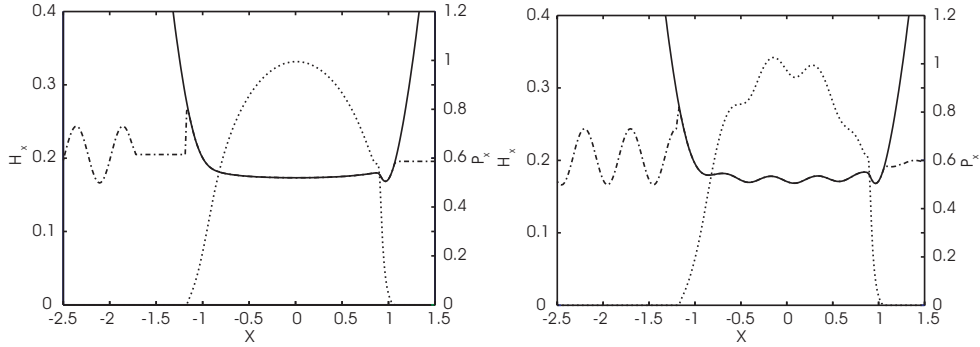
FIGURE 5.16: *Snapshots of the pressure and gap height profiles at* $Y = 0$ *for* $M = 20$, $L = 10$, $\overline{r}_c = 0.5$, $f_a = 0.2$, $\mathcal{W}_X = 0.5$

lubricant supply oscillations, and the degree of starvation . A starved transient EHL model was used to investigate these effects, as described in Chapter 3. Multigrid and multi-integration techniques are use to solve at each time step the dimensionless equations (2.20), (2.27), (2.29), (2.31), and (2.30) discretized on a rectangular domain $X \in [-2.5, 1.5]$, $Y \in [-2, 2]$, using an uniform grid with 129×129 nodes. For the Poiseuille terms of the Reynolds equation a central second order discretization scheme was used, while for the wedge and squeeze term, a narrow upstream second order ($NU2$) scheme was chosen, see Chapter 3). For the wavelengths considered here, the $NU2$ scheme provide sufficiently accurate results. This can be seen from the fact that there is no amplitude decay of the waves travelling through the contact.

The lubricant supply variations $H_{oil}(T)$ are given by:

$$H_{oil}(T) = \overline{H}_{oil} \left[1 - f_a sin \left(2\pi \frac{T}{\mathcal{W}_X} \right) \right] \qquad (5.14)$$

with $\overline{H}_{oil}$ the mean value of $H_{oil}(T)$, see Figure 5.14. The amplitude of the lubricant supply oscillations $A_i = f_a \times \overline{H}_{oil}$ is chosen within the order of $\overline{H}_{oil}$ and can not exceed this value ($f_a \in [0, 1]$).

Figures 5.16 shows snap shots of the solution for pressure distribution, gap height and lubricant film content along the running direction at $Y = 0$ for $M = 20$, $L = 10$, while the amount of oil from the inlet $\overline{H}_{oil} = 0.5H_{cff}$ oscillates with a (dimensionless) wavelength $\mathcal{W}_X = 0.5$ and an amplitude $A_i = 0.2\overline{H}_{oil}$. Oscillatory lubricant inflow has a clear influence on the pressure distribution and gap height. Both respond promptly to changes from the inlet, causing periodic film thickness variations with the amplitude A_c and a cyclic surface stress.

The corrected relative amplitude factor $\overline{\rho}A_c/A_i$ was studied for different EHL regimes (M and L), degrees of starvation ($\overline{r}$) and wavelengths ($\mathcal{W}_X$) as shown in Table 5.2. For small amplitudes $A_i \leq \overline{H}_{oil}$ the response of the EHL contact in terms of A_c is hardly dependent on the variation factor f_a, see Table 5.3. Therefore, the

M	L	$\mathcal{W}_X$	$\overline{r}$	f_a
		0.25	0.1	0.2
100	10	0.5	0.25	
100	5	1	0.5	
20	10	2	0.75	
20	5	4	1	
			1.5	

TABLE 5.2: *Input conditions for variable lubricant supply*

$f_a = A_i/H_m$	A_i/H_{cs}	$\overline{\rho}(p_H)A_c/A_i$
0.1	0.11	0.588
0.2	0.22	0.593
0.5	0.58	0.601
0.6	0.69	0.614
0.8	0.92	0.630
0.9	1.02	0.646

TABLE 5.3: *Linearity check for different values of f_a ($M = 100, L = 5, \overline{H}_{oil}/H_{cff} = 0.5, \mathcal{W}_X = 0.75$)*

simulations were performed fixing the initial amplitude A_i at $0.2 \times \overline{H}_{oil}$. The amplitude of the deformed gap height A_c was found monitoring the maxima and minima of this value over the time interval needed for a complete oscillation.

An analysis of the obtained results revealed that the factor $\overline{\rho}(p_H)A_c/A_i$ is limited to a maximum that is determined by the sensitivity of the starved EHL contact to the variation of the oil supply. Exploiting the results of the steady state starved contact this maximum can be estimated from (2.39) by differentiation as follows:

$$(I\!R)_{max} = \frac{\partial I\!R}{\partial r} = \frac{1}{\sqrt[\gamma]{1+r^\gamma}} - \frac{r^\gamma}{(1+r^\gamma)\sqrt[\gamma]{1+r^\gamma}} \tag{5.15}$$

with $I\!R$ given by

$$I\!R = \frac{H_{cs}}{H_{cff}} = \frac{r}{\sqrt[\gamma]{1+r^\gamma}} \tag{5.16}$$

For a small value of $I\!R$ any variation in the lubricant supply directly leads to a variation of the central film thickness.

$$\left(\frac{\overline{\rho}A_c}{A_i}\right)_{I\!R \to 0} = \lim_{r \to 0}\left(\frac{\partial I\!R}{\partial r}\right) = 1 \tag{5.17}$$

For $I\!R \approx 1$ the contact can be considered fully flooded, and variations of the lubricant supply are cancelled before they can affect the central gap height.

$$\left(\frac{\overline{\rho}A_c}{A_i}\right)_{\mathbb{R}=1} = \lim_{r \to \infty}\left(\frac{\partial \mathbb{R}}{\partial r}\right) = 0 \tag{5.18}$$

Depending on the EHL regime given by the operating conditions (M and L), a certain pressure field dictates the needed inlet length ($\overline{S}_{ff}$). If the inlet meniscus is way upstream, fully flooded conditions can be assumed and no changes in the gap height are recorded. A short pressure field makes starved lubrication unlikely, but in combination with a high degree of starvation can lead to oscillations of the central film thickness. That happens because the high pressure gradient causes the viscosity to rise to a level that shear flow dominates and the variations of the lubricant supply are directly transferred to the gap height variations. For large pressure fields the viscosity increases at a slower rate (with a smaller gradient) and the side flow (lubricant ejection, see [18]) cancel any variation of the lubricant supply.

For wavelengths larger than the contact width, the response of the EHL contact is according to the minima and the maxima of the lubricant supply, i.e. the contact "floats" on the oil layer. As the distance between the waves of lubricant is shorter the variation of the inlet layer leads to local variations of film thickness inside the contact.

Combining the effect of the inlet length $\overline{S}_{ff}$, see (2.40), wavelength ($\mathcal{W}_X$) and degree of starvation ($\mathbb{R}$) the following dimensionless parameter is proposed as follows:

$$C_O = (\mathbb{R})_{max}\frac{\mathcal{W}_X^{3/2}}{\overline{S}_{ff} \cdot \mathbb{R}^2} \tag{5.19}$$

Please note that the dimensionless parameter C_O represent the operating conditions and that is inversely proportional with the degree of starvation. In Figure 5.17 (top) the numerical results are shown as a function of this parameter (5.19).

For values of C_O below 1 the lubricant waves are completely flattened before they can produce any oscillations on the central film thickness. For values of C_O above 10 the lubricant waves are transmitted through the contact generating central film thickness oscillations with the same amplitude. A family of curves that describes the distribution of the computed values on the graph from Figure 5.17 (top) can be written as

$$\frac{A_c}{A_i} = \frac{1}{\overline{\rho}}\frac{(\mathbb{R})_{max}}{1 + 2/C_O + 40/C_O^2} \tag{5.20}$$

Figure 5.17 (bottom) shows the predictions obtained with the family of curves (5.20).

The points from Figure 5.17 can be gathered into a single curve when a dimensionless parameter directly proportional with the degree of starvation $\mathbb{R} = H_{cs}/H_{cff}$ is
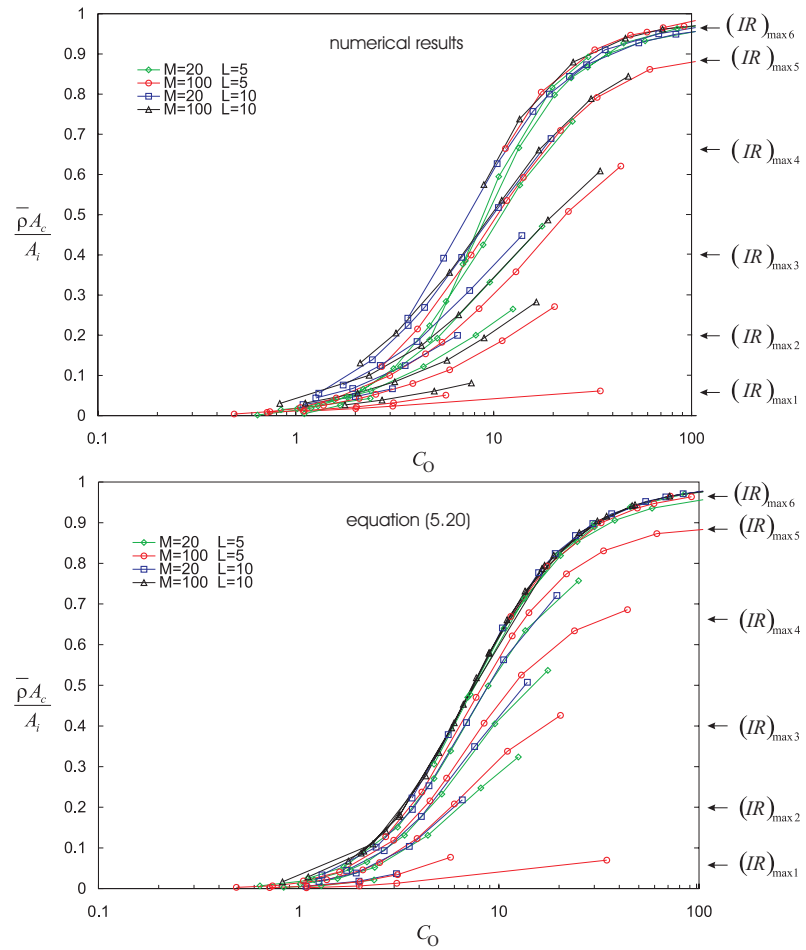
FIGURE 5.17: *Surface modification for oscillating lubricant supply: numerical results (top); surface modification curves for each degree of starvation as given in Table 5.2 (bottom)*

used, but the form presented above is preferred because it can be explained better in terms of the physical phenomena taking place around the contact.

5.3.2 Oil layers following the surface waviness

In earlier studies, [76], it was shown that the effect of the surface micro-geometry under starved condition (uniform oil layer) can be described by a dimensionless parameter $\overline{\nabla}$ that includes the degree of starvation, see (2.41). An amplitude reduction curve was found, (2.42), predicting how the amplitude of a harmonic wave is reduced in different operating conditions and degrees of starvation.

Analyzing the amplitude modification curves (5.20) and (2.42) it can be noticed that the factors $\overline{\rho}A_c/A_i$ and A_d/A_i are proportional to the dimensionless parameter C_O and inverse proportional to $\overline{\nabla}$. As first approximation it can be assumed that the surface waviness and the variable lubricant supply add up as follows:

$$A_{d+c} = A_d + A_c \tag{5.21}$$

To verify this hypothesis, the starved transient EHL model presented in Chapter 3 was tested on a grid with 129×129 nodes, equally spaced. The surface waviness was included according with (5.22), moving through the contact with the velocity u_m while the lubricant supply is controlled by (5.14).

$$\mathcal{R}(X, Y, T) = A_i \cdot sin\left(\frac{2\pi\left(X - (X_0)\right)}{\mathcal{W}_X}\right) \tag{5.22}$$

The initial amplitude of the waviness, A_i, is equal or smaller than the average oil layer thickness $\overline{H}_{oil}$ as follows

$$A_i = f_a \times \overline{H}_{oil} \times 10^{-10\left[max\left(0, \frac{X-X_0}{\mathcal{W}_X}\right)\right]^2} \tag{5.23}$$

The exponential term in (5.23) makes the waviness to effectively start at $X_0 = X_a + T$ without introducing any discontinuous derivatives, see [74]. As the lubricant follows the surface waviness, the two waves are in phase and have the same initial amplitude ($A_i = \overline{H}_{oil} \times f_a$), with maxima and minima facing each other (Figure 5.14). The lubrication regimes, amount of lubricant and the wavelengths are chosen as shown in Table 5.2. The amplitude of the deformed gap height A_{d+c} was found by averaging the maxima and minima of this value over the time interval needed for a complete oscillation.

Figure 5.18 shows the numerical results and the prediction obtained adding up the predictions of (2.41) and (5.20). The results are plotted as function of the dimensionless parameter $\overline{\nabla}$. The evolution of the amplitude modification factor A_{d+c}/A_i for different combinations of EHL regimes (M, L), lubricant supplies ($\overline{r} = \overline{H}_{oil}/H_{cff}$) and frequencies ($1/\mathcal{W}_X$) shows that for an increasing $\overline{\nabla}$ the initial surface waviness
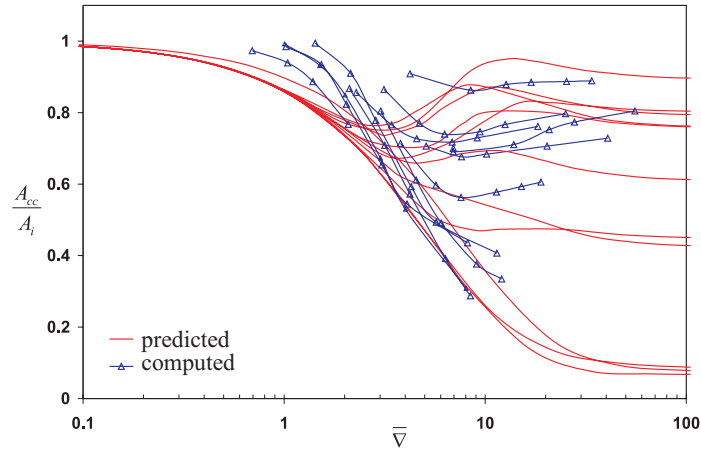
FIGURE 5.18: *Numerical results and predictions given by (5.21). The different curves represent combinations of degrees of starvation $\overline{r}$, operating conditions parameters M and L and wavelengths W_X .*

amplitude is reduced until a minimum is reached. This minimum corresponds to the intersection points of curve (2.42) with the family of curves (5.19). After reaching this minimum, A_{d+c}/A_i increases to the value prescribed by (5.15). For fully flooded conditions the effect of lubricant oscillations is nil, surface waviness dictates the value of A_{d+c}/A_i. For thin layers of lubricant the amplitude factor A_{d+c}/A_i is close to unity for values of $\overline{\nabla}$ smaller than 1 or bigger than 10, and decrease slightly below unity for $1 < \overline{\nabla} < 10$.

For the points situated in the region $1 < \overline{\nabla} < 10$ the difference between numerical calculations and the prediction given by (5.21) is about 20% and less than 10% for the other points. Even so, the main trend of the prediction curve is acceptably approximated for engineering purposes.

Test oil	Temperature [$^{\circ}C$]	Load [N]	Rolling speed [m/s]	measured h_{cff} [nm]
PAO 8	25	20	0.6	62
			1	104
PAO 100	25	20	0.05	124
			0.1	190

TABLE 5.4: *Test conditions*

5.4   Repeated overrolling

In Chapter 4 the thickness of the oil layer at the inlet of the contact was quantified across the running track (of the disc) at different rolling speeds. In this section, the response of the gap height in the center of the contact to the lubricant supply from the median line or the running track is monitored as function of number of revolutions. The results can be regarded as qualitative validation of Chevalier's [10] starved lubrication model. Unfortunately, full quantitative validation is not possible due to the limitation of the oil layer measurement technique, i.e. the maximum thickness that can be measured and the location of the measurement points (on the disc only).

Chevalier [10] and Damiens [18] have evaluated numerically the effect of repeated overrollings on the gap height decay as a function of number of revolutions for different rolling speeds. Below a similar experiment is presented for severely starved conditions with a low viscosity oil, PAO 8, and a high viscosity oil, PAO 100. The oil was "uniformly" distributed along the running track and the evolution of oil in the inlet and in the contact center was monitored as a function of the number of revolutions at different velocities. Table 5.4 presents the operation conditions and the corresponding film thickness for fully flooded conditions, measured at the contact center. The test velocities for each oil were chosen such that the gas bubble, formed behind the contact, broke through the outlet meniscus and two side levees were formed in the inlet after one revolution (see Figure 4.23).

Some results are presented in Figure 5.19 in plots of central film thickness ratio for starved and fully flooded lubrication conditions as a function of number of revolutions for each oil at two speeds. For the low viscosity oil PAO 8, a decay of the central film thickness can be noticed with an increasing number of overrollings. However, for the high viscosity PAO 100 oil such a decay was recorded only for a relatively low speed (0.05[m/s]). For a speed twice as big $0.1[m/s]$ the film thickness remains relatively constant. A stagnation of film thickness decay can also be observed for PAO 8, but only after about 50 revolutions.

Such a stagnation indicates a state of equilibrium regarding the lubrication, namely the oil layer supplying the contact establishes its shape and thickness and with it the response of the EHL contact. This is illustrated in Figure 5.20 where the thickness of the oil layer at the inlet and the gap height in the contact centre is plotted on a linear
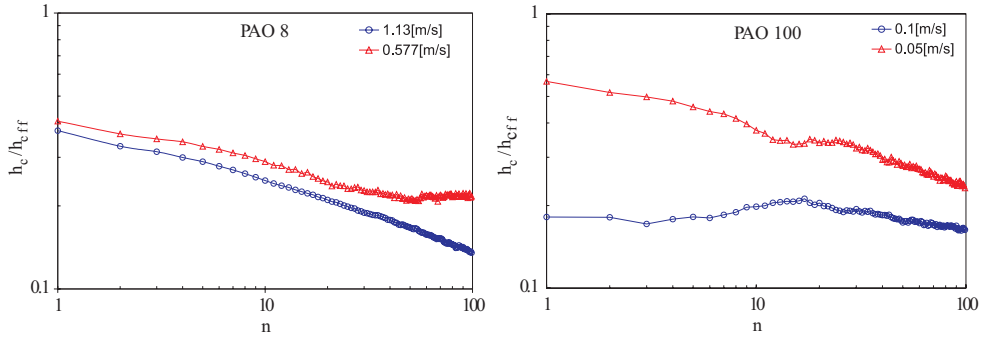
FIGURE 5.19: *Film thickness ratio for starved and fully flooded lubrication conditions as function of number of overrollings for PAO 8and PAO 100 for two speeds*

scale for each speed. On these plots it can be noticed that the central film thickness follows the changes from the inlet layer. It is clear that the potential of the EHL contact strongly depends on the oil layer level from the inlet.

Neglecting the effect of replenishment and considering a uniform oil layer across the inflow direction, Damiens used as approximation for the $n^{th} + 1$ overrolling the following relation for the relative oil film thickness r

$$r_{n+1} = \frac{r_n}{\sqrt[\gamma]{1 + (r_n)^\gamma}} \tag{5.24}$$

For more than two overrollings, the amount of lubricant at the inlet of the contact at the nth overrolling is given by

$$r_n = \frac{1}{\sqrt[\gamma]{n - 1}} \tag{5.25}$$

Chevalier predicted numerically the central film thickness decay for n consecutive overrollings as follows

$$I\!\!R(n) = \frac{1}{\sqrt[\gamma]{1/r_o^\gamma + n}}, \qquad \lim_{r_o \to 0} I\!\!R(n) = n^{-1/\gamma} \tag{5.26}$$

To some extent, this is also the behavior shown in Figure 5.19.

5.5   Oil replenishment

In their models Chevalier and Damiens neglected the replenishment effect. However, the lubricant distribution in the neighborhood of the contact is driven by the surface tension of lubricant, gravity force, centrifugal force and strongly depends on the time elapsed between consecutive overrollings. These effects were investigated in detail by Jacod [40]. He showed that for the flow 'around the contact' the surface tension is the main components that drive the reflow mechanism.
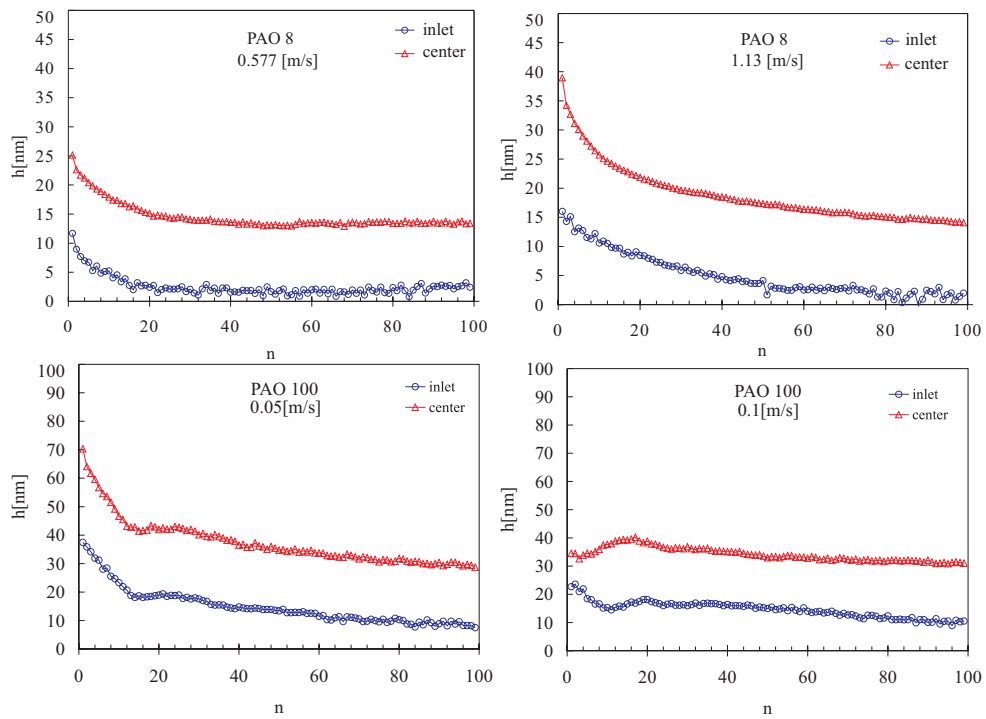
FIGURE 5.20: *Film thickness at inlet and center of contact as function of number of overrollings*

The experimental results presented in Chapter 4 showed that for starved lubrication the contact sides remain well lubricated due to the combination of side flow and replenishment action. For a single EHL contact this implies that the inlet conditions are strongly dependent on the replenishment rate and the time elapsed between consecutive overrolings.

Below, the replenishment rate after a sudden stop is investigated, following the procedure presented in Chapter 3. For these experiments a thin (low viscosity) oil (*TT 9*) was used because the changes in the wetting angle (oil profile) are visible within a few minutes. An amount of $0.6[\mu l]$ of oil was injected on the running track of the disc. With a load of $20[N]$ a contact circle with a diameter of $0.268[mm]$ is obtained between the steel ball and the glass disc. The disc was driven at a speed at which two side levees (ridges) of oil were visible (see Figure 4.23) for several minutes. Once the lubrication on the running track became steady state, the disc was stopped and the lubricant at a distance of $500[\mu m]$ from the contact center was measured. Figure 5.21 shows the measured profile from the inlet immediately after the sudden stop (0[s]), after 120[s] and after 240[s]. As expected, the results show that the oil flows back to the running track when enough time elapses. On the plot it can be seen that the oil from the sides slowly fills the empty space between the two levees. The same tendency can be seen in Figure 5.22 with a better overview. Please remember that the images from Figure 5.22 are recorded at a different time than the measurements from Figure 5.21. For the ridge from the right hand side, a height of about $1700[nm]$ was found counting the orders one by one, starting from order 3 ($540[nm]$ spacer layer). Since, a zero film reference is not available for the data acquired at $120[s]$ and $240[s]$, the fringe order was counted from the maximum height of the data acquired at time $0[s]$. This means that the measurements can be wrong with one or two fringe orders.

FIGURE 5.21: *Replenishment on the running track in the inlet region at* 0, 120 *and* 240 *seconds from a sudden stop*
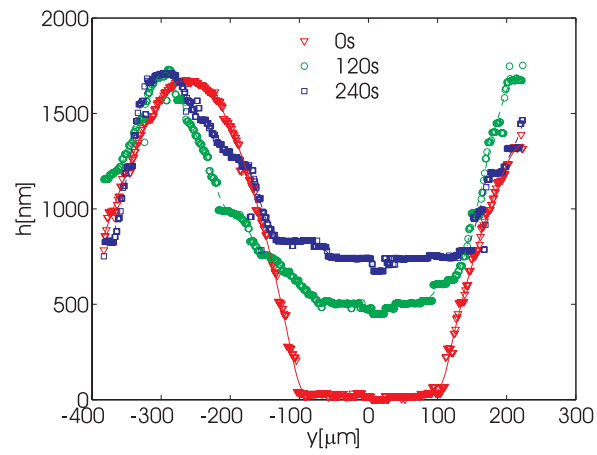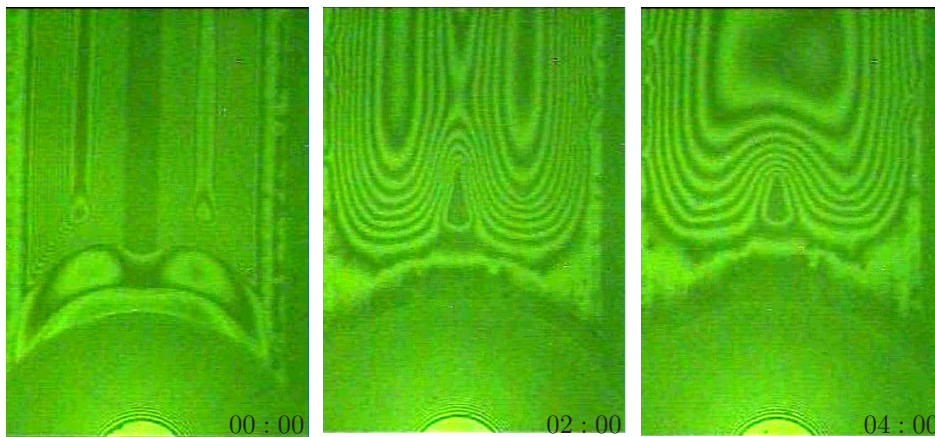

FIGURE 5.22: *Images recorded at* 0, 2 *and* 4 *minutes from a sudden stop (movie available)*

CONCLUSIONS & RECOMMENDATIONS

6

6.1 Conclusions

In this thesis various aspects of lubricant starvation on the performance of the elasto-hydrodynamically lubricated contacts have been studied theoretically and experimentally. The work was motivated by the urgent need of accurate prediction for the highly loaded contacts under poor lubrication conditions. The results are relevant for oil lubrication but also for grease lubricated contacts in the situation where after the first overrollings the grease has been pushed aside the running track and acts as a reservoir from which base oil is supplied for film formation.

Based on the work of Chevalier [10], Venner [76] and Damiens [18] the effect of steady state and time varying lubrication conditions were studied. By means of numerical simulations the gap height oscillations inside the contact induced by harmonic surface waviness have been investigated in relation to the thickness of the supplied layer of oil. It was shown that a variable lubricant supply modifies the local gap height inside the contact. It is revealed that this phenomena is governed by a unifying mechanism that can be characterized by a single non-dimensional parameter reflecting the operating conditions. A simple engineering formula has been derived to predict the amplitude of the gap height oscillations induced by waviness and by the lubricant layer oscillations. When applied to each Fourier component of a rough surface or lubricant layer variation the resulting formulas can be used to obtain a prediction of the local gap height inside the contact under given operating conditions. Such tools are essential first steps towards surface and lubricant supply optimization.

Another cause for local gap height variations inside the lubricated contact is the time variation of the operating conditions. In this thesis using a dynamic EHL model the effects of start-up on the gap height oscillations in the contact were investigated in relation to the inertia effects, stiffness of the loading system and the degree of starvation. It was shown that the gap height oscillations observed experimentally are mainly determined by the elastic effects, their frequency being accurately predicted from a simple analysis. The damping of these oscillations was found to vary with the degree of starvation, namely with an increasing degree of starvation the damping is

reduced.

Implementation of "tailor-made" geometries into the classic EHL model was also attempted. The geometries of two classical rolling bearings was studied and a comparison with existing analytical approximations was made. This approach is still in its infancy and requires more attention in the future research.

In the past decades optical interferometry has established itself as an outstanding method to study EHL contacts experimentally. Film thicknesses can be measured accurately down to a few nanometers under controlled conditions. With the final aim to provide quantitative experimental validation for starved lubricated contacts, the method has been used to validate the predictions of a standard EHL model under fully flooded conditions. Results for circular and elliptic contacts were presented. It has been shown that the models accurately predict both the level of the film thickness as well as the local variations inside the contact region such as the changes of the width of the side lobes with changing operating conditions. In addition measurements have been done on starved lubricated contacts. One of the problems here is the control of the degree of starvation. In the starved lubrication model the inlet layer thickness supplied to the contact is assumed to be known whereas in reality it is not. Therefore to validate the model it is essential that a measurement method for the thickness and shape of the oil layer entering the contact is developed. In this thesis it has been shown that for sufficiently thin layers this can be done using optical interferometry exploiting the fact that light is also reflected on the oil-air interface. Although the technique needs to be developed further the first results are encouraging.

6.2 Recommendations for future research

The results presented for the effect of lubricant starvation on surface deformation can directly be used in a practical design environment for surface optimization. In addition to the surface optimization it is a challenge to consider lubricant supply optimization. Actively bringing the lubricant where is mostly needed would be a major breakthrough in lubrication technology.

Regarding the experimental work further experiments for narrow elliptic contacts using rollers with a hardness comparable to bearing surfaces are recommended. This would provide further insight in the validity of the fully flooded models in relation to the ellipticity of the contact. For the validation of the starved contact models further development of the layer measurement procedure presented in this thesis is needed. Thorough validation of the model predictions is crucial to stimulate the use of the presented results from the theoretical research in practice.

As mentioned before the trends in design are towards smaller and smaller films. Even though it has been shown that up to very small film thickness levels the models can predict the film thickness quite accurately the models can not achieve the limit

of locally zero film or mixed lubrication. In the literature several attempts have been reported to extend the current models to account for local contact. However, it can easily be shown that many of these approaches yield artificial and non-physical results. In the theoretical research attention should be given to a physically acceptable way to model the transition from lubricated to dry contact.

Finally, additional ways to protect the surface against metallic contact may be considered. In experimental research it has been found that in some cases in grease lubricated contacts thickener rich layers are formed on the surface, on top of which the lubricant film is formed. Such layers can play an important role in the extremely thin film regime. In addition to ensuring surface separations such layers can have a cushioning effect on pressure oscillations induced by surface features and thereby help to reduce subsurface stresses. The challenge is to combine experimental and theoretical research such that the required qualities of such layers can be investigated.

REFERENCES

[1] Bair S., Khonsari M., Winer W.O., 1998, "High−pressure rheology of lubricants and limitation of the Reynolds equation", *Tribology International*, vol. 31, pp. 573÷586.

[2] Bair, S., Winer W.O., 2000, "The pressure−viscosity coefficient at Hertzian presure and its relation to concentrated contact traction", *Proceedings of* 26th *Leeds−Lyon Symposium on Tribology*, vol. 45, pp. 433÷443.

[3] Barus C., 1893, "Isothermals, isopietics and isometrics relative to viscosity", *American Journal of Science*, vol. 45, pp. 87÷96.

[4] Bayada G., Chambat M., El Alaoui M., 1990, "Variational formulation and Finite Element Algorithms for cavitaiton problems", *ASME, Journal of Tribology*, vol. 112 ,pp. 398÷403.

[5] Cann, P.M. and Spikes H.A., 1996, "The developement of a Spacer Layer Imaging Method (SLIM) for mapping elastohydrodynamic contacts", *Tribology Trasactions*, vol. 39, Issue 4, pp. 915÷921.

[6] Cann, P.M., 1996, "Starvation and reflow in a grease−lubricated elastohydrodynamic contact", *Tribology Transactions*, vol. 39, Issue 3, pp. 698÷704.

[7] Cann, P.M., 1999, "Starved Grease lubrication of rolling contacts", *Tribology Transactions*, vol. 42, Issue 4, pp. 867÷873.

[8] Cameron, A. and Gohar R., 1966, "Theoretical and experiemental studies of the oil film in lubricated point contacts", *Proceedings of the Royal Society*, Series A, vol. 291, pp. 520÷536.

[9] Chevalier, F., 1996, "Modélisation des conditions d'alimentation dans les contactes élastohydrodynamiques ponctuels", *PhD Thesis*, I.N.S.A. de Lyon, France.

[10] Chevalier, F., Lubrecht A.A., Cann P.M.E. et al., 1998, "Film thickness in starved EHL point contacts", *ASME, Journal of Tribology*, vol. 120 ,pp. 126÷133.

[11] Chittenden, R.J., Dowson, D., Dunn, J.F. and Taylor, C.M., 1985, "A theoretical analysis of the isothermal elastohydrodynamic lubrication of concentrated contacts. Part I: Direction of lubricant entrainment coincident with the major axis of the Hertzian contact ellipse", *Proceedings of the Royal Society of London*, Series A, Mathematical and Physical Sciences, vol. 397, pp. 245÷269.

[12] Chiu, Y.P., 1974, "An analysis and prediction of lubricant film starvation in rolling contact systems", *ASLE Trasactions*, vol. 17, pp. 22÷35.

[13] Cretu, S.S., 2002, "Mecanica contactului", *Editura Gh. Asachi Iasi*, vol. 2, ISBN 9738292018.

[14] Dowson, D, Higginson G.R., 1959, "A numerical solution to the elastohydrodynamic problem", Journal of Mechanical Engineering Science, vol. 1, pp. 6÷15.

[15] Dowson, D. and Higginson, G.R., 1966 "Elastohydrodynamic lubrication, the fundamentals of roller and gear lubrication", *Pergamon Press*, Oxford, Great Britain.

[16] Dowson, D, Higginson G.R., 1977, "Elastohydrodynamic lubrication", *Pergamon Press*, SI edition, ISBN 0080213030.

[17] Dowson, D., 1998, "History of Tribology", *Professional Engineering Publishing*, second edition, ISBN 186058070.

[18] Damiens, B., 2003, "Modélisation de la lubrification sous-alimentee dans les contacts élastohydrodynamiques elleptiques", PhD Thesis, I.N.S.A. de Lyon, France.

[19] Elrod H.G., 1981, "A cavitation algorithm", *ASME, Journal of Tribology*, vol. 103 No. 3, pp. 350÷354.

[20] Evans H.P., Snidle R.W., 1983, "Analysis of elastohydrodynamic lubrication of elliptic contacts with pure rolling along the major axis", *Proc. Instn. Mech. Engrs.*, vol. 197 C, pp. 209÷211.

[21] Evans H.P., Snidle R.W., 1992, "Wildhaber−Novikov circular Arc Gear: elastohydrodanamics", *ASME, Journal of Tribology*, vol. 115, No. 3, pp. 487÷492.

[22] Foord,R.P. , 1970, "Optical elastohydrodynamics", *Proc. Inst. of Mech.Engrs.*, vol. 184, pp. 487÷505.

[23] Glovnea, R. P., Spikes, H. A., 2000, "The influence of lubricant on film collapse rate in high pressure thin film behavior during sudden halting of motion", *STLE Tribology Transactions*, pp. 731÷739.

[24] Glovnea, R. P., and Spikes, H. A., 2001, "Elastohydrodynamic film formation at the start up of the motion", *Proc. Inst. Mech. Eng., Part J: J. of Eng. Tribol.*, vol. 215, pp. 125÷138.

[25] Glovnea, R. P., and Spikes, H. A., 2001, "Elastohydrodynamic film collapse during rapid decelaration. Part I: Experimental results", *ASME Journal of Tribology*, vol. 123, pp. 254÷261.

[26] Glovnea, R. P., and Spikes, H. A., 2001, "Elastohydrodynamic film collapse during rapid deceleration. Part II: Theoretical analysis and comparison of theory to experiment", *ASME Journal of Tribology*, vol. 123, pp. 262÷267.

[27] Greenwood,J.A., 1990, "Elastohydrodynamic film thickness in point contacts for arbitrary entraining angle", *Proc. Inst. of Mech. Engrs.*, part E., vol. 204, pp. 417÷420.

[28] Grubin, A.N. Vinogradova I.E., Ketova Kh.F., 1949, "Investigation of the contact of machine components", *Central Scientific Research Institute for Technology and Mechanical Engineering*, Book 30.

[29] Hamrock, B.J and Dowson, D., 1976, "Isothermal elastohydrodynamic lubrication of point contact, Part I: Theoretical formulation", *Transaction of the ASME, Journal of Lubrication Technology*, vol. 98, pp. 223÷229.

[30] Hamrock, B.J and Dowson, D., 1976, "Isothermal elastohydrodynamic lubrication of point contact, Part II: Ellipticity parameter results", *Transaction of the ASME, Journal of Lubrication Technology*, vol. 98, pp. 375÷383.

[31] Hamrock, B.J and Dowson, D., 1976, "Isothermal elastohydrodynamic lubrication of point contact. Part III: Fully flooded results", *Transaction of the ASME, Journal of Lubrication Technology*, vol. 99, pp. 264÷276.

[32] Harris, T.A., 2001, "Rolling bearing analysis - fourth edition", ISBN 0471354570.

[33] Hertz, H., 1896, "Miscellaneous papers", *Macmillan, London*.

[34] Holmes, M. J. A., Evans, H. P., and Snidle, R. W., 2002, "Comparison of transient EHL calculations with a start up experiment", *Proceedings of* 29th *Leeds−Lyon Symposium on Tribology*, Elseviers Tribology Series, D. Dowson et al., vol. 41, pp. 79÷89.

[35] Holmes, M. J. A., Evans, H. P., and Snidle, R. W., 2002, "Comparison of transient EHL calculations with a shut-down experiment", *Proceedings of* $29^{t}h$ *Leeds−Lyon Symposium on Tribology*, Elseviers Tribology Series, D. Dowson et al., eds., 41, pp. 91÷99.

[36] Hook, C.J, 1998, "Surface roughness modification in elastohydrodynamic line contacts operating in elastic piezoviscous regime", *Proc. Instn. Mech. Engrs.*, vol. 212, Part J2, pp. 145÷163.

[37] Hook, C.J, 1999, "Surface roughness modification in elastohydrodynamic line contacts - effects of roughness wavelength, orientation and operating conditions", *Proceedings of the* 26th *Leeds−Lyon Symposium on Tribology*, Elsevier, Tribology Series, vol. 36, pp. 193÷202.

[38] Hook, C.J, 2000, "Surface roughness attenuation in line and point contacts", *Proc. Instn. Mech. Engrs.*, vol. 214, Part J5, pp. 439÷444.

[39] Ioannides, E., Harris, T.A., 1985, "A new fatigue life model for rolling bearings", *ASME, Journal of Tribology, vol. 107, pp. 367÷378.*

[40] Jacod, B., Pubilier F., Cann P.M.E., Lubrecht A.A., 1998, "An analysis of track replenishment mechanisms in the starved regime", *Proceedings of the* $25^{t}h$ *Leeds−Lyon Symposium*, Tribology Series 36, Elsevier, pp. 483÷492.

[41] Jacod, B., 2002, "Friction in Elasto−Hydrodynamic Lubrication", PhD Thesis, University of Twente, Enschede, The Netherlands, ISBN 90 36517826.

[42] Jacobson, B. and Hamrock, B.J., 1984, "Non−Newtonian fluid model incorporated in elastohydrodynamic lubrication of rectangular contacts", *Transaction of the ASME, Journal of Tribology*, vol. 106, pp. 275÷284.

[43] Jakobsson, B. and Floberg, L., 1957, "The finite journal bearing, considering vaporization", *Trans. Chalmers Univ. Tech. Göteborg*, vol. 190.

[44] Johnson K.L., Tevaarwerk, J.L., 1977, "Shear behaviour of elastohydrodynamic oil films", *Proc. Roy. Soc. London*, series A. vol. 356, Issue 12, pp. 215÷236.

[45] Johnson, K.L., 1985, "Contact mechanics", *Cambridge University Press*, ISBN 0521347963.

[46] Johnson, R. Wayte R., Spikes H.A., 1991, "The measurement and study of very thin lubricant films in concentrated contacts", *STLE Tribology Transactions*, vol. 34, pp. 187÷194.

[47] Kaneta, M., Sakai, T., and Nishikawa, H., 1992 "Optical interferometric observations of the bump on point contact EHL", *ASME, Journal of Tribology*, vol. 114, pp. 779÷784

[48] Lubrecht A.A., 1987, "The numerical simulation of the elastohydrodynamically lubricated line and point contact problem using multigrid techniques" PhD Thesis, University of Twente, Enschede, The Netherlands. ISBN 9090015833.

[49] Lubrecht A.A., Venner, C.H., 1999, "Elastohydrodynamic lubrication of rough surfaces", *Proc. Instn. Mech. Engrs.*, vol. 213, Part J5, pp. 397÷404.

[50] Lundberg, G., Palmgren A., 1947, "Dynamic capacity of rolling bearings", *Acta Politechnica, Mechanical Engineering Series*, Royal Swidish Academy of Engineering Sciences vol. 1, pp. 7.

[51] Lundberg, G., Palmgren A., 1952, "Dynamic capacity of rolling bearings", (*Acta Politechnica, Mechanical Engineering Series*, Royal Swidish Academy of Engineering Sciences vol. 2, pp. 96.

[52] Martin, H.M., 1916, "Lubrication of gear teeth", *Engineering*, London, vol. 102, pp. 199.

[53] Masen, M., Venner, C.H., Lugt P.M. and Tripp, J.H., 2002, "Effects of surface micro-geometry on the lifft-off speed of an EHL contact", *Tribology Transactions*, vol. 45, Part 1, pp. 21÷30.

[54] Moes, H., 1992, "Optimum similarity analisis, an application to elastohydrodynamic lubrication", *Wear*, vol. 159, Part 1, pp. 57÷66.

[55] Moes, H., 2000, "Lubrication and beyond", *UT lecture notes*, code 115531.

[56] Newmark, N. M., 1959, "A method of computation for structural dynamics", *J. Eng. Mech. Div.*, vol. 85, pp. 76÷94.

[57] Nijenbanning, G., Venner, C.H., Moes H., 1994, "Film thickness in elastohydrodynamically lubricated elliptic contacts", *Wear*, vol. 176, pp. 217÷229.

[58] Odyck D.E.A., 2001, "Stokes flow in thin films", PhD Thesis, University of Twente, Enschede, The Nethrlands, ISBN 9090148205.

[59] Pemberton, J. and Cameron A., 1976, "A mechanism of fluid replenishment in elastohydrodyamic contacts", *Wear*, vol. 37, pp. 185÷190.

[60] Petrusevich, A.I., 1951, "Fundamental conclusions from the contact hydrodynamic theory of lubrication", *Izv. Akad. Hauk SSR (ONT)*, vol. 2, pp. 209÷223.

[61] Popovici, G., Venner C.H., Lugt P.M., 2004, "Effects of load system dynamics on the film thickness in EHL contacts During start up" *ASME Journal of Tribology*, vol. 126, pp. 258÷266.

[62] Quiang,L., 2002, "Friction in mixed and elastohydrodynamic lubricated contacts including thermal effects", PhD Thesis, University of Twente, Enschede, The Nethrlands, ISBN 9036517966.

[63] Reyonlds, O., 1886, "On the theory of lubrication and its application to Mr. Beauchamps Tower's experiments, including experimental determination of the viscosity of olive oil", *Phil. Trans.*, vol. 177, pp. 157÷234.

[64] Reusner H., 1987, "The logarithmic profile - the key to superior performance of cyclindrical taper and roller bearings", *Ball Bearing Journal*, vol. 230, SKF(June 1987), pp. 2÷10.

[65] Roelands, C.J.A., 1966, "Corelation aspects of the viscoisty-temperature-pressure relationship of lubrication oils", PhD Thesis, Techinschwe Hogeschool Delft, The Netherlands.

[66] Zhao, J., Sadeghi, F., and Hoeprich M.H., 2001, "Analysis of EHL circular contact start up. Part I: Mixed contact model with pressure and film thickness results", *ASME Journal of Tribology*, vol. 123, pp. 67÷74.

[67] Sharif, K.J, Barragan de Ling, F.d.M., Alanou, M.P., Evans, H.P., 2001, "Film thickness predictions for elastohydrodynamic elliptical contacts over a wide range of radius ratios with considereation of side starvation", *Proc. Instn. mech. Engrs., vol. 214, part J*, pp. 63÷78.

[68] Tower, B., 1883, "First report on friction experiments", *Proc. Instn. mech. Engrs.*, November 1883, pp. 632÷659.

[69] Tower, B., 1885, "Second report on friction experiments", *Proc. Instn. mech. Engrs.*, January 1885, pp. 58÷70.

[70] Venner, C.H., 1991, "Multilevel solution of the EHL line and point contact problem", PhD Thesis, University of Twente, Enschede, The Netherlands, ISBN 9090039740.

[71] Venner, C.H. and ten Napel, W.E., 1997, "Multilevel solution of the elastohydrodynamically lubricated circular contact problems. Part I: Theory and numerical algorithm", *Wear*, vol. 152, pp. 351÷367.

[72] Venner, C.H. and ten Napel, W.E., 1997, "Multilevel solution of the elastohydrodynamically lubricated circular contact problems. Part II: Smooth surface results", *Wear*, vol. 152, pp. 396÷381.

[73] Venner, C.H., 1997, "Amplitude reduction of waviness in transient EHL line contacts", *Proceedings of the 23th Leeds−Lyon Symposium on Tribology*, Elsevier, Tribology Series, vol. 32, pp. $103 - 112$.

[74] Venner, C.H., Morales−Espejel, G.E., 1999, "Amplitude reduction of small-amplitude waviness in transient elastohydrodynamically lubricated line contacts", *Proc. Instn. Mech. Engrs.*, vol. 213, Part J, pp. 487÷504.

[75] Venner, C.H., 2000, "Multilevel methods in lubrication", *Elsevier*, Tribology Series, vol. 37, ISBN 0444505032.

[76] Venner, C.H., Berger, G., 2004, "Waviness deformation in starved EHL circular contacts", Transaction of ASME, Journal of Tribology, vol. 126, pp. 248÷257.

[77] Venner, C. H., Popovici, G., Wijnant, Y. H., 2004, "Contact dyanamics of EHL contacts with time varying operating conditions", *Proceedings of 30th Leeds−Lyon Symposium on Tribology*, D. Dowson et al., ed., Elseviers Tribology Series, pp. 189÷200.

[78] Wedeven, L.D., 1970, "Optical measurements in elastohydrodinamic rolling contact bearings", PhD Thesis, Imperial College, London, England

[79] Wedeven L.D., Evans D., Cameron A., 1971, "Optical analysis of ball bearing starvation", *Transaction of the ASME, Journal of Lubrication Technology*, pp. 349÷363

[80] Wensing, J.A., 1998, "On the dynamics of ball bearings", PhD Thesis, University of Twente, Enschede, The Netherlands, ISBN 9036512298.

[81] Westlake, F.J., 1970, "An inteferometric study of Ultra-thin fulid films", PhD Thesis, University of London, United Kingdom.

[82] Wijnant, Y. H., and Venner, C. H., 1997, "Analysis of an EHL circular contact incorporating rolling element vibration", *Proceedings of 23rd Leeds−Lyon Symposium on Tribology*, D. Dowson et al., ed., Elseviers Tribology Series, vol. 32, pp. 445÷456.

[83] Wijnant,Y.H., 1998, "Contact dynamics in the field of elastohydrodynamic lubrication", PhD Thesis, University of Twente, Enschede, The Netherlands. ISBN 9036512239.

[84] Wijnant, Y. H., Venner, C. H., and Larsson, R., and Eriksson,P., 1999, "Effects of structural vibrations on the film thickness in an EHL circular contact", *ASME Journal of Tribology*, vol. 121, pp. 259÷264.

[85] Yasutomi S., Bair S., Winer W.O., 1984, "An application of free volume model to lubricant rheology", *Transaction of the ASME, Journal of Tribology*, vol. 106, pp. 291÷303.

[86] Zhao, J., Sadeghi, F., and Hoeprich, M. H., 2001, "Analysis of EHL circular contact start up. Part I: Mixed contact model with pressure and film thickness results", ASME Journal of Tribology ,vol. 123, pp. 67÷74.

[87] Zhao, J., Sadeghi, F., and Hoeprich, M. H., 2001, "Analysis of EHL circular contact start up. Part II: Thermal model with surface results", *ASME Journal of Tribology*, vol. 123, pp. 75÷82.

[88] Zhao, J., and Sadeghi, F., 2003, "Analysis of EHL circular contact shut down", *ASME Journal of Tribology*, vol. 125, pp. 76÷90.

[89] SKF, General Catalogue 4000, 1999, Third Edition.

[90] http://www.skf.com/

[91] http://wikipedia.org

MOES FORMULAE

A.1   Moes approximation for $I\!K$, $I\!E$ and κ

The complete elliptic integrals of the first and second kind, appearing in the expressions in Chapter 2, are defined as:

$$I\!K(m) = \int_0^{\frac{\pi}{2}} \frac{d\psi}{\sqrt{1 - m^2 sin^2(\psi)}} \tag{A.1}$$

$$I\!E(m) = \int_0^{\frac{\pi}{2}} \sqrt{1 - m^2 sin^2(\psi)} d\psi \tag{A.2}$$

with the eccentricity factor: $m = 1 - \kappa^2 \quad \forall \quad 0 \leq \kappa < 1$

Approximate expression for the *first* and *second* kind complete elliptic integrals ($I\!K$, $I\!E$) and κ are given by Moes [55], see Figure A.1.

$$I\!K(m) \approx \frac{\pi}{2}(1 - m) \left[1 + \frac{2m}{\pi(1 - m)} \ln\left(\frac{4}{\sqrt{1 - m}} \right) - 0.375 \ln(1 - m) \right] \tag{A.3}$$

$$I\!E(m) \approx \frac{\pi}{2}(1 - m) \left[1 + \frac{2m}{\pi(1 - m)} - 0.125 \ln(1 - m) \right] \tag{A.4}$$

$$\frac{1}{\kappa(I\!D)} = 1 + \sqrt{\frac{\ln(16/I\!D)}{2I\!D} - \sqrt{\ln(4)} + 0.16 \ln(I\!D)} \quad for \quad 0 < I\!D \leq 1 \tag{A.5}$$
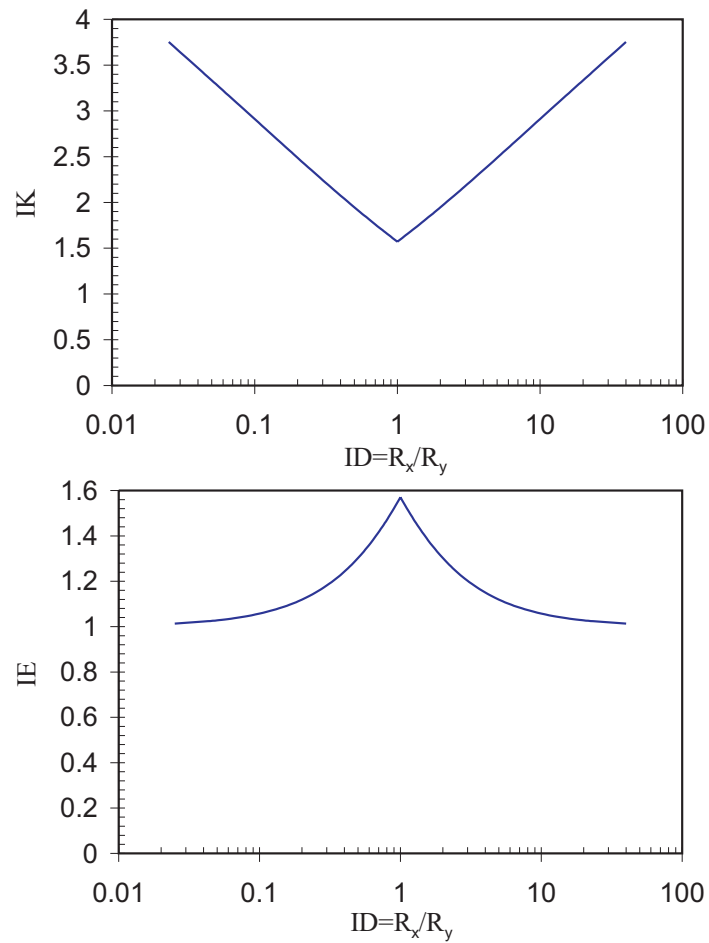
FIGURE A.1: *Evolution of the first and second kind elliptic integrals $\mathbb{K}$, $\mathbb{E}$ as function of R_x/R_y*

A.2 Nijenbanning film thickness formula

$$H_{cM} = \frac{h}{R_x} \left(\frac{\eta_0 2u_m}{E'Rx} \right)^{-1/2} \quad film\ thickness\ parameter \tag{A.6}$$

$$H_{cM} = \left\{ \left[H_{RI}^{3/2} \left(H_{EI}^{-4} + 0.1 D^4 \right)^{-3/8} \right]^{2s/3} + \left(H_{RP}^{-8} + H_{EP}^{-8} \right)^{-s/8} \right\}^{1/s} \tag{A.7}$$

$$s = \frac{3}{2} \left[1 + exp \left(-1.2 \frac{H_{EI}}{H_{RI}} \right) \right] \tag{A.8}$$

$$\begin{aligned} H_{RI} &= N^{-2} C_{RI}(D) \\ H_{RP} &= L^{2/3} C_{RP}(D) \\ H_{EI} &= N^{-2/15} C_{EI}(D) \\ H_{EP} &= N^{-1/12} L^{3/4} C_{EP}(D) \end{aligned} \tag{A.9}$$

$$\begin{aligned} C_{RI}(D) &\approx 145(1 + 0.796 D^{14/15})^{-15/7} \\ C_{RP}(D) &\approx 1.29(1 + 0.691 D)^{-2/3} \\ C_{EI}(D) &\approx 3.18(1 + 0.006 \ln D + 0.63 D^{4/7})^{-14/25} \\ C_{EP}(D) &\approx 1.48(1 + 0.006 \ln D + 0.63 D^{4/7})^{-7/20} \end{aligned} \tag{A.10}$$
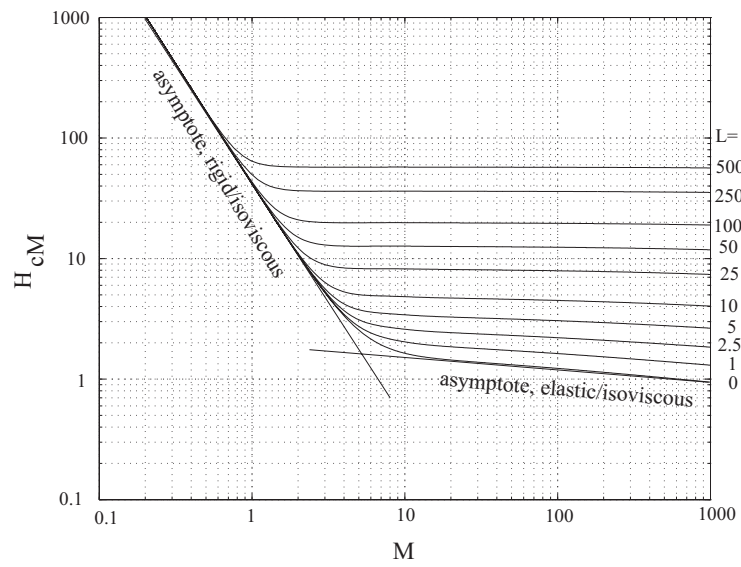
FIGURE A.2: *Survey diagram: Dimensionless film thickness for different operating conditions*

Numerical relaxation schemes

The residual of the Reynolds equation is given by:

$$\overline{r}_{i,j} = \langle f_{i,j} \rangle_P - K_{i,j} \langle \overline{P} \rangle \tag{B.1}$$

Depending on which relaxation scheme is used, the system matrix $A_{i,l}$ is filled according to one of the schemes: Gauss-Seidel line x (or y) or Jacobi distributive line x.

Gauss-Seidel line relaxation

$$A_{i,l}^{j} = \left. \frac{\partial K_{i,j} \langle P \rangle}{\partial P_{l,j}} \right|_{\underline{P} = \widetilde{\underline{P}}} \tag{B.2}$$

x direction

for $|i - l| > 1$

$$A_{i,l}^{j} = -\frac{1.5\widetilde{\overline{\rho}}_{i,j} K_{|i-l|,0} - 2\widetilde{\overline{\rho}}_{i-1,j} K_{|i-l-1|,0} + 0.5\widetilde{\overline{\rho}}_{i-2,j} K_{|i-l-2|,0}}{h_X} \tag{B.3}$$

for $i = l$

$$A_{i,i}^{j} = -\frac{\xi_E + \xi_W}{h_X^2} - \frac{\xi_N + \xi_S}{h_Y^2} - \frac{1.5\widetilde{\overline{\rho}}_{i,j} K_{0,0} - 2\widetilde{\overline{\rho}}_{i-1,j} K_{1,0} + 0.5\widetilde{\overline{\rho}}_{i-2,j}^{h} K_{2,0}}{h_X} \tag{B.4}$$

for $i > 1$

$$A_{i,i-1}^{j} = -\frac{\xi_E}{h_X^2} - \frac{1.5\widetilde{\overline{\rho}}_{i,j} K_{1,0} - 2\widetilde{\overline{\rho}}_{i-1,j} K_{0,0} + 0.5\widetilde{\overline{\rho}}_{i-2,j}^{h} K_{1,0}}{h_X} \tag{B.5}$$

for $i < n_X - 1$

$$A_{i,i+1}^j = -\frac{\xi_W}{h_X^2} - \frac{1.5\overline{\widetilde{\rho}}_{i,j}K_{1,0} - 2\overline{\widetilde{\rho}}_{i-1,j}K_{2,0} + 0.5\overline{\widetilde{\rho}}_{i-2,j}^h K_{3,0}}{h_X} \quad \text{(B.6)}$$

y-direction

for $|i - l| > 1$

$$A_{i,l}^j = -\frac{1.5\overline{\widetilde{\rho}}_{i,j}K_{|i-l|,0} - 2\overline{\widetilde{\rho}}_{i-1,j}K_{|i-l|,1} + 0.5\overline{\widetilde{\rho}}_{i-2,j}K_{|i-l|,2}}{h_X} \quad \text{(B.7)}$$

for $i = l$

$$A_{i,i}^j = -\frac{\xi_E + \xi_W}{h_X^2} - \frac{\xi_N + \xi_S}{h_Y^2} - \frac{1.5\overline{\widetilde{\rho}}_{i,j}^h K_{0,0}^{hh} - 2\overline{\widetilde{\rho}}_{i-1,j}^h K_{0,1}^{hh} + 0.5\overline{\widetilde{\rho}}_{i-2,j}^h K_{0,2}^{hh}}{h} \quad \text{(B.8)}$$

for $i > 1$

$$A_{i,i-1}^j = -\frac{\xi_S}{h_Y^2} - \frac{1.5\overline{\widetilde{\rho}}_{i,j}K_{1,0} - 2\overline{\widetilde{\rho}}_{i-1,j}K_{1,1} + 0.5\overline{\widetilde{\rho}}_{i-2,j}K_{1,2}}{h_X} \quad \text{(B.9)}$$

for $i < n_X - 1$

$$A_{i,i+1}^j = -\frac{\xi_N}{h_Y^2} - \frac{1.5\overline{\widetilde{\rho}}_{i,j}K_{1,0} - 2\overline{\widetilde{\rho}}_{i-1,j}K_{1,1} + 0.5\overline{\widetilde{\rho}}_{i-2,j}K_{1,2}}{h_X} \quad \text{(B.10)}$$

Jacobi distributive line relaxation

$$A_{i,l}^j = \left\{ \frac{\partial K_{i,j}\langle P\rangle}{\partial P_{l,j}} - \frac{1}{4}\left[\frac{\partial K_{i,j}\langle P\rangle}{\partial P_{l+1,j}} + \frac{\partial K_{i,j}\langle P\rangle}{\partial P_{l-1,j}} + \frac{\partial K_{i,j}\langle P\rangle}{\partial P_{l,j+1}} + \frac{\partial K_{i,j}\langle P\rangle}{\partial P_{l,j-1}} \right] \right\}\Big|_{\underline{P}^h = \underline{\widetilde{P}}} \quad \text{(B.11)}$$

$$A_{i,l}^j = -\frac{1.5\overline{\widetilde{\rho}}_{i,j}\Delta K_{|i-l|,0} - 2\overline{\widetilde{\rho}}_{i-1,j}\Delta K_{|i-l-1|,0} + 0.5\overline{\widetilde{\rho}}_{i-2,j}\Delta K_{|i-l-2|,0}}{h_X} \quad \text{(B.12)}$$

for $i = l$

$$A_{i,i}^j = -\frac{5}{4}\left(\frac{\xi_E + \xi_W}{h_X^2} + \frac{\xi_N + \xi_S}{h_Y^2} \right) - \frac{1.5\overline{\widetilde{\rho}}_{i,j}\Delta K_{0,0} - 2\overline{\widetilde{\rho}}_{i-1,j}\Delta K_{1,0} + 0.5\overline{\widetilde{\rho}}_{i-2,j}^h \Delta K_{2,0}}{h_X} \quad \text{(B.13)}$$

for $i > 2$

$$A_{i,i-2}^j = -\frac{1}{4}\frac{\xi_E}{h_X^2} - \frac{1.5\widetilde{\overline{\rho}}_{i,j}\Delta K_{2,0} - 2\widetilde{\overline{\rho}}_{i-1,j}\Delta K_{1,0} + 0.5\widetilde{\overline{\rho}}_{i-2,j}\Delta K_{0,0}}{h_X} \quad \text{(B.14)}$$

for $i < n_X - 1$

$$A_{i,i+1}^j = -\frac{\xi_W}{h_X^2} - \frac{1.5\widetilde{\overline{\rho}}_{i,j}\Delta K_{1,0} - 2\widetilde{\overline{\rho}}_{i-1,j}\Delta K_{2,0} + 0.5\widetilde{\overline{\rho}}_{i-2,j}\Delta K_{3,0}}{h_X} \quad \text{(B.15)}$$

for $i < n_X - 2$

$$A_{i,i+2}^j = -\frac{1}{4}\frac{\xi_W}{h_X^2} - \frac{1.5\widetilde{\overline{\rho}}_{i,j}\Delta K_{2,0} - 2\widetilde{\overline{\rho}}_{i-1,j}\Delta K_{3,0} + 0.5\widetilde{\overline{\rho}}_{i-2,j}\Delta K_{4,0}}{h_X} \quad \text{(B.16)}$$

CHARACTERISTICS OF DIFFERENT OILS

Temperature	Density	Viscosity		pressure-viscosity
		Kinematic	Dynamic	index
$[^\circ C]$	$[g/cm^3]$	$[cSt]$	$[cP]$	$[GPa^{-1}]$
TT 9 (Shell Turbo T9)				
20	-	-	20.1	25.57
25	-	-	15.7	24.47
30	-	-	12.46	23.45
40	0.876	9.41	8.24	21.62
60	-	-	4.19	18.61
80	-	-	2.46	16.24
100	-	-	1.61	14.37
HVI 60				
40			22	19.8
HVI 160/s (source Shell Laboratory)				
25	0.874	189.31	216.6	28.7
38	0.866	88.79	102.5	25.1
40	-	-	90.13	-
99	0.828	9.19	11.1	16.7
HVI 650 (Evans, 1983, PhD Thesis)				
30	-	-	900	30.2
40	0.888	506.76	450	27.5
50	-	-	240	24.8
60	-	-	140	22.9
70	-	-	85	21
80	-	-	55	19.5
90	-	-	37	18.4
100	0.853	31.65	27	17.5

TABLE 3.1: *Proprieties of TT 9, HVI 60, HVI 160/s and HVI 650*

DEDUCED PRINCIPAL DIMENSIONS

$DGBB$ 6312			
Parameter	Symbol	Value	Dimension
Elastic modulus	$E_1 = E_2$	213	GPa
Poisson's ratio	$\nu_1 = \nu_2$	0.29	$-$
Applied load on the bearing	F_r	400	N
Maximum load on the ball	F_N	220	N
Inner raceway-ball contact			
Radius ratio factor	$I\!D_i$	0.018	$-$
Ellipticity ratio	κ_i	0.076	$-$
Semi-major axis	a_i	1.377	mm
Semi-minor axis	b_i	0.105	mm
Contact deformation	c_i	2.584	μm
Maximum Hertzian pressure	p_{Hi}	0.722	GPa
Outer raceway-ball contact			
Ratio factor	$I\!D_o$	0.092	$-$
Ellipticity ratio	κ_o	0.21	$-$
Semi-major axis	a_o	0.812	mm
Semi-minor axis	b_o	0.171	mm
Contact deformation	c_o	3.276	μm
Maximum Hertzian pressure	p_{Ho}	0.752	GPa
Rotational speeds			
Inner raceway speed	n_i	$100 \div 1500$	rpm
Outer raceway speed	n_0	0	rpm
Lubricant (SKF T9@40[°C])			
Viscosity at atmospheric pressure	η_0	8.24×10^{-3}	$Pa \cdot s$
Pressure-viscosity index	α	21.6×10^9	Pa^{-1}

TABLE 4.1: *Operating conditions tested for the geometry of $DGBB$ 6312*
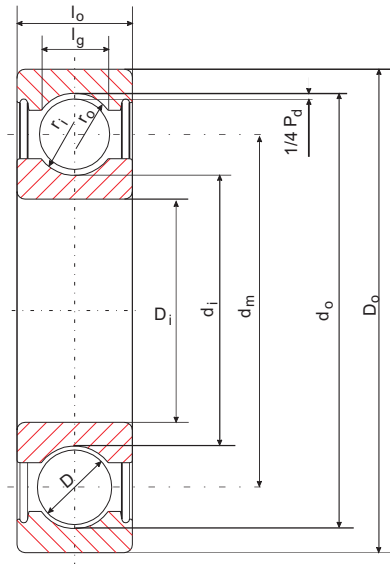
FIGURE D.1: *Principal dimensions for single row deep groove ball bearing*

$DGBB$ 6312			
Parameter	Symbol	Value	Dimension
Outer bore diameter	D_o	130	mm
Inner bore diameter	D_i	60	mm
Outer ring width	B	31	mm
Inner raceway diameter	d_i	72.784	mm
Outer raceway diameter	d_o	117.224	mm
Ball diameter	D	22.22	mm
Number of balls	Z	8	–
Inner groove radius	r_i	11.37	mm
Outer groove radius	r_o	12.00	mm
Pitch diameter	d_m	95.004	mm

TABLE 4.2: *Principal dimensions of $DGBB$ 6312*

$CRB\ NJ312ECP$			
Parameter	Symbol	Value	Dimension
Elastic modulus	$E_1 = E_2$	213	GPa
Poisson's ratio	$\nu_1 = \nu_2$	0.29	$-$
Applied load on the bearing	F_r	700	N
Maximum load on the ball	F_N	220	N
Inner raceway-ball contact			
Radius ratio factor	$\mathbb{D}_i$	$-$	$-$
Ellipticity ratio	κ_i	$-$	$-$
Semi-major axis	a_i	9.3	mm
Semi-minor axis	b_i	3.141×10^{-5}	mm
Contact deformation	c_i	0.419	μm
Maximum Hertzian pressure	p_{Hi}	0.223	GPa
Outer raceway-ball contact			
Ratio factor	$\mathbb{D}_o$	$-$	$-$
Ellipticity ratio	κ_o	$-$	$-$
Semi-major axis	a_o	9.3	mm
Semi-minor axis	b_o	3.839	mm
Contact deformation	c_o	0.431	μm
Maximum Hertzian pressure	p_{Ho}	0.183	GPa
Rotational speeds			
Inner raceway speed	n_i	$100 \div 1500$	rpm
Outer raceway speed	n_0	0	rpm
Lubricant (SKF T9@40[°C])			
Viscosity at atmospheric pressure	η_0	8.24×10^{-3}	$Pa \cdot s$
Pressure-viscosity index	α	21.6×10^9	Pa^{-1}

TABLE 4.3: *Operating conditions for the geometry of $CRB\ NJ312ECP$*
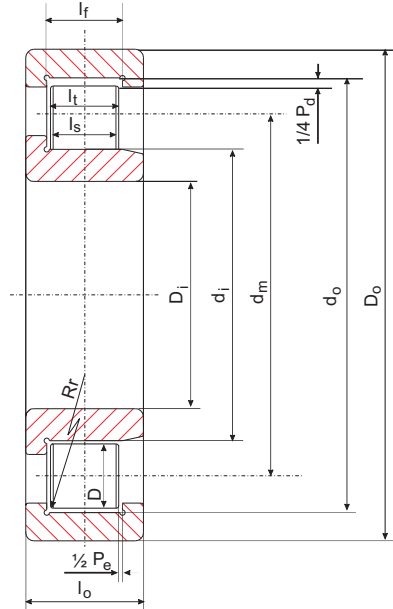
FIGURE D.2: *Principal dimensions for single row cylindrical roller bearings*

$CRB\ NJ312ECP$			
Parameter	Symbol	Value	Dimension
Outer bore diameter	D_o	130	mm
Inner bore diameter	D_i	65	mm
Outer ring width	B	31	mm
Inner raceway diameter	d_i	77	mm
Outer raceway diameter	d_o	115	mm
Roller diameter	D	19	mm
Roller total length	l_t	20	mm
Roller effective length	l_s	18.6	mm
Number of balls	Z	13	$-$
Inner groove radius	r_i	∞	mm
Outer groove radius	r_o	∞	mm
Pitch diameter	d_m	96	mm

TABLE 4.4: *Principal dimensions of $CRB\ NJ312ECP$*